Wireless Power Transfer
for Low Power Medical Sensors

Dimitris Tsorvas

Technische Universiteit Delft

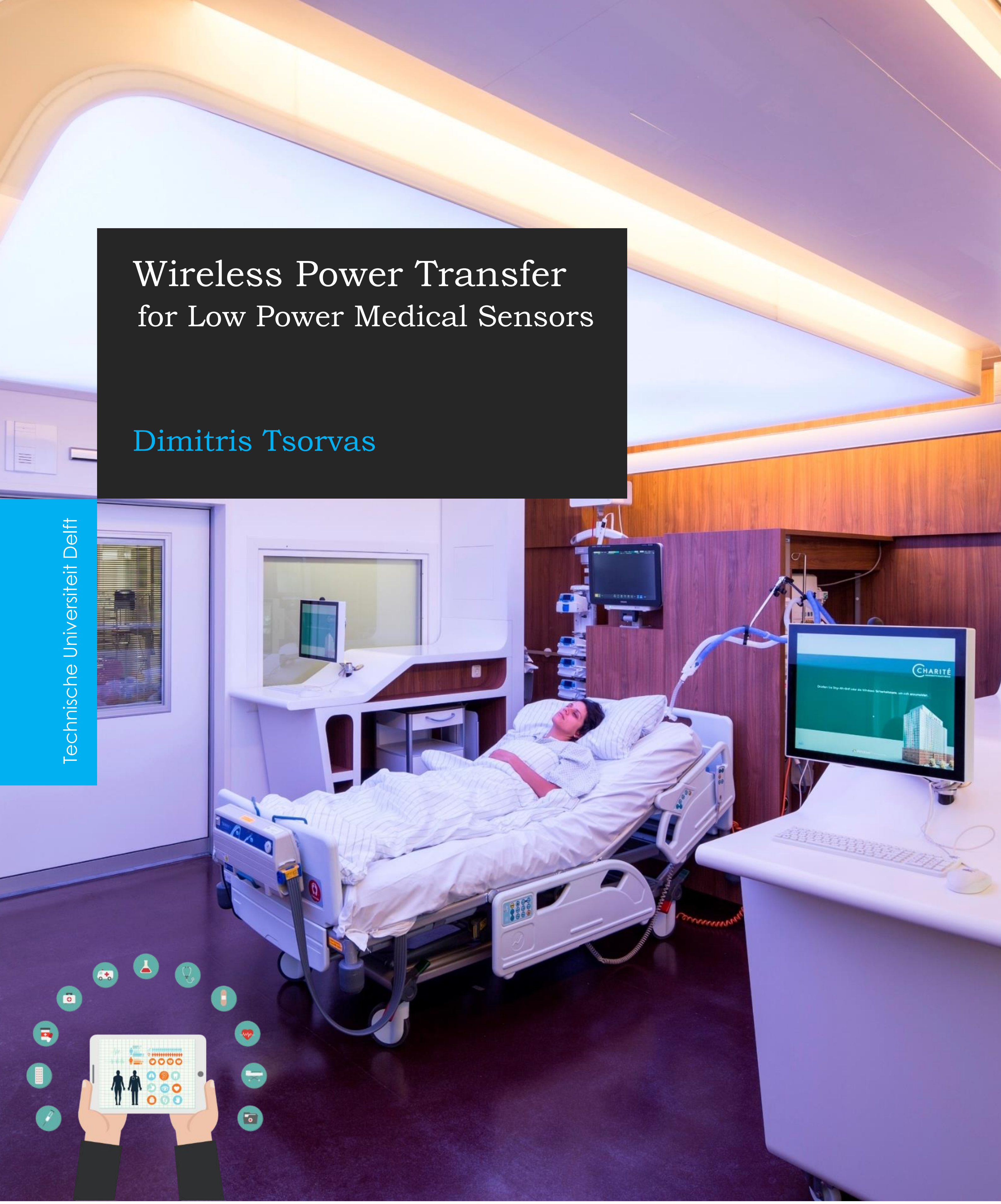

Delft University of Technology

Challenge the future

Wireless Power Transfer for low power medical sensors

Dimitrios Tsorvas

In partial fulfillment of the requirements for the degree of:

Master of Science
in Electrical Power Engineering

at

Delft University of Technology

August 24, 2017

Student Number:	4518543	
Committee Chair:	Prof. dr. ir. P. Bauer	TU Delft
Thesis Committee:	Dr.ir. J. Dong	TU Delft
	Dr.ir. J.R. Torres	TU Delft

Cover Page Image Ref.: Philips Luminous ceiling https://goo.gl/UCYprZ

DELFT UNIVERSITY OF TECHNOLOGY
DEPARTMENT OF DC SYSTEMS, ENERGY CONVERSION & STORAGE

Acknowledgements

First and foremost, I would like to thank my supervisors, Rolf van der Wal and Vijay Vasan Ashok, for their immense patience and support during the course of this thesis. They were always available for any kind of questions and discussions, constantly providing me with candid feedback. Without their experience and guidance this project would not have concluded successfully.

I would also like to thank my colleagues Gert Doodeman and Mark Kleijnen for the help they provided me regarding the system's RF properties. They have been extremely helpful throughout the whole duration of the thesis and were always ready to contribute with answers and information.

During the 8 months of conducting my thesis at Philips Innovation Services, I learned a great deal of technical and interpersonal skills while enjoying the process at the same time. I hope to have an opportunity to work with my PInS colleagues again in the future.

I would also like to express my gratitude to my daily supervisor Soumya Bandyopadhyay for his support. He assisted me during the length of the entire project providing valuable feedback and helping me shape the research scope of my thesis.

Without a doubt the past two years have been one of the most challenging, interesting and exciting periods of my life. There are several people, back in Greece and in the Netherlands, who have supported me through all this time. My family, whose unconditional love and support has been a source of inspiration and strength at difficult times, and my friends in the Netherlands. In particular "the feggaropetra" who made my stay in Delft one of the most memorable phases of my life!

Dimitris Tsorvas

Eindhoven, July 2017

Abstract

Internet of Things (IoT) encloses the utilization of sensors, actuators and data communication technologies embedded into physical devices enabling them to be tracked, coordinated or controlled over the Internet. Medical IoT refers to the vision where several wearables, sensors and actuators are scattered inside medical facilities and can interact with every other object, system or person over the cloud. This interactive network of things targeted for medical applications, is expected to generate market opportunities for patients and businesses by offering real time patient data and remote patient monitoring. The integration of this technology depends on autonomous operation of the modules and sustainable powering of these devices has proven to be one of its most challenging aspects.

Harvesting energy from renewable sources such as wind and solar, besides vibration and heat have been examined closely by research community over the past years. However, the limitations of these sources inside buildings, where solar and wind energy are not always sufficient, shifted the scientific and commercial focus to Wireless Power Transmission. This technology, despite its challenging nature, is becoming very popular because it overcomes the lack of different power sources inside buildings and provides user friendly powering method for battery-less sensor modules.

This thesis aims to investigate various antenna-rectifier topologies, also known as rectennas, and analyze the challenges that arise when harvesting low levels of radio frequency (RF) power. The initial part of this project focuses on the components that constitute a basic RF energy harvester. A system like this consists of an antenna which captures a fraction of the transmitted signal, attached to a rectifier which converts the RF signal into DC power. The development of analytical models and conducted lab measurements will identify the behavior of the rectifying circuit. In order to maximize the power transferred between the antenna and the rectifier, a matching infrastructure is necessary. Harvesting topologies with commercially available components and a matching network will be designed and manufactured along with custom antenna designs that match directly the input impedance of the rectifier. These novice antenna configurations decrease the size and cost of the system as well as improve the power conversion efficiency. Additionally, a power management integrated circuit will be introduced right after the rectifier to buffer the harvested DC power and provide protection for the sensor. Finally, this thesis culminates with a detailed presentation of the conducted total system experiments and future research possibilities.

Contents

1 Introduction

List of Figures

List of Tables

List of Abbreviations

IoT	Internet of Things
VNI	Cisco Virtual Networking Index
RF	Radio Frequency
WPT	Ireless Power Transfer
DC	Direct Current
AC	Alternating Current
EM	Electro-Magnetic
ISM	Industrial, Scientific and Medical radio bands
EIRP	Equivalent Isotropically Radiated Power
ECC	Electronic Communications Committee
ERP	Effective Radiated Power
IC	Integrated Circuit
PCB	Printed Circuit Board
RK4	Fourth order Runge-Kutta method
FFT	Fast Fourier Transformation
PCE	Power Conversion Efficiency
ADS	Advanced Design System
MPPT	Maximum Power Point Tracking
SMA	Sub-Miniature version A connector
VNA	Vector Network Analyzer
EMF	Electro-Magnetic Field
HPR	High Power Rectifying Topology
LPR	Low Power Rectifying Topology
SMD	Surface Mounted Device
DoD	Depth of Discharge
ESR	Equivalent Series resistance
FSPL	Free Space Path Loss

Chapter 1

Introduction

In this chapter the motivation for the development of a dedicated wireless power transfer system in a medical environment will be provided. After a conclusive view of the whole field of research, the research questions are formulated. Finally the chapter culminates in a brief outline of the thesis.

1.1 Trends and Conceptual frame

The vision of a world where every device can interact with every other object, person or system within a network is referred to as the Internet of things (IoT). Commercial implementations of this concept have only been emerging over the past few years even though it was initially conceptualized in the early 90's [1] and this is due to significant improvements on associated technologies such as sensor networks, cloud infrastructure, lower production costs and wireless communication systems.

One of its promising branches, medical IoT, has the potential to change the conventional healthcare treatment through enabling access to real time patient data and remote patient monitoring. The global Internet of Things healthcare market is expected to grow from the evaluated worth of $ 60 billion in 2014 to $136 billion by the end of 2021 [2]. Cisco in its recent VNI Mobile report estimates that smart devices and connections will surpass 8 billion devices worldwide confirming the trend of an ever-growing market of wireless sensors (Figure 1.1).

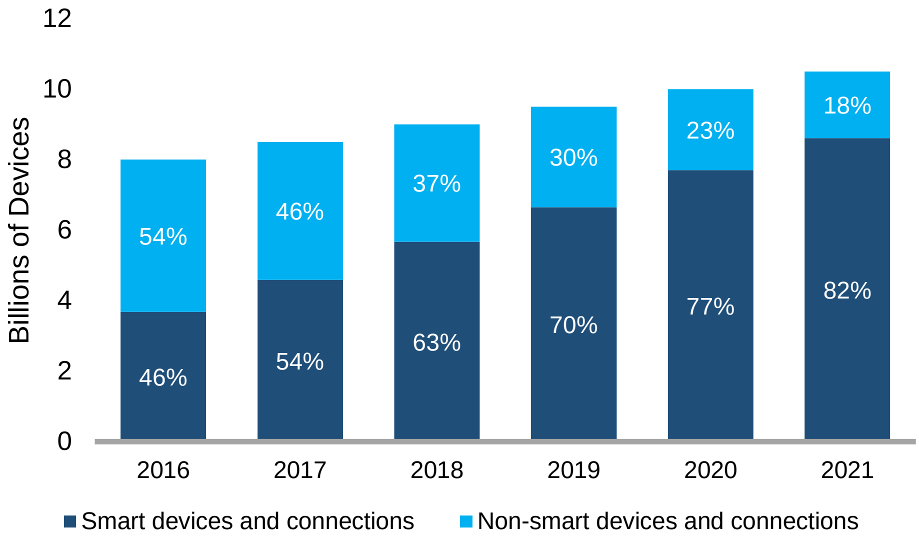

Figure 1.1: Wireless smart devices trends by Cisco VNI mobile 2017.

In the scenario proposed by this thesis, multiple networked sensors and actuators can be easily deployed at a healthcare facility with minimum cabling installation work as shown in Figure 1.2. Wearable sensors monitor the vital signs of the patient. The data transmitted from these sensors could be observed by medical staff in case of deviation from the expected values or transmitted to the cloud. Another functionality could be that these wearables interact with devices in the environment such as humidity, temperature or brightness sensors to provide the most suitable atmosphere for the patient.

Despite the need for wireless sensors in offices, houses and hospitals, their integration has been significantly slowed down due to cabling installation costs [4]. Especially for offices and places that are reconfigured frequently. The use of batteries might reduce these costs, however this poses as a non-ideal commercial option since the depleted batteries should be located, replaced and eventually disposed. Therefore these batteries must be recharged remotely and preferably by sustainable energy sources.

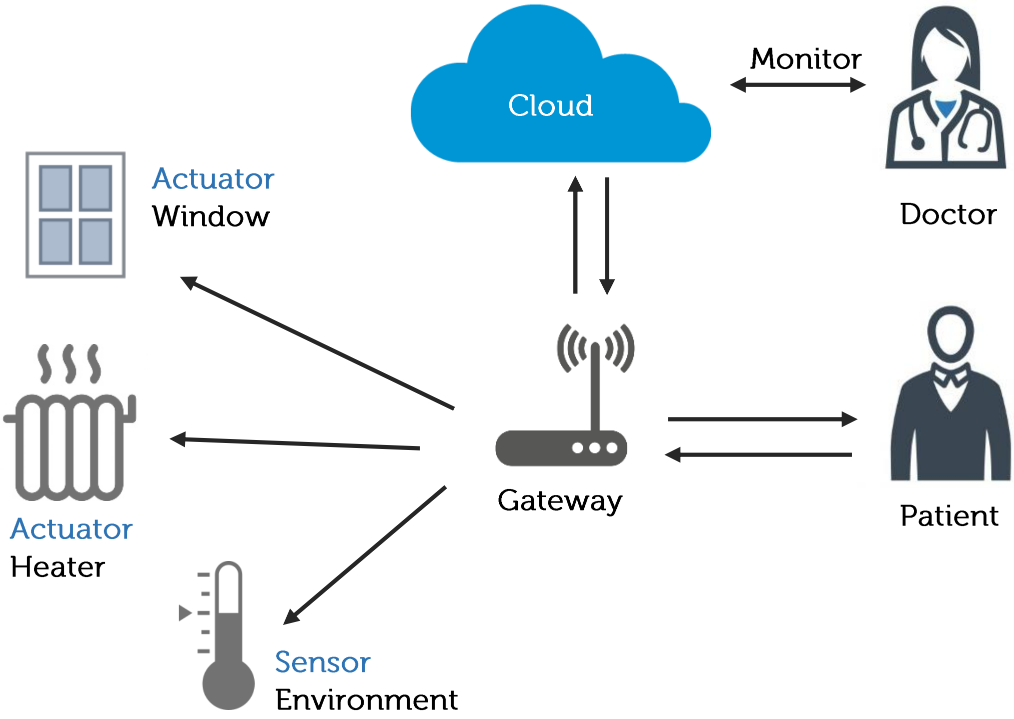

Figure 1.2: Thesis conceptual framework.

In order for a system as described above, to be deployable with ease in a medical facility such as a "Smart hospital" [3] the majority of these sensors and actuators should meet specific needs that can be summarized by the following:

- Secure communications
- Autonomous calibration
- Small form factor
- Plug and play ability
- Self-powered
- Sufficient battery life
- Sufficient transmission range

This thesis will be mainly examining the latter three points, related to the wireless power transfer and power management schemes required for the autonomous operation of such a sensor.

1.2 Radio Frequency Wireless power transfer

Recently, there has been an uprise of research/academic interests in radio frequency (RF) wireless power transfer [5], which is the ability of converting the received RF signals into electricity. This technology becomes a promising solution to power energy-constrained wireless networks, which have a limited lifetime hindering the overall system performance.

In RF power transfer, radio signals ranging from 3 kHz to as high as 3 GHz are utilized as a medium to carry energy in form of electromagnetic radiation. The techniques that are used can be classified as:

- RF energy transfer/harvesting
- Inductive coupling
- Magnetic resonance coupling

Inductive WPT is based on magnetic coupling that transfers electrical energy between a receiving and transmitting coil, resonating at the same frequency. The electric power is carried through the magnetic field between the two coils [6]. On the other side, magnetic resonance coupling is based on evanescent-wave coupling to transport electrical energy between two resonating coils [7]. The resonator coil is formed by adding capacitance to an induction coil. Both of the two techniques described above are classified as near-field wireless transmission featured with conversion efficiency and high power density. The coupling coefficient is the main factor influencing the transmission efficiency, and it mainly depends on the distance between two coils/resonators. However both of these techniques are not suitable for powering wireless sensors presented in the previous chapter because of the power being attenuated relative to the cube of reciprocal distance (60dB/ decade distance)[8]. On the other hand, RF energy transfer is the most suitable for powering a large number of distributed devices because it doesn't require calibration and alignment of the transmitting and receiving resonators. The signal strength of the far-field RF transmission attenuates relative to the reciprocal of the transmitter and receiver distance (20dB/ decade distance).

WPT Technique	Propagation	Field Region	Distance	Efficiency
Magnetic Resonance Coupling	Non-radiative	Near-field	centimeters up to meters	High
Resonant Inductive Coupling	Non-radiative	Near-field	millimeters up to centimeters	Medium-High
RF energy transfer	Radiative	Far-field	meters up to kilometers	Low

Table 1.1: Comparison of WPT techniques.

Table 1.1 presents the comparison between the aforementioned WPT techniques. It is obvious that RF energy transfer has advantages in terms of effective energy transfer distance but it presents low RF-DC energy conversion efficiency especially when the power levels are low.

1.2.1 Radiative vs Non-radiative RF Power Transfer

Charged particles such as electrons create electric and magnetic fields. Whenever any charge is in stationary position, an electrostatic field surrounds it. The magnetic field is created around a steady current of charges (DC, direct current). These aforementioned fields contain energy but they can't transfer power because of their stationary state. On the other hand, time-varying fields have the ability to carry power [9]. The alternating current (AC) of electrons inside a wire contains accelerated electric charges which generate time-varying electric and magnetic fields in the space around them. These fields apply oscillating forces on the electrons of the receiving antenna, resulting in them perturbing back and forth and thus representing an alternating current that could power a load. The oscillating electric and magnetic fields surrounding moving electric charges in an antenna can be divided into two regions, depending on distance from the antenna.

1.2.1.1 Non-Radiative Power Transfer

Power transfer utilizing induction requires only a time-varying magnetic field. Such a field can be directly generated by driving a coil with an AC current. Implemented this way, the magnetic field is able to oscillate up to million times per second (megahertz frequencies). If the size of the coil is much less than the wavelength, then the field around the coil remains magnetic in nature.

When current flows through the source coil, energy is stored in the magnetic field around it (inductor). This field, sometimes called an evanescent field, is confined to the source coil and falls off rapidly with distance. A second coil that intercepts a part of this field is "coupled" to the source and can wirelessly receive power. Power transfer can still be highly efficient because energy not transferred to the receive coil returns to the source coil. This energy is stored in the electric field of the capacitor of the RLC circuit. As energy is reciprocally transferred between the magnetic and electric fields, the stored energy can accumulate significantly in a phenomenon referred to as resonance. In the circuit shown in Figure 1.3 an AC source is connected to a coil L_t that is resonating with a capacitor C_t. At the receiver side, the coil L_r is respectively resonating with the capacitor C_r and positioned in the vicinity of the source. The resistances R_t and R_r describe the losses in the transmitting and receiving circuits.

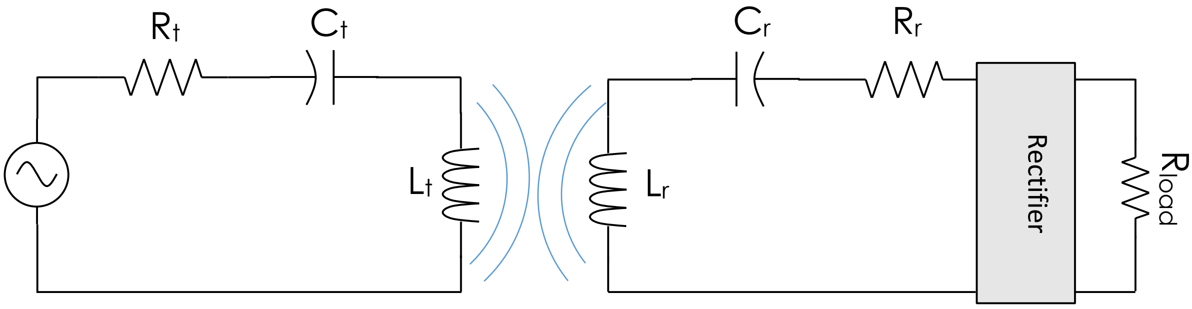

Figure 1.3: Non-radiative power transfer system.

1.2.1.2 Radiative Power Transfer

When the operating frequency increases to the point where the coil size is comparable to the wavelength of the signal, the power transfer scheme substantially changes. As the current flowing through the coil oscillates faster, the magnetic field changes more rapidly and generates a greater electric field. The electric field being time-varying, according to Maxwell's equations, generates time-varying magnetic field. This interaction between the magnetic and electric fields can result in self-sustained oscillations that move away from the source at the speed of light.

Sources that generate these kind of propagating fields are known as antennas and are used every-day from cell phones and radio. Utilizing this technology the range of power transfer can be much greater because the fields are not held near the source. However, there are some important technical disadvantages for radiative power transfer. For radiative sources, the direction of radiation is important because energy is transported away whether or not there are interacting objects in that direction. Therefore specific strategies should be implemented for narrowing the beam of radiation to increase the power transfer efficiency. In such a system the transmitting antenna radiates electromagnetic (EM) waves towards a receiver antenna that has the ability to rectify the RF signal and then transfer it to a load as depicted in Figure 1.4.

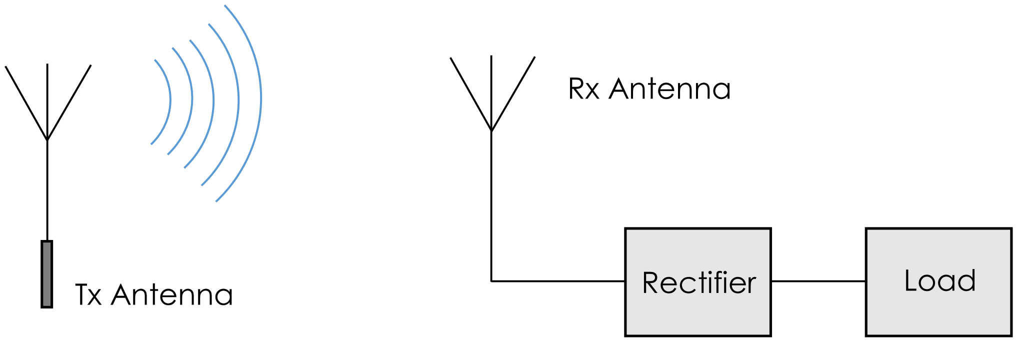

Figure 1.4: Simplified Radiative power transfer system.

1.2.2 RF Energy Harvesting

Energy can be efficiently harvested from solar irradiation [10], mechanical motion or thermo-electric sources [11].However, such conventional sources are essentially opportunistic and intermittent. The power availability highly fluctuates and is neither predictable nor controllable [12]. Unlike these sources, in a dedicated RF harvesting network the harvested energy is predictable and relatively stable over time due to fixed distance. The RF sources can be classified into three categories:

- *Dynamic ambient RF sources*: These sources are comprised by RF transmitters that operate periodically or use time-varying transmit power (e.g. WiFi access point). In order to have the most efficient power harvesting in such a scenario the RF harvester has to be adaptive and possibly “smart” enough to scan for energy harvesting opportunities in a specific frequency range. In [13] a study is presented that achieved energy harvesting from a dynamic ambient RF source where a secondary user can harvest RF energy from nearby transmitting primary users.

- *Static Ambient RF sources*: These sources refer to ambient RF transmitters which radiate stable power over time such as radio and TV towers. They can provide predictable RF energy, yet there could be long and short term fluctuations stemming from service schedule and signal fading. A high gain antenna is usually required combined with a wideband spectrum rectifier because the power density of ambient RF sources is small at different frequency bands. The study in [14] is an example of a sensor powered by static ambient RF sources .One highlight of this report was that when the distribution of ambient RF sources presents stronger repulsion, higher RF energy harvesting rate can be achieved.

- *Dedicated RF sources*: Dedicated RF sources can be used when a more predictable energy supply is required. These sources are operating within the ISM frequency bands with power levels ranging from 1 to 4 Watts EIRP and already have been commercialized like the TX91501 Powercaster [15]. However, the power output of RF sources are limited by regulations due to safety and health concern of RF radiations [16]. In order to compensate for such measures several transmitters/repeaters should be deployed to meet user demands. In [17] several RF energy transmission scenarios for mobile power transmitter to replenish wireless networks are investigated.

1.3 Thesis Objectives and Research Framework

This thesis specifically focuses on the design of an RF wireless harvester with the use of novice antennas and power management schemes. The majority of the factors that influence the system's performance will be simulated, analyzed and presented according to the operating scenario which will be explored in the following section.

1.3.1 Operating Scenario

The analysis presented by this thesis for radiative wireless power transfer in a medical environment was based on a conceptual ecosystem that according to recent trends [18] is not that far from commercialization. The goal of this thesis is to power a medical IoT equivalent temperature module from a distance that simulate an average hospital recovery room, ranging from 2.5 to 5 meters.

A dedicated RF source that resembles a typical wireless router will be responsible for providing adequate radiated power within regulations. This dedicated source should be strategically positioned in each room depending the respective topology in order to yield maximum power transfer efficiency. In order to have a "line of sight " propagation, meaning the electromagnetic waves traveling from the transmitter to the receiver in a direct path, the source should ideally be positioned on the ceiling of the room as shown in Figure 1.5. For larger installations multiple distributed RF sources can be used to cover the entire area. The transmitting antenna poses several challenges in terms of directivity and RF characteristics, however such an analysis is beyond the scope of this research. The present analysis, instead, is focused on the receiver side optimization and not on the dedicated source which will be simplified for the experiments.

1.3.2 Challenging Aspects

The scenario described in the previous section requires RF power transfer in frequency bands that are license-free and doesn't interfere with communications. The industrial, scientific and medical (ISM) radio bands are bands reserved internationally for the use of radio frequency energy for industrial, scientific and medical purposes other than telecommunications.

These frequency bands can be used without a license but there are restrictions in the maximum allowed Effective Isotropic Radiated Power (EIRP) which is the product of transmitter power and the antenna gain in a given direction relative to an isotropic antenna of a radio transmitter. According to ECC [19] for the ISM frequency of 868 MHz the maximum allowed EIRP does not exceed 3.3 Watts (equivalent to 2W ERP). Therefore low power levels should be anticipated at the receiving antenna because of the low initial transmission power and the spherical spreading of the electromagnetic waves in space. This translates to precise impedance matching techniques in order to minimize reflection losses.

A study performed in [20] demonstrated the benefits in antennas directly matching the rectifying circuit's impedance, therefore in the context of this thesis similar techniques are going to be implemented in order to design and compare these antennas to its commercial counterparts. Finally some remaining aspects that are going to be investigated are: the identification of the input impedance of the rectifier at the optimum power levels and the introduction of a power management scheme for this application.

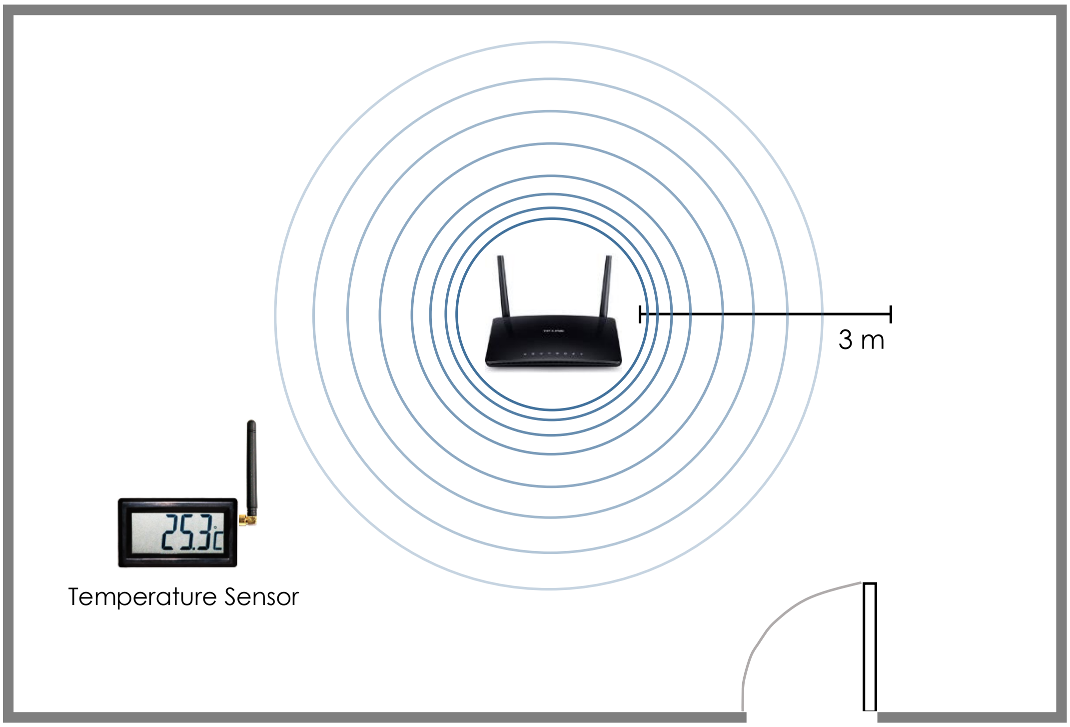

Figure 1.5: Proposed WPT scenario layout.

1.3.3 Research Questions

From the conceptual and research framework described in the previous sections, this study aims to answer the following research questions:

- Which is the most suitable rectifying topology for the proposed application?
- How does input power and frequency influence the Impedance of the rectifier?
- Can Conjugate Matching antennas power the proposed system and how do they perform when compared to traditional commercial counterparts?
- What improvements does the power management IC provide?
- What is the overall RF-DC conversion efficiency of such a system? Identify the losses.

1.4 Thesis layout

This section describes the approach or methodology taken in this thesis. In order to successfully answer the research questions mentioned above, this Master thesis is organized as graphically depicted in Figure 1.6.

Chapter 1: In this chapter the ever growing need for autonomous Sensors is discussed as well as possibilities of remotely powering them. After presenting the different RF power transfer technologies, radiative RF power transfer is chosen as the optimal way to transfer power wirelessly over a significant distance. The application for which this thesis was developed resides in the medical IoT Domain and smart hospitals. The importance of accurately designing the subsystems of such a receiver/sensor due to limited power densities was highlighted. Finally the research and conceptual framework of this study has been summarized.

Chapter 2: The components that comprise the RF rectifier is discussed. An analytical expression of the rectifying Schottky diode is presented in order to model its impedance and select the most suitable commercially available module. Furthermore the rectifying topologies were explored and justification for the use of voltage doubler has been offered. To support these claims several simulations were performed and compared to the experimental results.

Chapter 3: The theory and techniques behind the design of impedance matching networks for the proposed system will be presented. After selecting the adequate components and topologies, these matching networks will be combined with the voltage doubler circuits in the same PCB design in order to measure their performance in different power levels.

Chapter 4: Different antenna topologies will be investigated. Matching the Antenna impedance directly to the rectifiers input impedance has shown to improve compactness and efficiency while reducing manufacturing costs. Based on novice antenna designs and expanding on them, this chapter will introduce three antenna configurations. The proposed geometrical structure of these antennas makes it possible to tune their impedance to a value that matches approximately the input impedance of the rectifier. After performing simulations the characteristics of these antennas will be studied further through measurements on the manufactured PCB antennas.

Chapter 5: This chapter introduces the integration of a commercially available power management IC to the existing harvesting infrastructure to offer a more complete system in terms of options and robustness. This circuit is based on a TI evaluation board and contains a nano-powered boost and buck converter that enable the storage of energy to a battery/capacitor. Finally the total system testing, consisting of efficiency measurements at different stages of the configuration, will be analyzed in order to identify the performance bottlenecks of the power harvesting system.

Chapter 6: Finally, chapter 6 presents a summary of the whole system, answering the main research questions, providing conclusions and recommendations for future research.

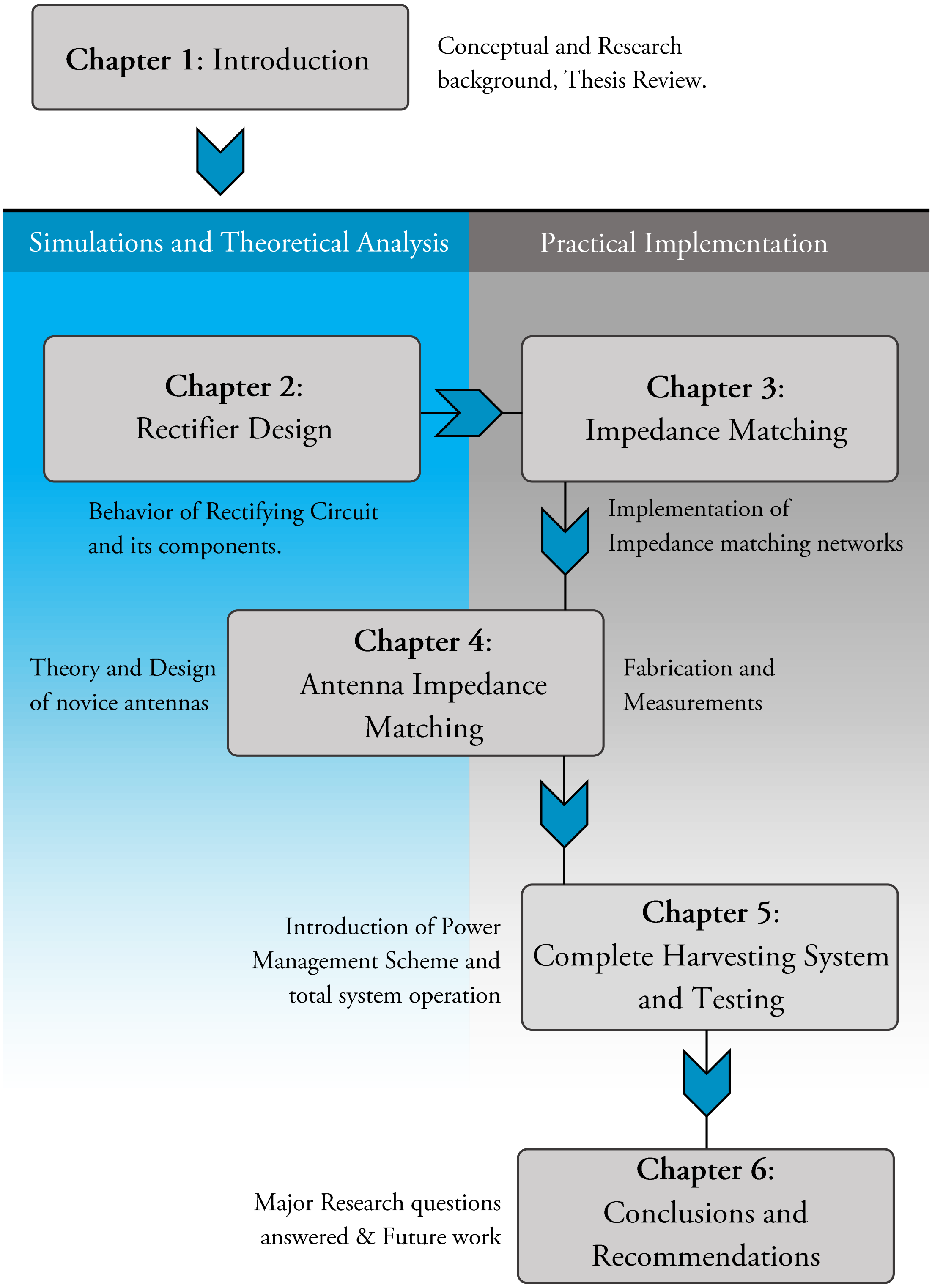

Figure 1.6: Outline of this thesis.

Chapter 2

Rectifier Design

In this chapter a study of the most suitable diodes and rectifying topologies will be presented in order to identify the most suitable configuration. Through simulations and analytical models the input impedance of the rectifier is calculated. The proposed method examines the impedance of the diodes for different input power levels.

2.1 Electrical characteristics and Physics of Schottky Barrier diodes

Standard silicon diodes have a turn on voltage of 0.6 volts and even germanium ones have a turn on voltage of around 0.3 volts, this is relatively high when small signals require rectification. In the proposed scenario of this thesis low power signals are to be expected. In order to overcome this issue, Schottky diodes will be used. These diodes are silicon based but have a turn on voltage of approximately 0.2 volts. This attribute makes them far more suitable than standard silicon diodes that could otherwise be used. Germanium diodes are available, but not nearly as widespread used. Subsequently any components based on this semiconductor are be more expensive and therefore not suitable for the low cost RF sensor application that this thesis will introduce.

Schottky barrier diodes present several differences when compared to their junction diodes counterparts. In Schottky diodes the current flow incorporates only one type of carrier instead of both. Specifically, in n-type Schottkys, forward current stems from electrons flowing from the n-type semiconductor to the metal; while in p-type, the forward current is composed of holes moving from the p-type semiconductor to the metal. This contact potential build-up between the metal and the semiconductor element forces the diode to conduct [21]. When an n-type semiconductor comes into contact with the metal, electrons diffuse out of the semiconductor in to the metal, resulting into a region known as the "depletion layer" where there are no free electrons available. The depletion layer is positively charged, and this makes the semiconductor positive with reference to the metal. The voltage difference between the metal and the semiconductor is referred to as the contact potential and is usually in the range 0.2~0.8 V for typical Schottky diodes. When positive voltage is applied to the metal, the internal voltage decreases, and electrons can flow. Electrons whose thermal energy is multiple times the average can escape, and are accountable for all the forward current from the semiconductor to the metal.

However there is no flow of minority carriers from the metal into the semiconductor. Therefore, when the positive voltage is removed, current stops almost instantaneously, and reverse voltage is generated in picoseconds. There is no delay due to charge storage as in the junction diode counterparts. This is the main advantage of the surface barrier in microwave applications, where the diode must switch states at microwave oscillator speeds.

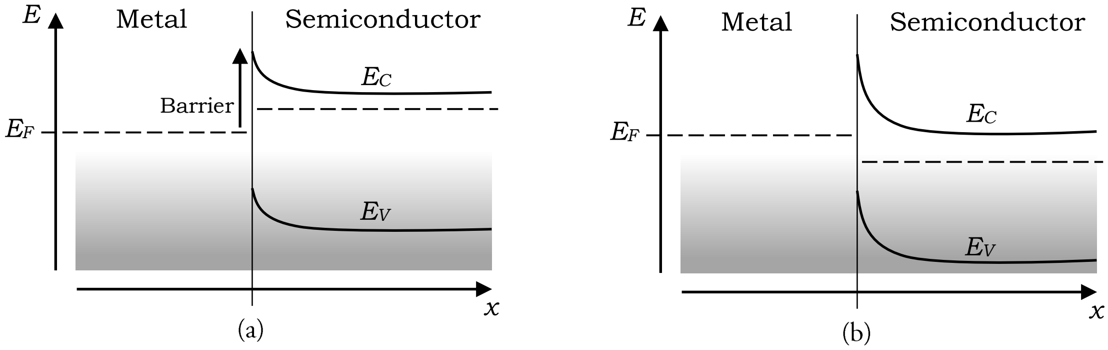

Figure 2.1: (a) Forward bias and (b) Reverse bias of the Schottky barrier to a n-type semiconductor [22], EC: conduction band edge, EF: Fermi level, EV: Valence band edge.

The depletion region in the semiconductor gives the barrier a high resistance when low voltages are applied. Under greater voltage bias the current flowing through the barrier behaves by the thermionic emission principle where a thermally induced flow of charge carriers moves over a potential energy barrier.

From figure 2.1 (a) when there is a forward bias many thermally excited electrons surpass the barrier and move from the n-type semiconductor to the metal. The current moves to the opposite site of the electron transfer. Subsequently the current rises rapidly with constant bias until the series resistance of the semiconductor starts to restraint the current. Under reverse bias as shown in figure 2.1 (b), the barrier is too high for thermally excited electrons to enter the conduction band from the metal however some of these electrons possess adequate amount of energy to surpass the barrier creating a small leakage current. This type of current is considered to be constant, even though it rises progressively due to a weak barrier lowering. Finally at very high voltage biases the depletion region breaks down.

2.2 Equivalent circuit of a Schottky diode

The Schottky diode can be represented by a nonlinear resistance R_j, in parallel with a capacitance C_j and in series with resistance R_s as shown in figure 2.2 (a). According to the analysis presented in [21] the resistance is the nonlinear barrier resistance at the rectifier contact. The capacitance represents both the barrier and overlay capacitance. At RF frequencies the shunting effect will decrease the voltage across the barrier while at lower frequencies the barrier capacitance does not influence the rectification procedure. C_j is the parasitic junction capacitance of the Schottky chip and because it is not possible to be tuned out by an external inductance at radio frequencies, by design it must be kept small to increase the rectification efficiency. The series package inductance and shunt package capacitance, comprising the diode's package parasitics, are represented by L_p and C_p. The effect of both of these factors should be considered when performing the diode analysis.

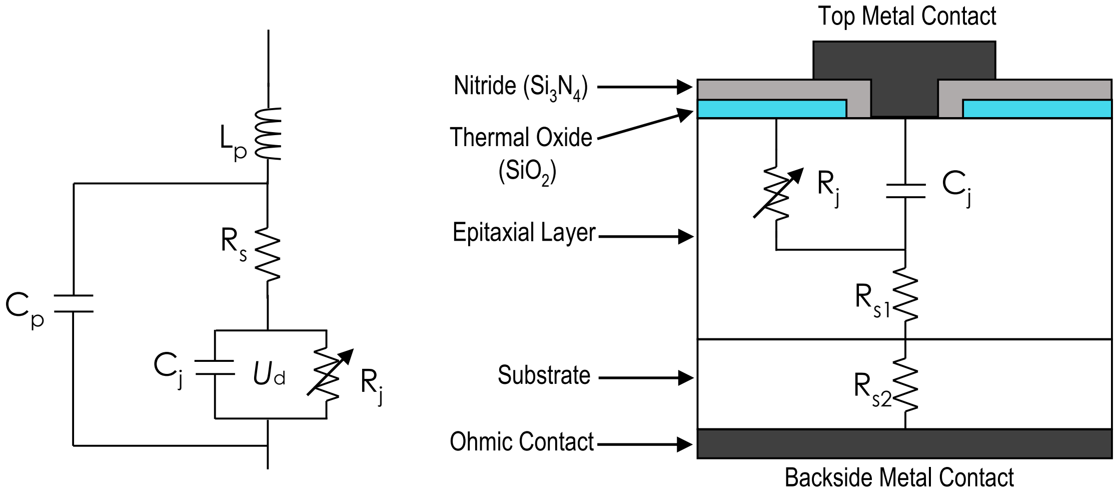

(a) (b)

Figure 2.2: (a) Equivalent circuit of a packaged Schottky diode (b) Schottky Diode Die.

According to [23] the value of Cj depends on the applied voltage U_d

$$C_j(U_d) = \frac{C_{j0}}{\sqrt{1-U_d/\varphi}}, \qquad (2.1)$$

where U_d is the voltage across the bare diode (Figure 2.2a), C_{j0} is the zero-bias barrier capacitance and φ is the barrier potential of the diode. These values usually can be determined from the diode's datasheet.

The voltage-current characteristic of the diode is given by

$$\mathrm{I_d} = \mathrm{I_s}(\mathrm{e}^{\left(\frac{\mathrm{q}}{\mathrm{nkT}}\right)\mathrm{U_d}} - 1)\,, \tag{2.2}$$

I_d represents the current flowing through the non-linear diode, I_s is the saturation current, q is the electron charge , *k* is the Boltzmann's constant (1.3806504×10^{-23} J/K), *T* is the temperature in kelvin and n is the ideality factor of the diode that can be found on the diode's datasheet.

However these equations apply to the bare diode and not the packaged diode. The packaging parasitics must be included in the equations in order for them to accurately predict the diodes nonlinear behavior. For the purposes of this thesis a linearization around a point of the voltage current characteristic will be sufficient to determine this behavior. Of course there are several other approaches like the harmonic balance analysis [24] where the circuit is examined separately in a linear and a nonlinear circuit. This method has proven to generate accurate results however a major drawback of this method is that for more than one higher harmonic, closed form analytical expressions are no longer valid.

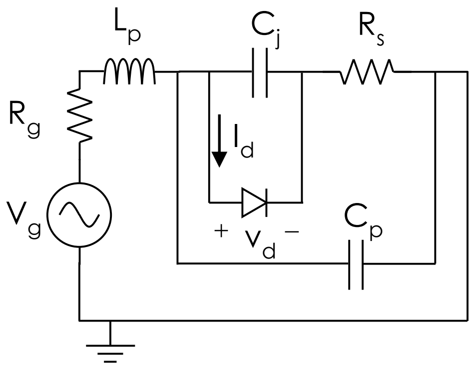

Figure 2.3: Circuit for determining the impedance of the packaged diode.

The numerical method that is going to be implemented is based on a time-advancing algorithm, which is time efficient. The system will be discretized into nonlinear first-order ordinary differential equations. An input signal and starting condition should be stated so that an integral over the differential equations is applied.

Using a small time step, the new system state is calculated according to the following equation,

$$y_{n+1} = y_n + \Delta t \cdot f(t_n, y_n), \tag{2.3}$$

Where y_n is the system state at t_n, y_{n+1} is the next system state at t_{n+1} and $f(t_n, y_n)$ is the derivative of y. Δt represents the time step $t_{n+1} - t_n$. To calculate the impedance of the diode the circuit depicted in Figure 2.3 will be used where R_g is the source resistance and V_g the source voltage described by:

$$V_g = |V_g| \cos \omega t \tag{2.4}$$

The following equations describe the voltages and currents in the circuit shown in Figure 2.3:

$$V_{C_p} = V_d + V_{R_s}, \tag{2.5}$$

$$V_g = I_g R_g + L_p \frac{dI_g}{dt} + V_{C_p}, \tag{2.6}$$

$$V_{R_s} = (I_{C_j} + I_d) R_s, \tag{2.7}$$

$$I_{C_j} = C_j \frac{dV_d}{dt}, \tag{2.8}$$

$$I_g = I_d + I_{C_j} + I_{C_p}, \tag{2.9}$$

$$I_{C_p} = C_p \frac{dV_{C_p}}{dt}, \tag{2.10}$$

From these equations the first order differential equations are generated:

$$V_g = L_p \frac{dI_g}{dt} + V_d + I_g R_g + R_s C_j \frac{dV_d}{dt} + R_s I_s (e^{\left(\frac{q}{nkT}\right) V_d} - 1), \tag{2.11}$$

$$I_g = I_s \left(e^{\left(\frac{q}{nkT}\right) V_d} - 1\right) + C_j \frac{dV_d}{dt} + C_p \frac{dV_g}{dt} - C_p R_g \frac{dI_g}{dt} - C_p L_p \frac{dI_y}{dt}, \tag{2.12}$$

and

$$I_y = \frac{dI_g}{dt}, \tag{2.13}$$

to avoid any second order derivatives.

In order to solve this ordinary differential equation system it must be analyzed as a set of coupled first-order differential equations. Every unknown derivatives will be expressed as known parameters:

$$\frac{\mathrm{dV_d}}{\mathrm{dt}} = \frac{1}{\mathrm{R_s C_j}}\left(\mathrm{V_g} - \mathrm{I_g R_g} - \mathrm{V_d} - \mathrm{I_y L_p} - \mathrm{R_s I_s}\left(\mathrm{e}^{\left(\frac{\mathrm{q}}{\mathrm{nkT}}\right)\mathrm{V_d}} - 1\right)\right), \tag{2.14}$$

$$\frac{\mathrm{dI_y}}{\mathrm{dt}} = \frac{1}{\mathrm{C_p L_p}}\left(\mathrm{I_s}\left(\mathrm{e}^{\left(\frac{\mathrm{q}}{\mathrm{nkT}}\right)\mathrm{V_d}} - 1\right) + \mathrm{C_j}\frac{\mathrm{dV_d}}{\mathrm{dt}} + \mathrm{C_p}\frac{\mathrm{dV_g}}{\mathrm{dt}} - \mathrm{C_p I_y R_g} - \mathrm{I_g}\right), \tag{2.15}$$

$$\frac{\mathrm{dI_g}}{\mathrm{dt}} = \mathrm{I_y}. \tag{2.16}$$

The parameters V_d, I_g, I_y and dV_g/dt are known at t_0. The initial conditions are $V_d = I_g = I_y = dV_g/dt = 0$. By inserting these equations in Matlab using a forth order Runge-Kutta (RK4) method for the specifications of an HSMS-2822 Schottky diode [25] with an operating frequency of 2 GHz and input power of 0 dBm it is possible to solve this system.

In figure 2.4 the Matlab solution of V_d together with the generator voltage is shown. The diode impedance can be now calculated by applying a fast Fourier transform (FFT) in Matlab to the calculated diode current and voltage:

$$\mathrm{Zdiode_{FFT}} = \frac{\mathrm{Vd_{FFT}}}{\mathrm{Id_{FFT}}}, \tag{2.17}$$

2.3 Analytical Model Simulation Results

The model described in the previous section constitutes a time-domain method to calculate the currents and voltages in a packaged diode circuit, which can ultimately using an FFT provide us with the diode circuit's input impedance including the series resistance and packaging parasitics.

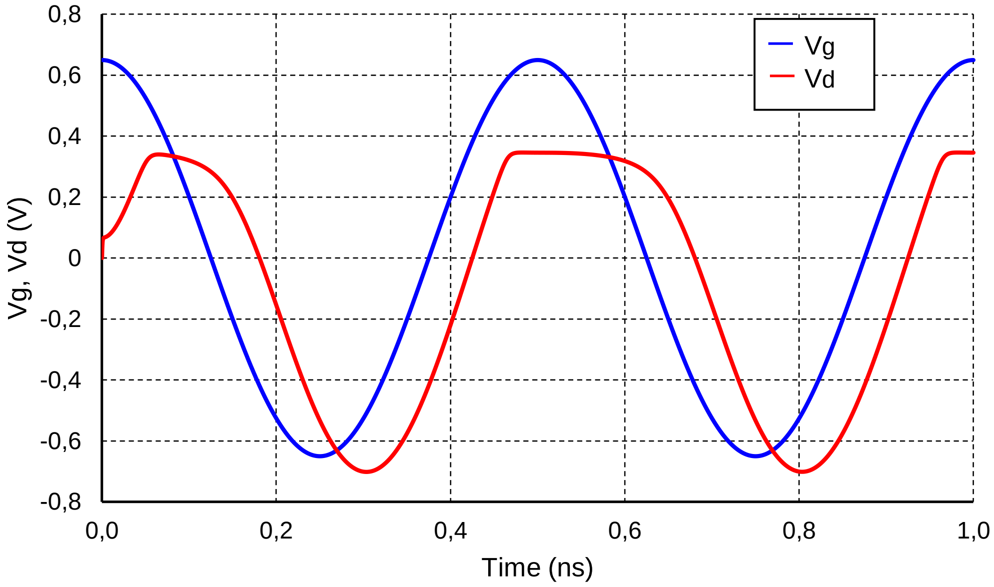

Figure 2.4: Simulation voltage output for the HSMS-2822 Schottky diode.

In the waveforms presented by figure 2.4 and generated by the RK4 method when source Vg is positive the diodes begins to conduct and holds the voltage across itself constant at 0.3V until the sinusoidal waveform falls below this value. During the negative half cycle, the diode is reverse biased (cathode more positive than anode) blocking current flow through itself and as a result has no effect on the negative half of the sinusoidal voltage which passes to the load unaltered. Then the diode limits the positive half of the input waveform and is known as a positive clipper circuit. The slight phase shift between the two voltages is caused by the packaging parasitics.

The following figures will provide a realistic approximation of the examined diode impedances over a range of frequencies.

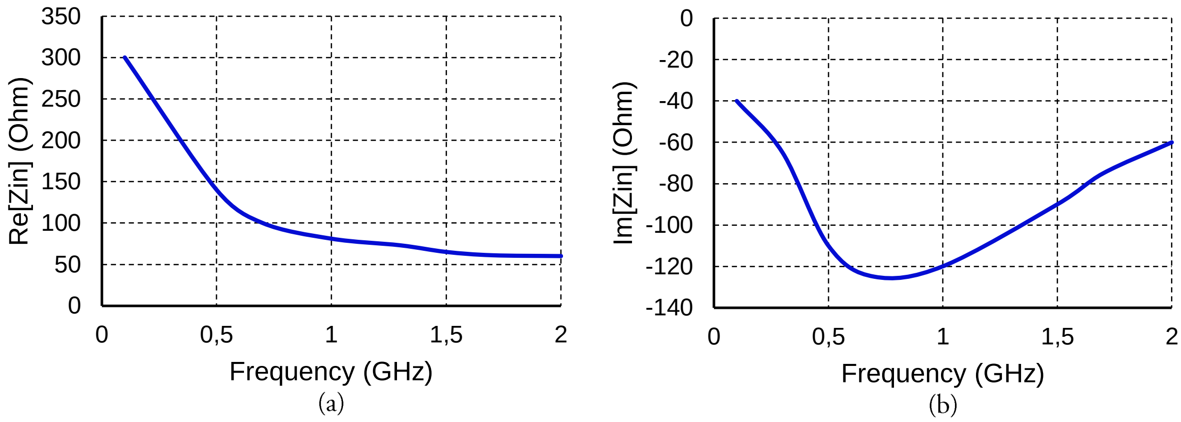

(a) (b)

Figure 2.5: Frequency sweep of the real (a) and imaginary part (b) of the HSMS-2820 Schottky diode's impedance for power levels of -5 dBm (316x10^{-6}W) and source impedance of 50 Ohms.

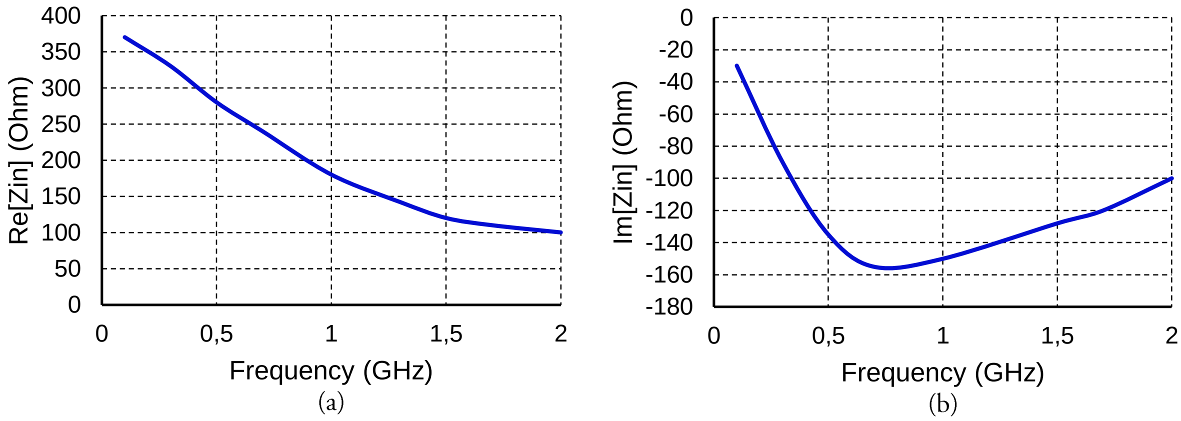

(a) (b)

Figure 2.6: Frequency sweep of the real (a) and imaginary part (b) of the HSMS-2850 Schottky diode's input impedance for power levels of -5 dBm and source impedance of 50 Ohms.

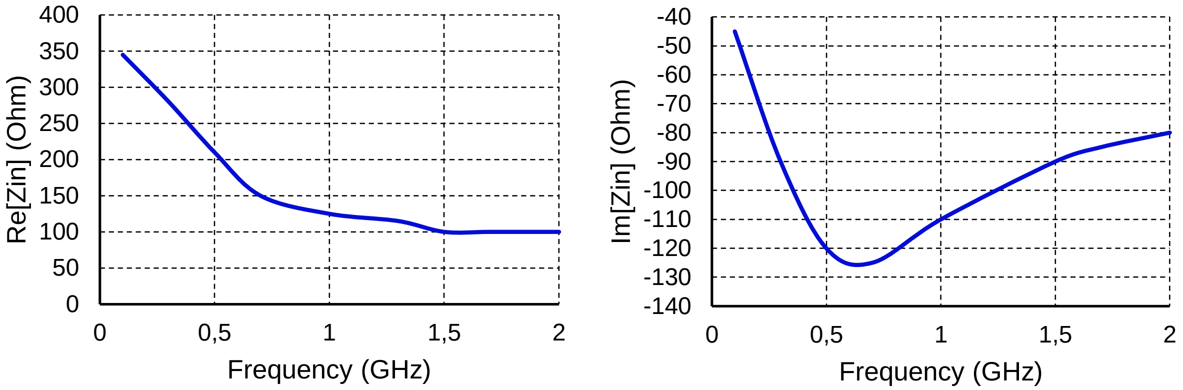

(a)

(b)

Figure 2.7: Frequency sweep of the real (a) and imaginary part (b) of the HSMS-2860 Schottky diode's impedance for power levels of -5 dBm ($316x10^{-6}$W) and source impedance of 50 Ohms.

Parameter	**HSMS-2860**	**HSMS-2850**	**HSMS-2820**	Units
B_V	7.0	3.8	15	V
C_{J0}	0.18	0.18	0.7	pF
E_G	0.69	0.69	0.69	eV
I_{BV}	1E-5	3E-4	1E-4	A
I_S	5E-8	3E-6	2.2E-8	A
N	1.08	1.06	1.08	-
R_S	6.0	25	6.0	Ω
P_B	0.65	0.35	0.65	V
P_T	2	2	2	-
M	0.5	0.5	0.5	-

Table 2.1: SPICE parameters used in the Matlab simulation to calculate the input impedance of the three different Schottky diodes [25][26][27].

After examining the diodes parameters and characteristics this thesis will focus mostly on the HSMS-282x and HSMS-285x Schottky diode families because of their performance in high frequencies and low voltage turn-on sensitivity which is extremely important in the proposed scenario. The first type of diode can be exposed to higher power levels (above -10 dBm) thus will be examined for a relatively higher power environment than the latter which will be implemented for lower power scenarios.

2.4 Diode Selection

This section examines the DC output voltage as a function of input power for a single diode. The method that is going to be used is the Ritz-Galerkin method [28] and it can estimate the output voltage for different load resistance values. The output voltage is implicitly given by:

$$B_0\left(\frac{q}{nkT}\sqrt{8R_gP_{in}}\right) = (1 + \frac{V_0}{R_LI_s})e^{(1+\frac{R_g+R_S}{R_L})\frac{q}{nkT}V_0} \qquad (2.18)$$

Where B_0 is the zero order modified Bessel function of the first kind, P_{in} is the input power, I_S is the saturation current, R_L is the load resistance and R_S is the series resistance of the diode. Furthermore q is the electron charge, T is the temperature in Kelvin, n is the diode's ideality factor and k is the Boltzmann's constant.

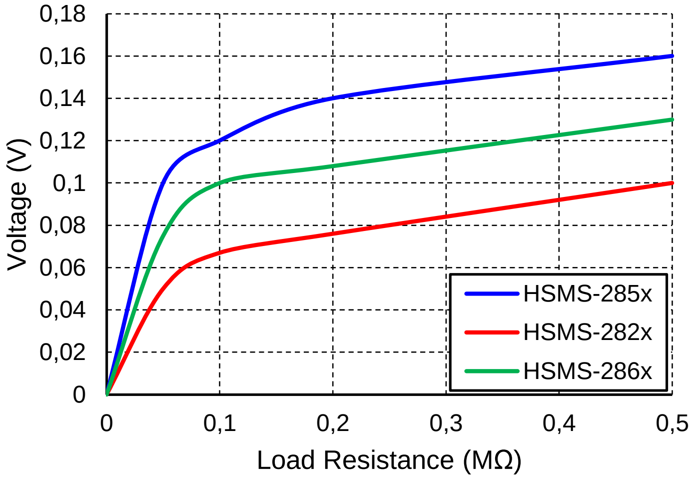

Figure 2.8: Output voltage versus load resistance for the three diodes in test. The results were obtained through Matlab for Input power of -15dBm.

Figure 2.8 shows the Matlab simulated DC output voltage of the diodes when no matching circuit is present at input power of -15dBm. The Schottky diodes with higher saturation current and contact resistance like the HSMS-2850 and the HSMS-2860 present higher V_{OUT} for the same input power and load resistance. However one of the objectives of this thesis is to present and compare two alternative rectifying configurations for low and high RF power levels. The HSMS-2850 out-performs the other two diodes and will be used for the low power option. The HSMS-2860 produces higher V_{OUT} than the HSMS-2820 but is not designed to handle high RF power like the HSMS-2820 which inevitably will be the second choice.

2.5 Rectifier Configuration

Since the input power captured by the antenna is limited by regulations, and mostly because of free space path loss between the source transmitter and the antenna system, losses in surrounding objects, size limitations of the antenna and impedance mismatch between the antenna and the rectifier. The rectifier must be able to produce relatively high output voltage for lower levels of incoming power [29]. In order to accomplish that, the choice of performance parameters is important. The diode characteristics such as saturation current and forward voltage drop can influence the rectifier's performance [30]. The rectifier configurations can determine the rectifier performance for certain power levels. Specifically when the number of diode capacitor pairs in the circuit increases, the DC output voltage rises, but the overall efficiency decreases [31]. Furthermore, the performance of a rectifier based on Schottky diodes is closely related to the value of load resistance. While the output voltage of the rectifier is greater at a higher load resistance, the efficiency is gets hindered. Optimal efficiency can be achieved at a specific load resistance. All those design considerations should be taken into account when selecting the most suitable rectifier configuration. In the following sections several rectifying configurations will be analyzed in order to identify the most efficient and cost effective layout.

2.5.1 Half-wave rectifier

The simplest design that can be used is a peak detector or half wave peak rectifier. This configurations contains a series connection of a diode and a capacitor generating a DC voltage equal to the peak value of the AC signal. The circuit is shown in Figure 2.9 below. An AC voltage source applied to the detector, charges the capacitor to the peak of the input. The diode conducts positive half-cycles, charging the capacitor to the waveform peak value. When the input waveform drops below the DC peak stored on the capacitor, the diode becomes reverse biased, blocking the current flow from the capacitor back to source. Therefore, the capacitor retains the peak value even when the waveform drops to zero.

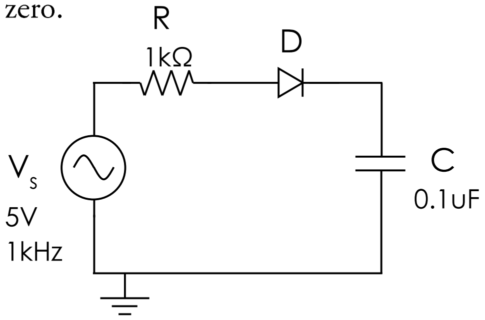

Figure 2.9: Basic peak detector circuit

It takes a few cycles for the capacitor to charge to the peak due to the time constant (RC). As it is shown figure 2.10 the capacitor does not charge all the way up to 5 V and that's because there is no such thing as an "ideal" diode. The silicon diode has a forward voltage drop of 0.7 V which is subtracted from the 5 V peak of the source.

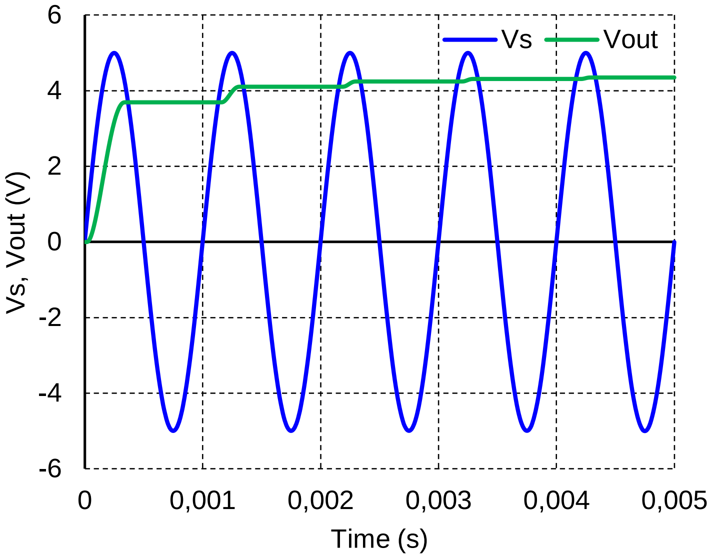

Figure 2.10: Behavior of the peak detector circuit as modeled in LTSPICE.

This circuit produces a significant ripple on the DC output of the signal when connected to a load. The voltage decreases in relation to the inverse of the resistance of the load multiplied by the capacitance. Finally the voltage output is always similar or lower than the input signal therefore it wouldn't be a suitable rectifier topology for the proposed scenario because the voltage should be multiple times higher to drive an IoT sensor.

2.5.2 Full-wave rectifier

A full-wave rectifier is a non-multiplying detector circuit that requires no RF chokes, does not have a back-off voltage, and does not depend on whether there is a DC path through the source network or not and is shown in Figure 2.11.

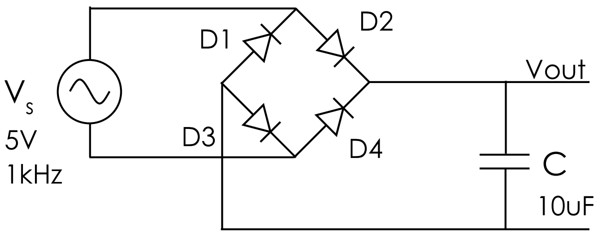

Figure 2.11: Full-wave rectifier circuit.

This circuit is very common in modern power supplies, but it has two major disadvantages in signal detection and RF rectification applications; the first one being that it has two diode forward-voltages in the path to the load, and the other being that either the output or the input terminals must be allowed to float with respect to the ground. However, one advantage of the full-bridge rectifier is that the maximum inverse voltage for any of the diodes is only $\sqrt{2}$ times the RMS input voltage. The magnitude of the inverse voltage across D2 is limited from rising above $V_{in}\sqrt{2}$ by the clamping action of D1 and so on. The same argument applies for diodes D3 and D4.

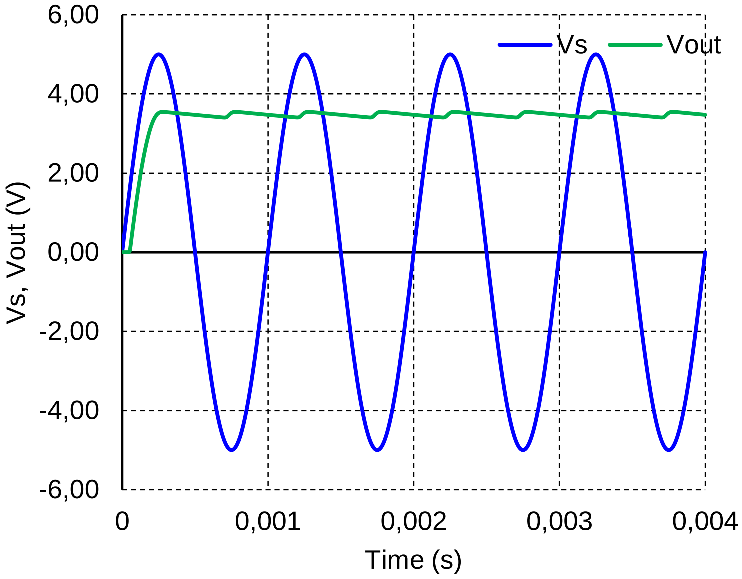

Figure 2.12: Behavior of the full-wave rectifier circuit when connected to a load as modeled in LTSPICE. The voltage drop in the output is due to the two forward voltages of the diodes.

During the positive half of the cycle, D2 is on, D1 is off and charge is stored on the capacitor. But, during the negative half, the diodes are reversed, D1 is on and D2 is off. The capacitor doesn't discharge nearly as much as in the previous circuit, so the output has less ripple, as shown in Figure 2.12. It produces a cleaner DC signal than the half-wave rectifier, but the circuit itself is more complicated with the use of extra components that increases the cost and the possibility of a component failure along with the significant voltage drop in the output introduced by the non-ideal diodes.

2.5.3 Greinacher voltage doubler

The circuit shown in Figure 2.13 represents a single stage voltage multiplier circuit. The circuit is also known as voltage doubler because in principle, the voltage on the output is approximately two times the input. This topology comprises of two parts; each includes a diode and a capacitor necessary for rectification. The high frequency input signal is rectified in the positive half of the input cycle, followed by the negative half. However, the voltage stored on the input capacitor during one half cycle is transferred to the output capacitor during the next half cycle of the input signal. In this way, the voltage at the output capacitor is almost two times the peak value of the RF source voltage lowered by the turn-on voltage of the diode.

One important aspect of this topology is that these stages can be combined by connecting them in series. This topology behaves similar to the principle of stacking DC voltage sources in series to generate more voltage at the output. The first stage's output is not quite pure DC and it is basically an AC signal with a DC offset. Due to this feature, combined stages result in larger voltage output than the previous stages. When a second stage is stacked on top of the initial multiplier circuit, the signal that the second stage is receiving is the noise of the first stage. This noise is then multiplied by two and added to the DC voltage of the first stage. Thus, the more stages that are added, presumptively, more voltage will be measured at the output.

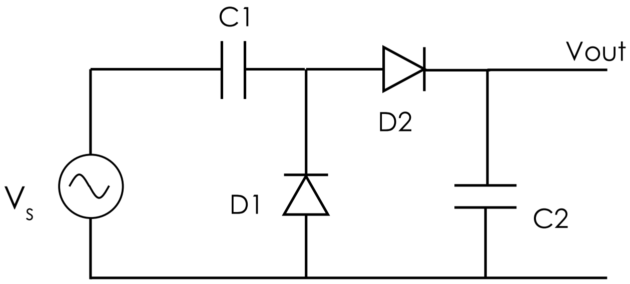

Figure 2.13: Single stage voltage multiplier circuit.

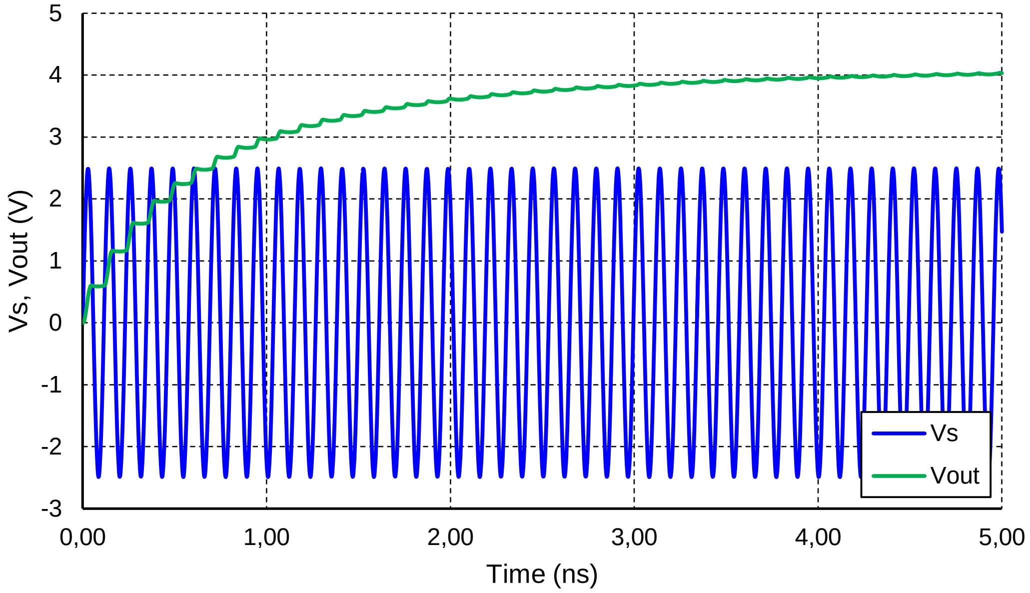

Figure 2.14: Behavior of the single stage voltage multiplier circuit from an RF source of 2.5V amplitude at 900MHz supplying a 10KΩ load as modeled in LTSPICE.

Rectifier Type	**Structure**	**Rectifier Topology**
Basic Rectifier	Single diode in series with a load. A capacitor is added to smoothen the ripple in the output.	Half-wave rectifier, full-wave rectifier [32]
Voltage Doubler	Utilizes two rectifying stages to double-up the DC voltage.	Villard circuit, Greinacher circuit, Dickson charge pump [33][34]
Voltage Multiplier	Converts RF to DC by utilizing a network of capacitors and diodes.	Villard cascade multiplier, Cockroft-Walton voltage multiplier [35]

Table 2.2: Comparison of suitable RF rectifying topologies.

The combination of low complexity, increased voltage output and stacking capability makes the voltage doubler/multiplier circuits more compelling than the remaining rectifying topologies for RF to DC energy conversion. In the next sections the characteristics of this topology will be examined to determine the relationship between the power conversion efficiency (PCE) and factors such as the rectifying stages, load value and input power.

2.6 Number of rectifying stages

When low input power levels are applied on the rectifier its DC output voltage will reside way below the 1.5 V mark that most commercial electronics operate. Therefore to boost this voltage, a voltage multiplier will be utilized similar to Figure 2.16. However there is a limit to how many of these stages should be implemented because as the rectifying stages increase, cost and complexity increase while efficiency eventually decreases. By simulating the rectifying circuits in ADS, the effect of the number of stages in the output voltage will be examined along with the ramifications in power conversion efficiency.

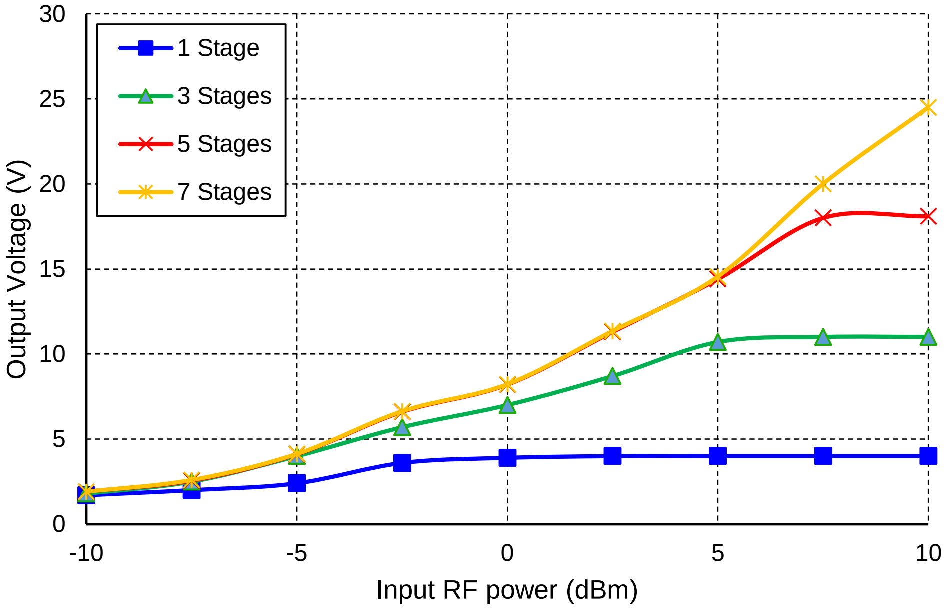

Figure 2.15: Output voltage correlation with voltage multiplier stages based on the HSMS-2820 diode.

At input power values ranging from -10 to -5 dBm, which can approximate the power levels that are going to be fed into the rectifier, all the examined rectifying topologies have similar performance in terms of voltage output. The distinction becomes clearer as the power levels increase, however for the application of low power sensors the interest is focused on the 0 to 5V voltage span where the single stage is quite competitive and more cost efficient. From figure 2.15 the non-linear behavior of the voltage multiplier circuit is apparent.

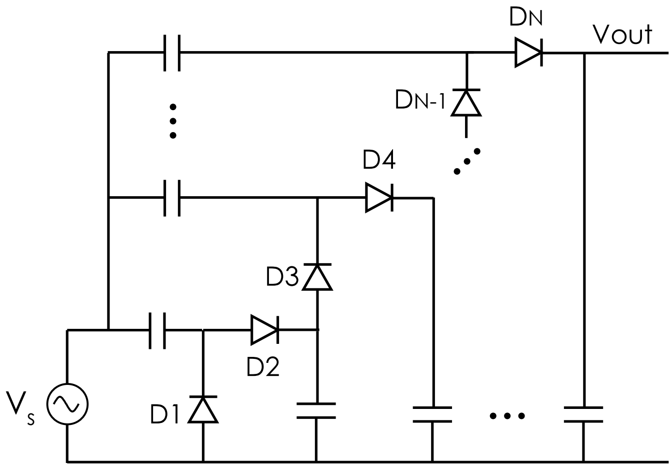

Figure 2.16: Dickson charge pump based voltage multiplier with N stages.

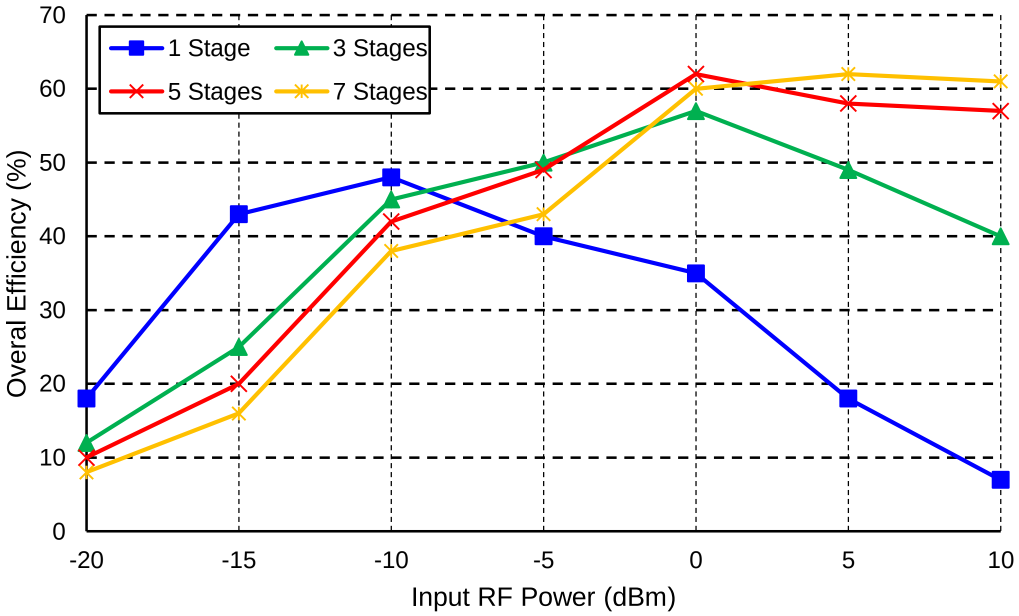

Figure 2.17: Effect of number of stages on the efficiency of the HSMS-2850 based rectifier.

From Figure 2.17 the relation between the total conversion efficiency and the amount of input RF power is examined through LTSPICE simulations. According to these findings the single stage voltage doubler is the most efficient at -10 dBm of Input RF power. As the input power increases the efficiency also increases with the number of stages but within the contexts of this thesis the efficiency in lower power levels is considered more important. This means that the single stage voltage doubler is the most suitable circuit for energy harvesting in terms of complexity, cost and efficiency.

The conversion efficiency is defined in [36] as,

$$\mathrm{n_{con}} = \frac{\text{Power Output}_{\text{ DC}}}{\text{Input RF Power} - \text{Reflected RF Power}} \tag{2.19}$$

while, the overall efficiency is described as:

$$\mathrm{n_{o}} = \frac{\text{Power Output}_{\text{ DC}}}{\text{Input RF Power}} \tag{2.20}$$

Conversion efficiency doesn’t include the reflected RF power caused by impedance mismatches. However the overall efficiency does include this amount of reflected power and thus provides a more realistic metric of the energy harvesting performance.

2.7 Effect of Load Impedance

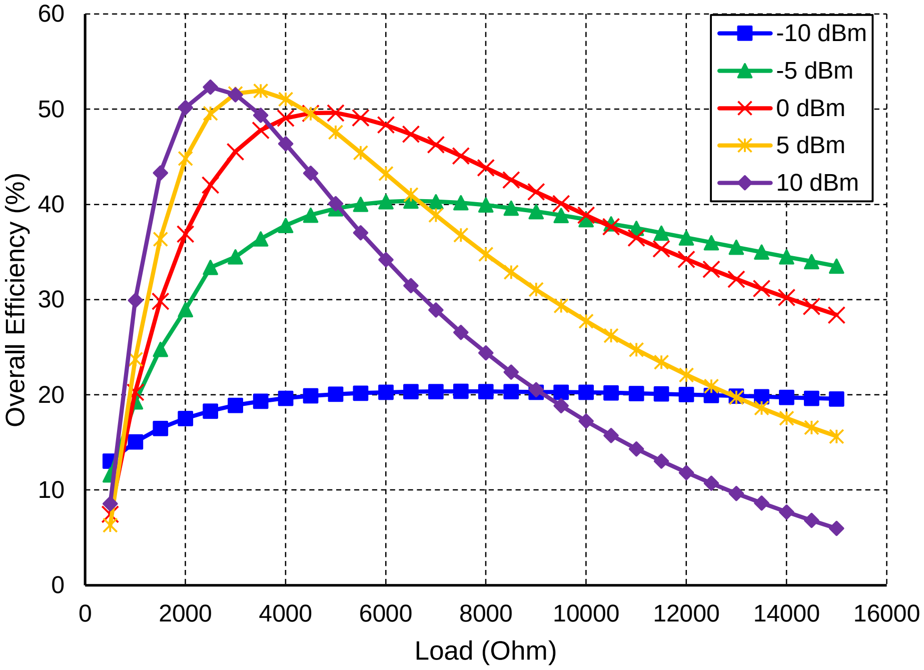

Figure 2.18: Effect of load impedance on the efficiency of the HSMS-2820 based rectifier.

It is imperative that the load impedance must be specifically chosen for a defined rectifying circuit. This is highlighted in Figure 2.18 where the ADS simulation results reveals the relationship between the overall efficiency and the load impedance utilizing parameter sweeps of −10 dBm to 10 dBm and 500 Ω to 15 KΩ for input RF power and load value, respectively. It can be observed that the circuit yields the optimal efficiency at a particular load range. Moreover the circuit's efficiency decreases significantly when the load value gets too low or too high. The energy harvesting circuit in simulation is comprised by a single stage circuit using the HSMS-2820 diodes.

In other words, for different input power the optimal operating point in terms of load impedance shifts. A solution to this challenge will be presented in the next chapters with the introduction of a power management IC that offers maximum power point tracking (MPPT).

2.8 Input Impedance Measurements

In the previous sections the impedance of the rectifier was calculated through analytical model simulations in Matlab. However the equivalent circuit impedance will also be verified by measurements. The Schottky diodes HSMS-2822 and HSMS-2852 will be used for the lab measurements. The RF behavior of the voltage doubler can be summarized in Figure 2.19 (b). The capacitors can be considered as short circuits and the input impedance is half the value of that of a single diode. For the DC behavior shown in Figure 2.19 (c) the capacitors are considered to be open-circuits and the two diodes will act as they were connected in series [37].

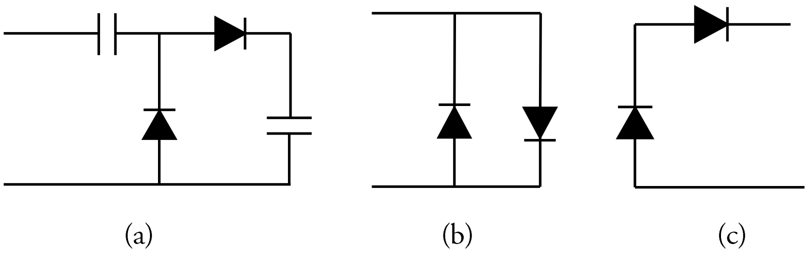
(a) (b) (c)

Figure 2.19: (a) Voltage doubling circuit. (b) RF equivalent circuit. (c) DC equivalent circuit.

Since the equivalent RC circuit can be represented as two antiparallel diodes the three-pin SOT-23 configuration will be preferred because it already contains two diodes sharing a common pin between the anode of the first and the cathode of the second [25]. These packaged diodes were mounted directly on a subminiature version-A connector (SMA). This connector was attached to Keysight's E5071C Vector Network Analyzer (VNA) with a 50 ohm transmission line coaxial cable. In order for the coaxial cable's length not to influence the measurements, the calibration has been taken place at the point after the SMA connector just before the diodes. The VNA can accurately measure the reflection coefficient S_{11} at the point of calibration.

2.8.1 Reflection Coefficient

Reflection coefficient is the ratio of the complex amplitude of the reflected wave to that of the incident wave. When a source with an impedance Z_S is connected to a load impedance Z_L Figure 2.20, the reflection coefficient Γ is described by:

$$\Gamma = \frac{Z_L - Z_R}{Z_L + Z_R} \tag{2.21}$$

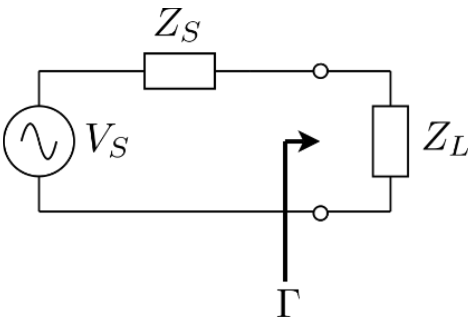

Figure 2.20: Measurement location of reflection coefficient [38].

This coefficient is a clear indication for the amount of reflected power only when the source impedance is not complex [38]. When the source's impedance is complex and conjugate to the load impedance Γ will be non-zero.

2.8.2 Measurement set-up and results

As mentioned in the previous section the two diodes connected in antiparallel fashion on a small PCB were connected through an SMA connector to a 50 ohm transmission line with the VNA to obtain the impedance measurements as shown in Figure 2.21.

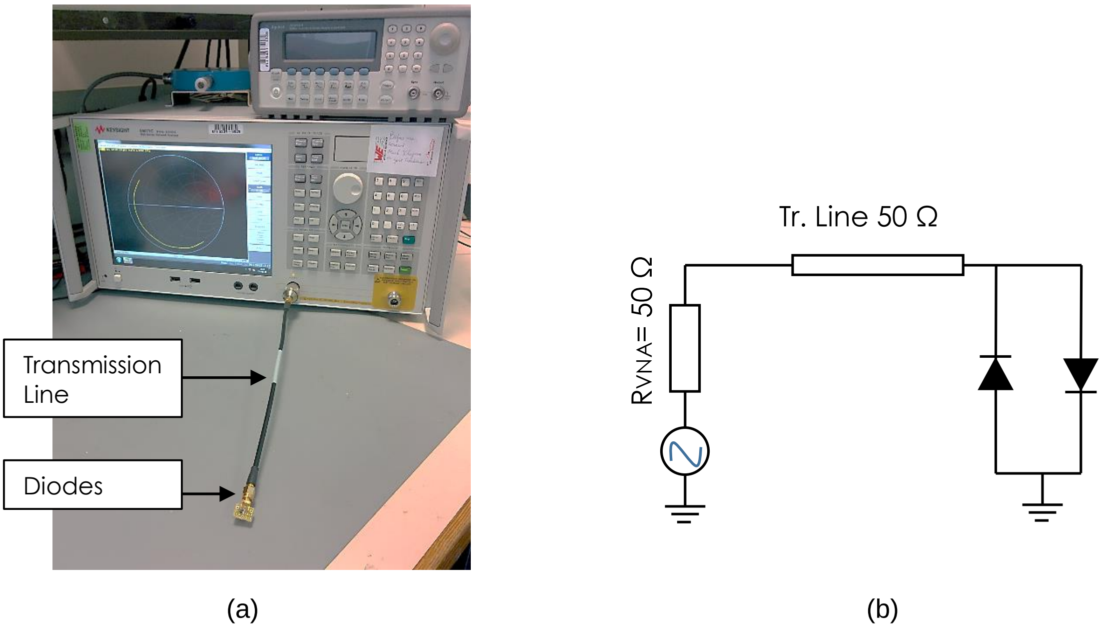

(a) (b)

Figure 2.21: (a) Lab set-up for impedance measurements. (b) Schematic representation of the set-up.

The VNA as mentioned before measures the reflection coefficient in S-parameters (S_{11}). After receiving these data a transformation should be performed to calculate the input impedance according to the following formula:

$$Z_{input} = Z_0 \frac{1 + S_{11}}{1 - S_{11}} \tag{2.22}$$

Where Z_0=50 Ω.

The results of the impedance measurements for the diode HSMS-2822 and HSMS 2852 are presented below:

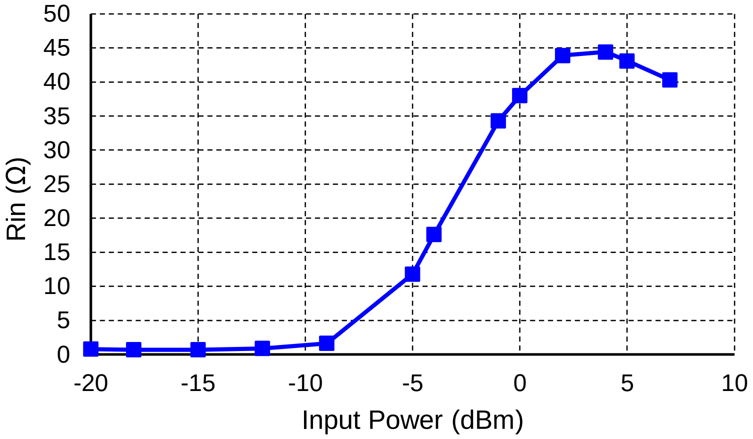

Figure 2.22: Real part of the input impedance of the HSMS-2822 rectifier versus input power.

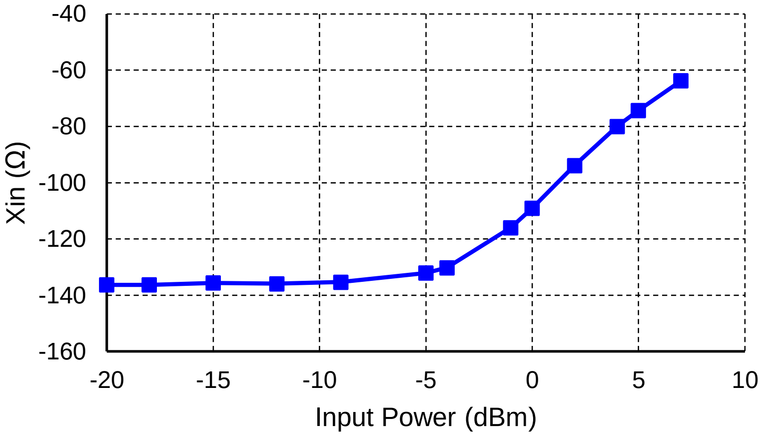

Figure 2.23: Imaginary part of the input impedance of the HSMS-2822 rectifier versus input power.

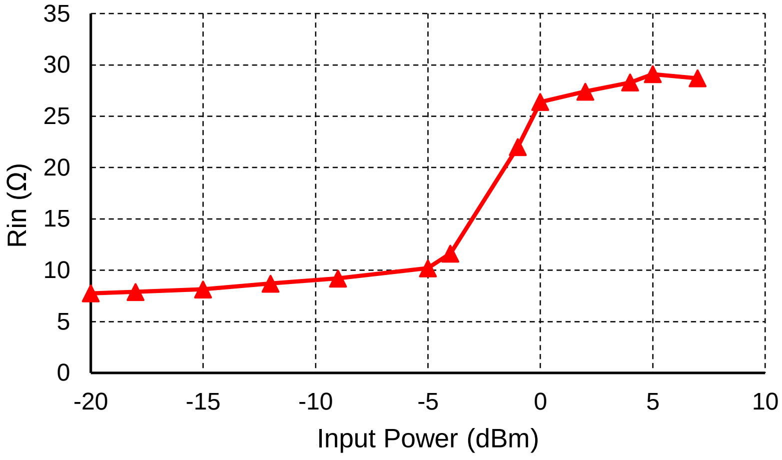

Figure 2.24: Real part of the input impedance of the HSMS-2852 rectifier versus input power.

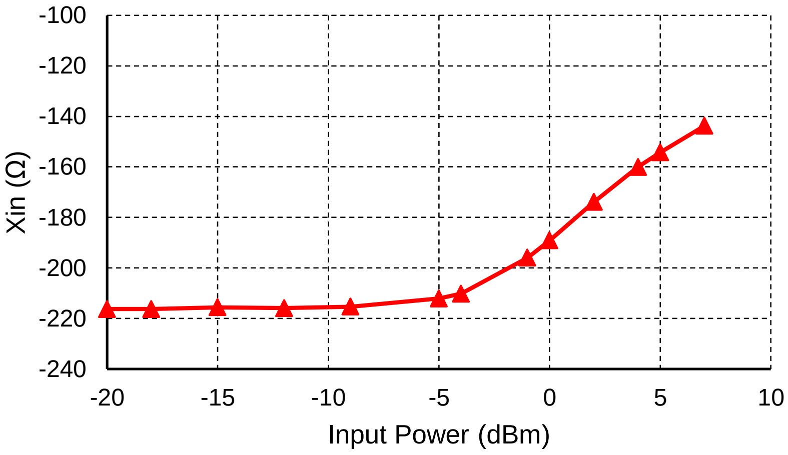

Figure 2.25: Imaginary part of the input impedance of the HSMS-2852 rectifier versus input power.

Figures 2.22 to 2.25 reveal the non-linear behavior of the diode's impedance at different input power levels. Therefore input power and operating frequency are two major factors that affect the rectifiers input impedance. Around the -5 dBm mark of input RF power it can be seen that the real part of the impedance increases while the imaginary part decreases in both versions of the rectifier. In order to have maximum power transfer from the antenna to the load this impedance must be matched. The techniques used for this matching will be presented in the next chapter.

2.9 Conclusions

This chapter presented a complete rectifier analysis for RF harvesting systems. Specifically a simulation method to estimate the input impedance of the diodes for different power levels and frequencies was introduced. The accurate prediction and measurement of the rectifiers input impedance plays a significant role in maximizing the power transfer between the antenna and the rectifier in a harvesting system. That statement made imperative the identification of the non-linear behavior of the diodes and the rectifier subsequently.

Multiple stages of the voltage doubler rectifying circuit show improvements in DC voltage output but not necessarily for the RF power range that the system is expected to operate (-10 to -5 dBm). The excess amount of output voltage above the 1~3V range that the sensor requires, does not provide any benefit. In fact the efficiency of the single stage voltage multiplier, after simulations, was higher @ -10 dBm for the HSMS-2852 rectifier when compared to the multiple stages. Finally the diodes where measured in the network analyzer to provide more accurate input impedance values of the rectifier.

Chapter 3

Impedance Matching

In this chapter the theory and techniques behind the design of impedance matching networks for the proposed system will be presented. After selecting the adequate components and topologies, these matching networks will be combined with the voltage doubler circuits in the same PCB design in order to measure their performance in different power levels.

3.1 Impedance matching fundamentals

When high-frequency signals are carried on transmission lines, specific measures must be taken so that the transmission topology is matched to its termination/load. The source and load impedances should be equal the characteristic impedance of the transmission line, as this minimizes signal reflections. Impedance discontinuities or mismatches will degrade the signal's amplitude and phase accuracy.

Mismatch loss is the amount of power that will not be available on the output due to impedance mismatches and signal reflections. A transmission line that is properly terminated, that is, terminated with the same impedance as that of the characteristic impedance of the transmission line, will have no reflections and therefore no mismatch loss [40]. Impedance matching is an important part of RF system design; however, in practice some degree of mismatch loss cannot be avoided.

The importance of impedance matching can be summarized in a few points:

- Maximum power is delivered to the load when the transmission line is matched at both the load and source ends. This configuration complies with the conjugate match condition.
- More signal power is transferred to the load, which increases the sensitivity of the rectifier in lower power levels.
- Some equipment can be damaged when too much power is reflected to the source.

However the selection of an appropriate matching network depends on the needs of the designer. Complexity of the design, availability of components, variable load conditions are some the factors that contribute to the selection procedure.

The most common impedance matching methods are the following:

- *L Network*: This network is one of the most commonly used antenna matching network. Different L sections exist such as inverted L section and reverse L section networks.
- *Pi Network*: The Pi network is used to match high source impedance to the low load impedance. These circuits are commonly used in vacuum tube RF power amplifiers which requires to match with low value antenna impedances.
- *Split Capacitor Network*: This network type is used to transform source impedance which is less than load impedance.
- *Coaxial Cable Balun Transformer*: The balun is a transformer which matches an unbalanced resistive source impedance with a balanced load.
- *Matching stubs*: The shorted stub can produce reactance of any value
- *Quarter wavelength transformer*: Also known as Q-section transformer connected between the transmission line and the antenna load.

The design of the matching network analyzed by this chapter will be based on L-Matching networks because it provides high matching efficiency with less complexity (amount of components) [41][[42][43].

3.2 Matching using *L* Networks

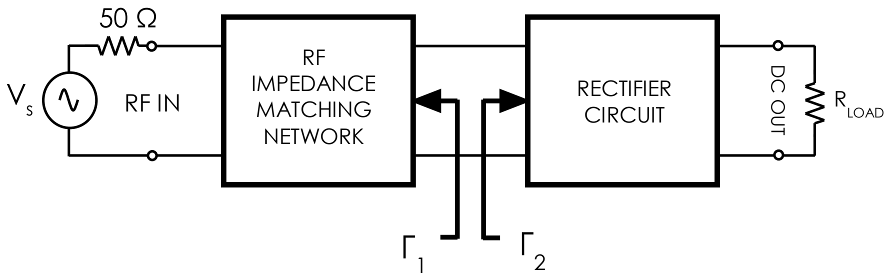

Figure 3.1: Impedance matching general circuit.

In Figure 3.1 a representation of the matching network's position is shown where at any frequency and input power level, the rectifier circuit will have an input reflection coefficient Γ_2, with magnitude p_2 and angle θ_2. In order to achieve a perfect impedance match and, subsequently, maximum power transfer at a given frequency Γ_1 must be set to be the complex conjugate of Γ_2.

At least two degrees of freedom are required in the L-matching network in order to transform the load impedance to the impedance seen at the input of the matching network [44]. This topology gets its name from the fact that the series and shunt elements of the matching circuit form an "L" shape. There are eight possible combinations of inductors and capacitors in this matching topology based on the two models presented in figure 3.2.

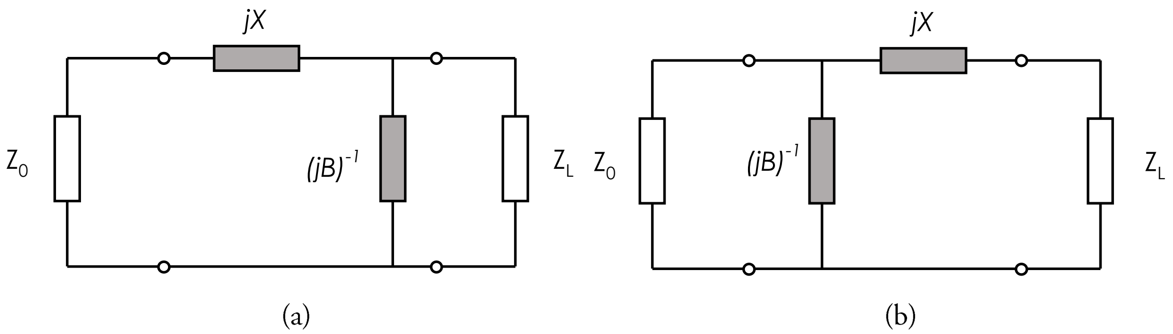

Figure 3.2: Matching network configuration for (a) $R_L > Z_0$ and (b) $R_L < Z_0$.

3.2.1 Analytical Solution for *L* Network Matching

From Figure 3.2 (a) where $R_L > Z_0$, the input impedance of the circuit will be given by:

$$Z_{in} = jX + \left(jB + \frac{1}{R_L + jX_L}\right)^{-1} \tag{3.1}$$

Through proper selection of X and B it is possible to equate Z_{in} and Z_0. Solving equation 3.1 for B and X by equating the imaginary and real parts respectively it is derived:

$$B = \frac{X_L \pm \sqrt{R_L/Z_0}\sqrt{R_L(R_L - Z_0) + X_L^2}}{R_L^2 + X_L^2} \tag{3.2}$$

and

$$X = \frac{1}{B} + \frac{Z_0 X_L}{R_L} - \frac{Z_0}{BR_L} \tag{3.3}$$

Since $R_L > Z_0$ the argument in the second square root of 3.2 must be a positive because B is a real number. There are always two solutions for B and respectively for X.

From Figure 3.2 (b) where $R_L<Z_0$, the input impedance of the circuit will be given by:

$$Z_{in} = Z_0 = \left(jB + \frac{1}{Z_L + jX}\right)^{-1} \quad (3.4)$$

Solving equation 3.4 by equating real and imaginary parts as before, B and X are obtained

$$X = \pm\sqrt{R_L(Z_0 - R_L) - X_L} \quad (3.5)$$

and

$$B = \pm\frac{1}{Z_0}\sqrt{\frac{Z_0 - R_L}{R_L}} \quad (3.6)$$

Since $R_L<Z_0$ the argument in the square root of 3.5 must be a positive number.

According to Pozar [44] all the aforementioned types of networks in this chapter are considered to be lossless or at least the losses can potentially be made extremely small with proper component choices.

3.3 Matching Network Design

In Chapter 2 it was observed that the input impedance of the rectifier varies when subjected to different power levels. This aspect makes the accurate matching of the impedance quite difficult because at different distances and hence power levels, the input impedance will change according to Figure 3.3. A selection/compromise must be made in order to satisfy the proposed scenario needs without limiting the performance of the rectifying circuit. In Figure 3.3 two sections are highlighted one in the 2.9 meter and on the 5.3 meter mark, these two represent the operating range of the proposed WPT system. The dedicated router must be able to power the IoT module within this range. This means that the impedance matching must be designed according to those values that correspond to the range conditions for a given transmission power. Specifically as the transmission range increases and the input power decreases the rectifier's impedance becomes more capacitive.

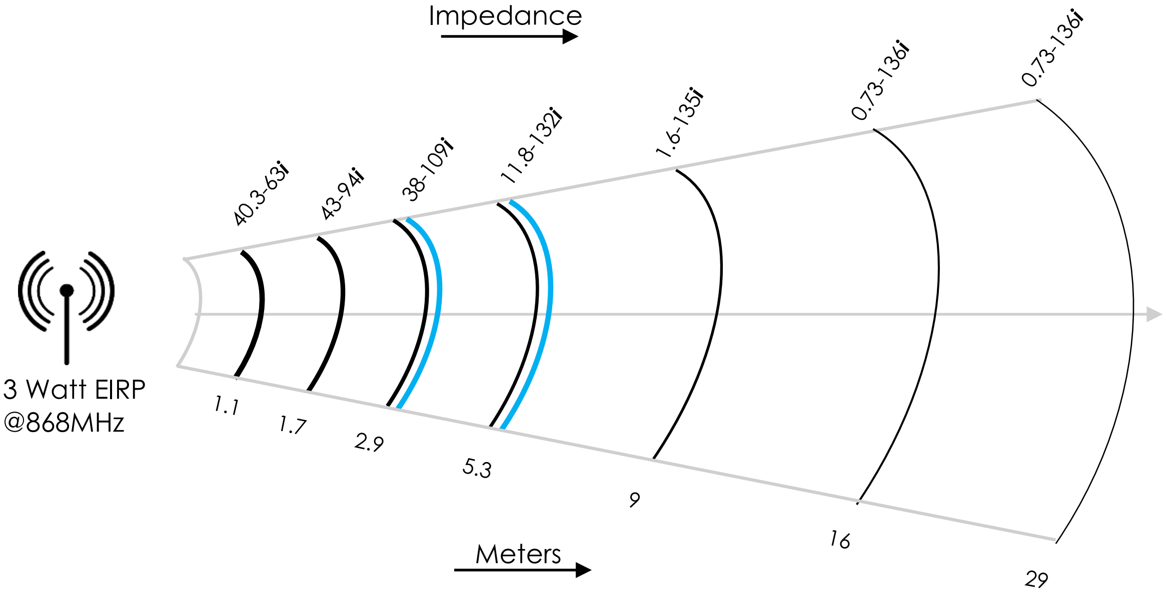

Figure 3.3: Schematic representation of the rectifier's input impedance in respect to transmission range, the highlighted region illustrate the proposed scenario (for the HSMS-2822 based rectifier)

Parameter	**Input Impedance** HSMS-2852	**Input Impedance** HSMS-2822	Units
Real[Z_{IN}]	10	25	Ω
Imag[Z_{IN}]	-218	-120	Ω
Input Power	-5	-5	dBm
Frequency	868	868	MHz

Table 3.1: Input Impedance characteristics of the proposed topologies

Two different topologies will be designed and implemented in hardware. The first one will be for the rectifying unit that can handle higher power levels for longer periods based on the HSMS-2822 Schottky diodes, while the second one will be the based on the HSMS-2852 Schottky diodes. Table 3.1 summarizes the impedance characteristics of each topology with the respective power and frequency operating conditions. For the target input power level of -5dBm, that the system is expected to operate under highest efficiency, the HSMS-2852 based rectifier presents a much more capacitive behavior than its counterpart.

3.3.1 Matching Network for the HSMS-2822 Rectifier

Following the analysis presented in the previous sections the designed L-matching network will be constituted by a capacitor (3.6 pF) and an inductor (26.6 nH) as shown in Figure 3.4 (a). The RF source will be replaced by an antenna with 50 ohm impedance.

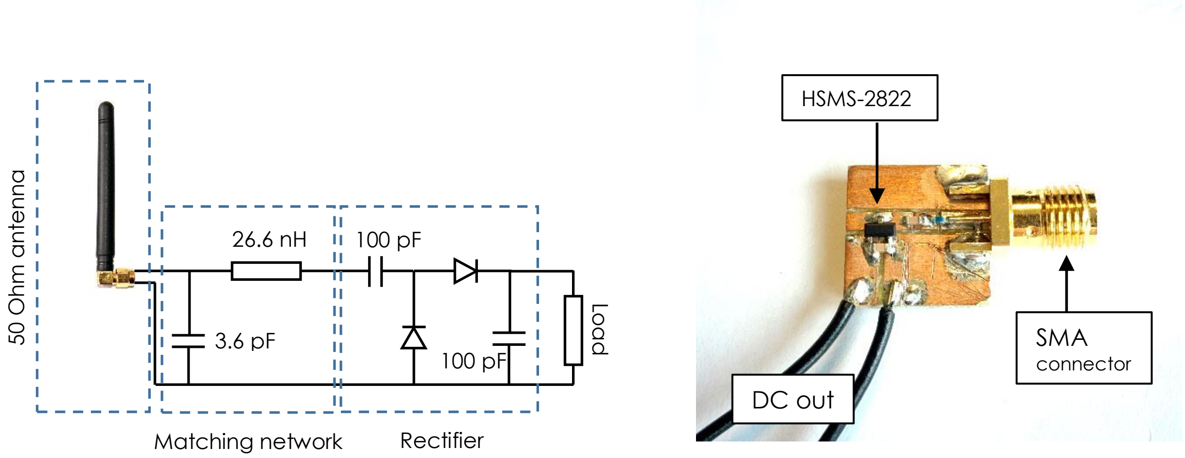

(a) (b)

Figure 3.4: (a) System topology with matching network for HSMS-2822 based rectifier, (b) Hardware implementation of the design.

Component	Value	Manufacturer Info.
CMATCH	3.3 pF	JOHANSON TECHNOLOGY 251R14S3R3BV4T
LMATCH	27 nH	MURATA LQG15HN27NJ02D
CRECTIFIER	100 pF	JOHANSON TECHNOLOGY 251R14S101GV4T
Diode	-	BROADCOM HSMS-2822-TR1G

Table 3.2: List of components used for the HSMS-2822 based rectifier

In the hardware implementation, from Table 3.2, it can be seen that there is a deviation between the commercial component values and the calculated ones presented in Figure 3.4 (a). This is caused by the unavailability of certain components in the market, therefore the components having closest approximation of these values were selected.

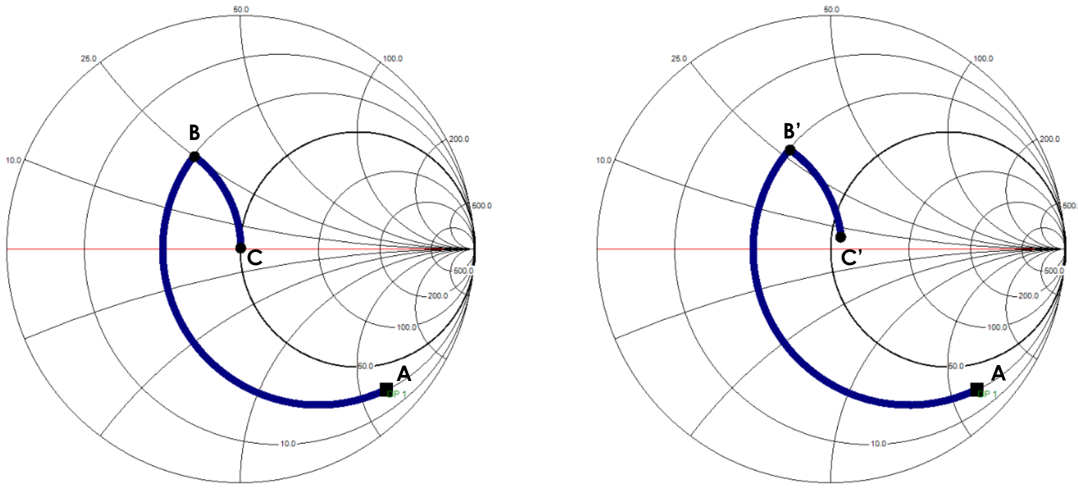

(a) (b)

Figure 3.5: (a) Ideal matching and (b) actual matching of the L network for the HSMS-2822 rectifier

In Figure 3.5 (a) the Smith chart representation [45] of the ideal matching procedure is summarized. Initially the input impedance of the rectifier is at 25-120j (point A). A series inductance of 26.6nH shifts the impedance clockwise to point B towards the inductive half cycle. In order to achieve matching to the 50 Ohm reference which is the center of the Smith chart, a shunt capacitor of 3.6pF must be added. Following the admittance cycles the capacitor moves the admittance to point C where the impedance is 50+0j ohms and the transmission line sees a matched load. However the precise matching of the load is very complicated since every millimeter of copper track and the PCB layout can induce parasitics at high frequencies. Apart from that, the unavailability of specific high frequency components and the use of approximate ones also influence the matching procedure. This phenomenon is presented in Figure 3.5 (b) where the use of a 27nH series inductor results into a point B' where a shunt capacitance of 3.3pF is not enough to approach the center of the smith chart. The final point is C' where the impedance is 55+7j meaning that the transmission line is not completely matched to the load. The implications of this slight mismatch will be discussed in the next chapters.

3.3.2 Matching Network for the HSMS-2852 Rectifier

A similar analysis presented in the previous sections will be implemented where the L-matching network will be comprised of a capacitor (7.3 pF) and an inductor (43.64 nH) as shown in Figure 3.6 (a). The RF source will be replaced by an antenna with 50 ohm impedance.

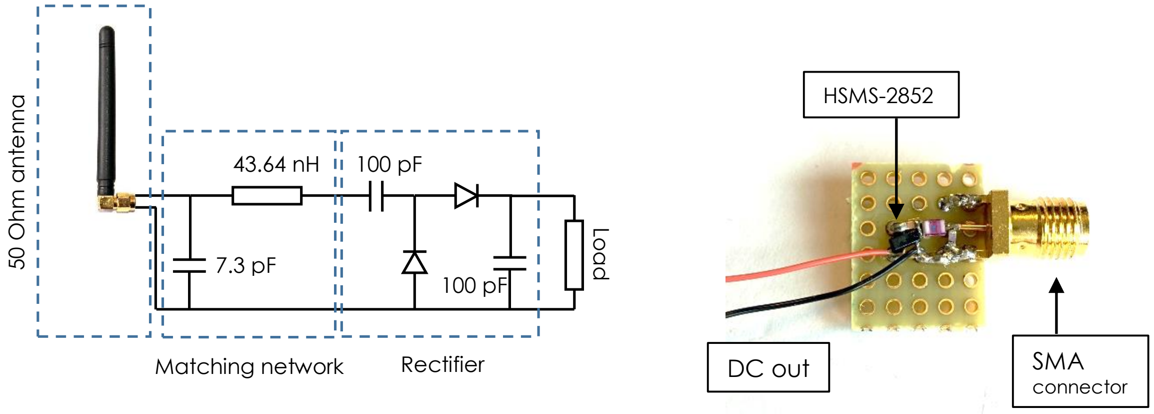

(a) (b)

Figure 3.6: (a) System topology with matching network for HSMS-2852 based rectifier, (b) Hardware implementation of the design.

Component	**Value**	**Manufacturer Info.**
CMATCH	7.5 pF	JOHANSON TECHNOLOGY 251R14S7R5CV4T
LMATCH	43 nH	COILCRAFT 0603HP-43NXGLU
CRECTIFIER	100 pF	JOHANSON TECHNOLOGY 251R14S101GV4T
Diode	-	AVAGO HSMS-2852-TR1G

Table 3.3: List of components used for the HSMS-2852 based rectifier

As stated in the previous section, again in hardware implementation it can be seen that there is a deviation between the commercial component values and the calculated ones presented in Figure 3.6 (a) and Table 3.3. This can be explained by the unavailability of specific components in the market, therefore the components having the closest approximation of these values were selected.

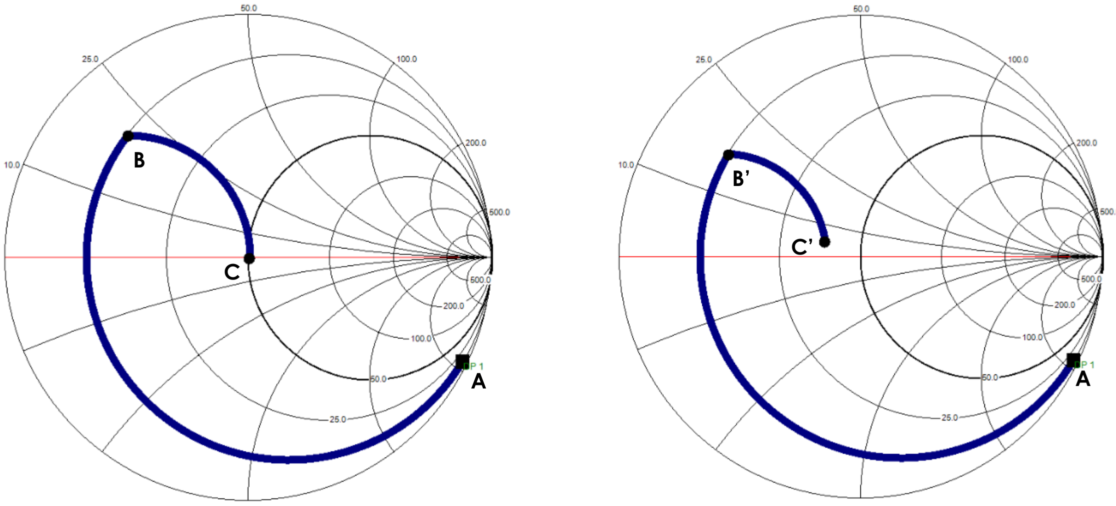

(a) (b)

Figure 3.7: (a) Ideal matching and (b) actual matching of the L network for the HSMS-2852 rectifier.

From Figure 3.7 (a) the ideal impedance matching is presented with a similar approach as shown in the previous section the series inductance of 43.64nH shifts the impedance to point B where a shunt capacitance moves the impedance to point C (50+0j) where the transmission line is precisely matched to the load. However the real implementation presented in Figure 3.7 (b) parasitics and the selection of slightly different components than the ideal ones result into a final impedance point C’ (39+5j). The implications of this slight mismatch will be presented in the next chapters.

3.4 Experimental Setup and Measurements

The test setup of the system is comprised of an HP 8648C Signal generator connected to the matching and rectifying circuits presented in Sections 3.3.1 and 3.3.2 by a 50 ohm transmission line. The signal generator replaces the receiving 50 Ohm antenna to ensure the accurate reproduction of the input signals. Then two calibrated multimeters are connected to a 5 kΩ load in a current and voltage measurement configuration as shown in Figure 3.8. Since the output is almost pure DC it is easy to calculate the power and thus the overall efficiency of the system.

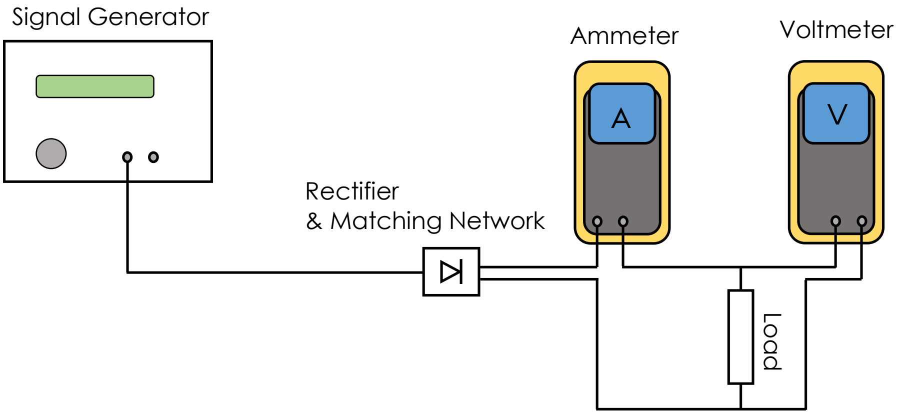

Figure 3.8.: Experimental set-up for efficiency measurements of different topologies.

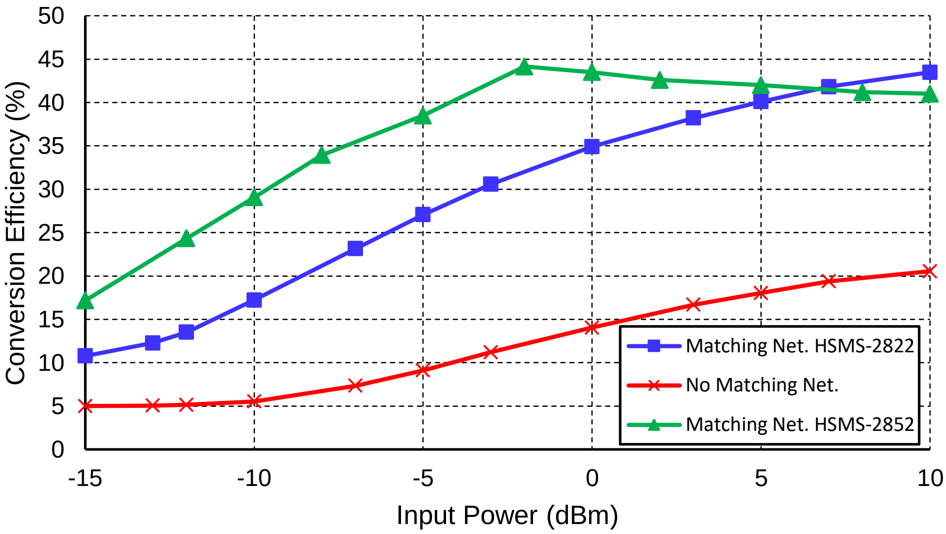

Figure 3.9: Overall conversion efficiency of different L-Matching networks presented in this chapter.

In Figure 3.9 the overall efficiency of the implemented topologies was measured and compared. The signal generator enables the accurate selection of different power levels spanning from -15 up to 10 dBm. For the majority of the examined power spectrum the HSMS-2852 based topology presented the highest efficiency peaking at 44% @-2dBm. As the power levels increase a slight decrease is noticed. The HSMS-2822 counterpart for the sub-zero dBm levels was consistently outperformed by the first. At 8 dBm it can be observed that the efficiencies of both topologies were equalized and after this mark the HSMS-2822 started to surpass the HSMS-2852 topology. This confirms the initial design notion that the HSMS-2822 performs better in a relatively high RF power environment. Finally the efficiency of the HSMS-2822 rectifier topology without a matching network was measured to realize the effect of the latter in the overall efficiency. This topology presented the lowest efficiency peaking at 20% @ 10 dBm.

3.5 Conclusions

In this chapter, the impedance matching techniques utilizing L-matching networks on a commercially available 3dBi 50 ohm whip antenna were presented. According to literature this type of matching networks constitute a circuit that provides less losses and complexity with enough accuracy to match the two different rectifier topologies. The matching network for the HSMS-2822 based rectifier showed a slight mismatch to the 50 ohm antenna with a final impedance of 55+7j. This is due to the components used that were slightly different from the calculated values and from parasitic elements in the PCB manufactured rectifier. The matching network for the HSMS-2852 based rectifier also showed a slight mismatch to the 50 ohm antenna with a final impedance of 39+5j for the same reasons that were previously described. Finally all the topologies were tested and the RF-DC conversion efficiency was measured. The HSMS-2852 based topology presented the highest efficiency peaking at 44% @-2dBm while the HSMS-2822 topology peaked at 43.5% @ 10dBm. Both of these topologies heavily outperformed the unmatched rectifier circuit as expected.

Chapter 4

Antenna Impedance Matching

In this chapter different antenna topologies will be investigated. Matching the Antenna impedance directly to the rectifiers input impedance has shown to improve compactness and efficiency while reducing manufacturing costs. Based on novice antenna designs and expanding on them, this chapter will introduce three antenna configurations. The proposed geometrical structure of these antennas makes it possible to tune their impedance to a value that matches approximately the input impedance of the rectifier. After performing simulations the characteristics of these antennas will be studied further through measurements on the manufactured PCB antennas.

4.1 Half-wave Dipole Antenna

In order to design the antenna configuration that was conceptualized, the basic "building blocks" first must be analyzed. The most basic element of these antennas is the single dipole antenna that was the initial point of reference for the study that took place in this thesis. Specifically the half-wave dipole antenna is one of the simplest and most widely used antennas [46]. It consists of two quarter-wavelength conductors as shown in Figure 4.1.

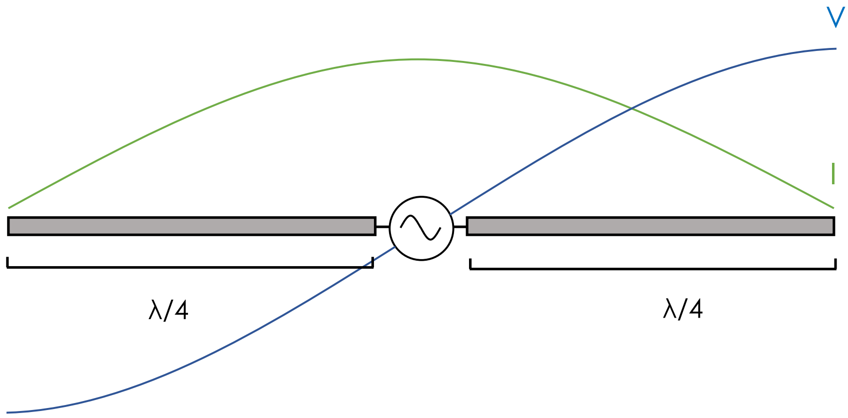

Figure 4.1: Half-wave Dipole antenna Voltage and Current distribution.

An antenna that has a length of one half wave and RF energy applied to it at its resonant frequency a standing wave develops on it. This standing wave consists of both current and voltage that are 90 degrees out of phase. The end result is a distribution of current that is at a maximum at the center and a distribution of voltage that is at a maximum at the ends.

The input impedance of this type of antenna could be calculated by using the induced EMF method. For dipole lengths of half a wave length according to [47] a fitting method applied to a first fitting can approximate the antenna's impedance:

$$\begin{gathered} \mathrm{Z_{in}} = [122.65 - 204.1\mathrm{k_0 l} + 110(\mathrm{k_0 l})^2 \\ -\mathbf{j}[120\left(\ln\frac{2\mathrm{l}}{\mathrm{a}} - 1\right)\cot\mathrm{k_0 l} - 162.5 + 140\mathrm{k_0 l} - 40(\mathrm{k_0 l})^2 \end{gathered} \tag{4.1}$$

For $(1.3 \leq k_0 \leq 1.7)$ and $(0.001588 \leq a/\lambda_0 \leq 0.009525)$ where a is the radius of the wire.

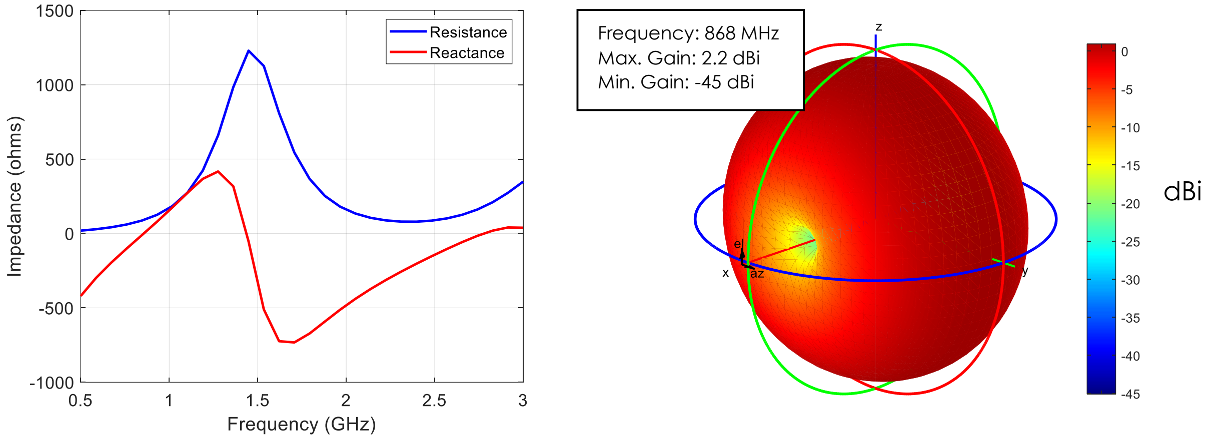

(a) (b)

Figure 4.2: Matlab Antenna Toolbox generated results (a) Half-wave Dipole's impedance versus frequency, (b) Radiation pattern.

Using the Matlab RF and Antenna Toolboxes the impedance of such an antenna can be approximated as well as its characteristics. From Figure 4.2 (a) for frequencies below GHz the antennas impedance has predominantly capacitive behavior while its resistance is quite larger than the required value. The radiation pattern of this antenna as shown in Figure 4.2 (b) is omni-directional with a maximum gain of 2.2 dBi which is quite acceptable for an antenna of this size. At the operating frequency of 868 MHz the half-wave dipole antenna has an impedance of 95.4+12j which is lower than the desired values presented in Chapter 3.

4.2 Loop Antenna

Since the input impedance of the rectifier is mostly capacitive the fabricated antenna's impedance must be inductive to match it. The loop antenna poses as a viable solution because of its shape it can be perceived as a series electrical circuit consisting of an inductance and a resistor [48], Figure 4.3 (b).

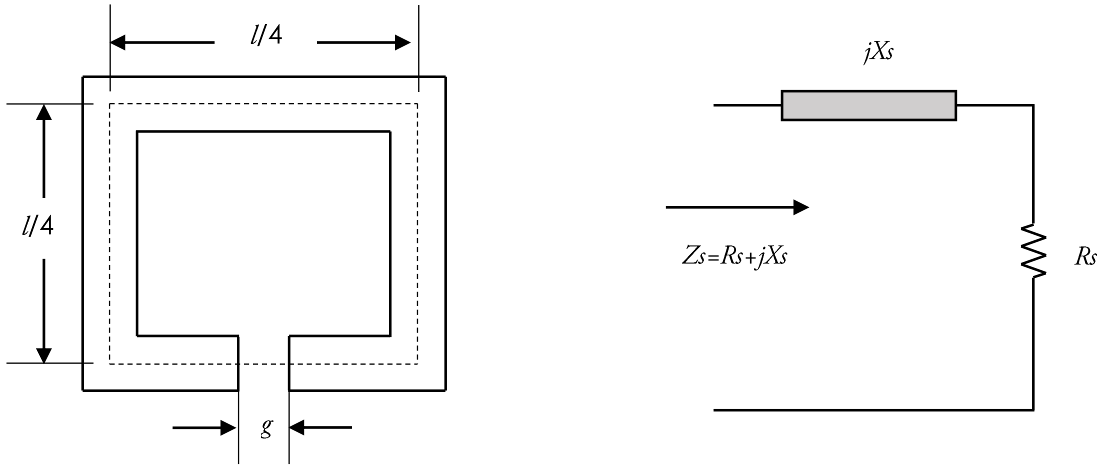

(a) (b)

Figure 4.3: (a) Square strip loop antenna (b) Equivalent series impedance circuit.

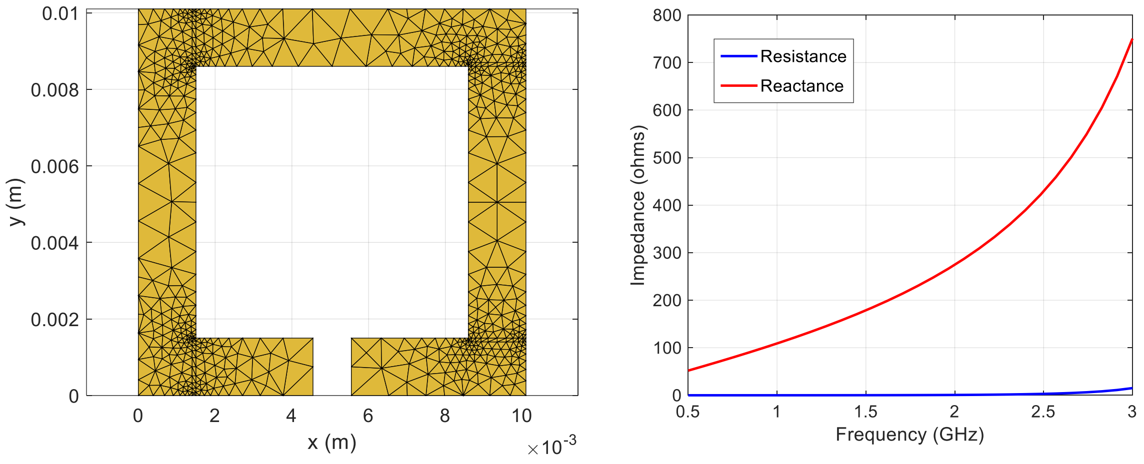

(a) (b)

Figure 4.4: (a) Designed Square strip small loop antenna with perimeter smaller than a tenth of a wavelength @868 MHz (b) Loop antenna impedance versus frequency.

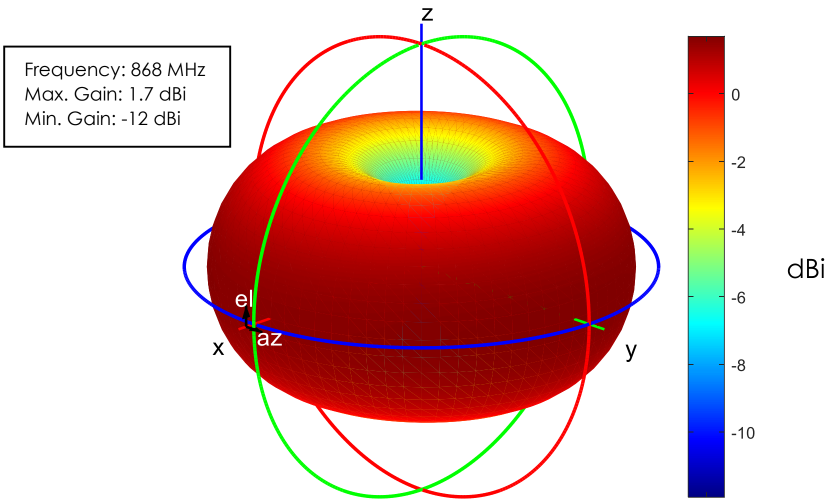

Figure 4.5: Radiation pattern of the designed small loop antenna

The square loop inductance L can be calculated by the following formula [46]:

$$\mathrm{L} = \frac{\mu_0 \mathrm{P}}{2\pi} \ln\left(\frac{P}{2W}\right) \tag{4.2}$$

Where P is the perimeter of the loop and W is the width of the strip.

The small loop antenna requires a wavelength smaller than a tenth of the wavelength at 868MHz (0.3454 m). This requirement confines this particular antenna design in terms of length and therefore with a single loop there isn't the option to fine tune the antennas impedance exactly to match the input impedance of the rectifier. In order to design such an antenna that will match its impedance with another complex impedance there must a relative freedom in the number of geometrical features.

From Figure 4.4 (b) where the antenna's complex impedance is simulated it can be seen that for frequencies bellow 1 GHz the impedance is inductive, however not to an extend that will satisfy all the tested rectifying topologies.

4.3 Custom Designed Antennas

In this section novel and compact antenna designs will be presented that present greater geometrical feature freedom than the ones presented in the previous sections. The first iteration of the custom antenna design is based on a combination of the two antennas presented in sections 4.1 and 4.2 that will try to match the input impedance of the High Power Rectifying (HPR) topology. However the need to utilize antennas of smaller sizes for the proposed sensors steered the focus of the design process to the modified rectangular loop antenna presented by [49]. Similarly there will be designs for both low power and high power rectifying topologies.

4.3.1 Custom Antenna #1 for HPR

This proposed design combines characteristics of the half-wavelength dipole antenna which is one of the most basic antenna designs with a small loop antenna. Since the dipole antenna cannot be tuned to the desired input impedance by simply adjusting its length, the inductive load of a loop section will be added as shown in Figure 4.6.

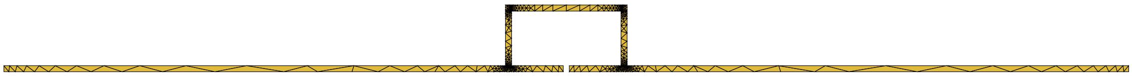

Figure 4.6: Custom designed loop-dipole antenna as simulated in Partial Differential Equation Toolbox™.

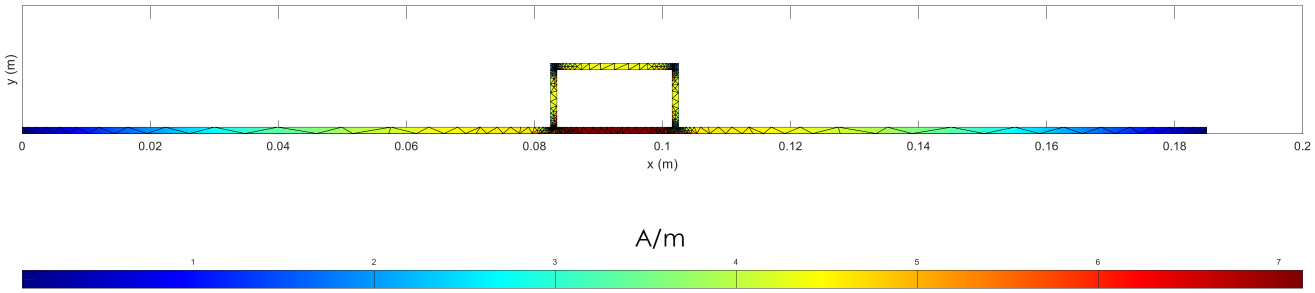

Figure 4.7: Current Distribution of the designed antenna from Matlab PDE Toolbox™.

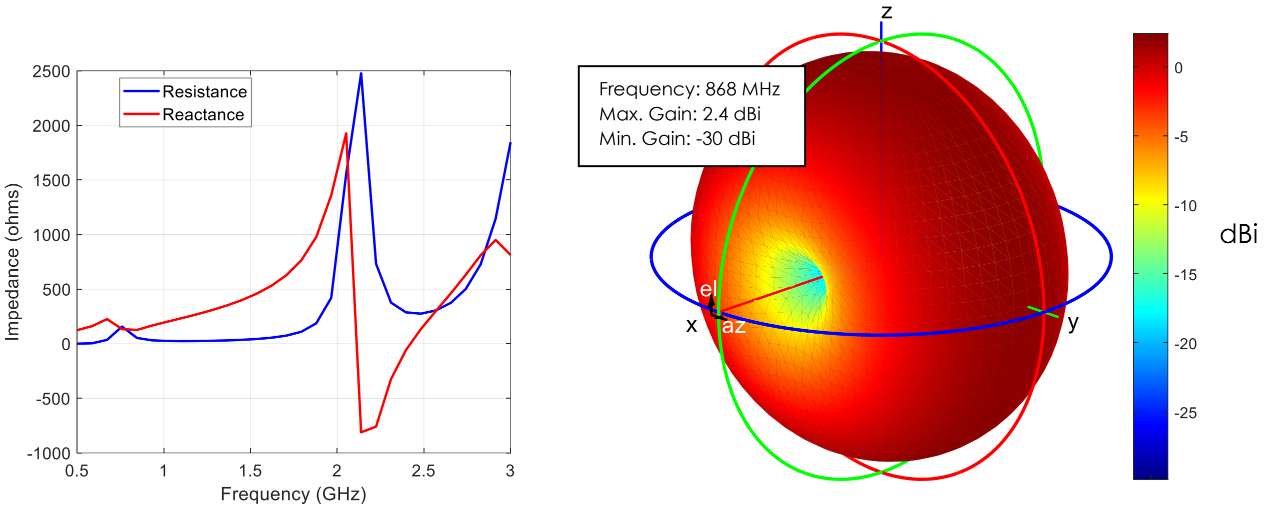

(a) (b)

Figure 4.8: (a) Custom antenna impedance versus frequency, (b) Radiation pattern.

The geometrical features of this antenna enables its input impedance to approximately match the complex impedance of the rectifier. From Figures 4.7 and 4.8 there can be observed that the characteristics of this antenna are suitable for operation at 868 MHz with significant gain (2.4 dBi) and impedance close to the requirements.

However there will be losses caused by impedance mismatches. The efficiency of power received by the proposed antenna due to a non-perfect impedance match according to [49] can be described as:

$$\mathrm{Eff}_{\mathrm{match}} = 1 - |\Gamma|^2 = 1 - \left|\frac{Z_{\mathrm{Ant}} - Z^*_{\mathrm{Rect}}}{Z_{\mathrm{Ant}} + Z_{\mathrm{Rect}}}\right|^2 \qquad (4.3)$$

The antenna's impedance is 46+139j Ohms slightly different from the 25-120j Ohms of the HSMS-2822 rectifier. Therefore the losses due to mismatch will be 17%.

4.3.2 Custom Antenna #2 for LPR

This section introduces an antenna presented in [20] by S. Keyrouz and fits the purpose of conjugately match the impedance of the HSMS-2852 rectifier. This antenna can be categorized as a modified rectangular loop antenna that is comprised of additional loops to control its input impedance. The topology of such an antenna is shown in Figure 4.9. The radiation characteristics are solely influenced by the outer antenna length and width. The main advantage of this type of antenna is its compact size and the ability to fine tune its impedance with the internal loops. The antennas dimensions are included in the appendix.

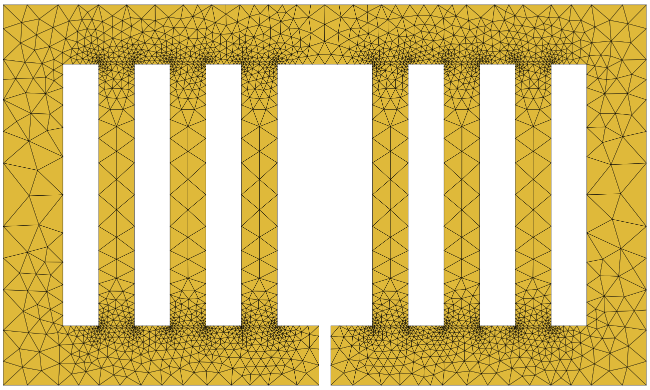

Figure 4.9: Modified rectangular loop topology as simulated from Matlab PDE Toolbox™.

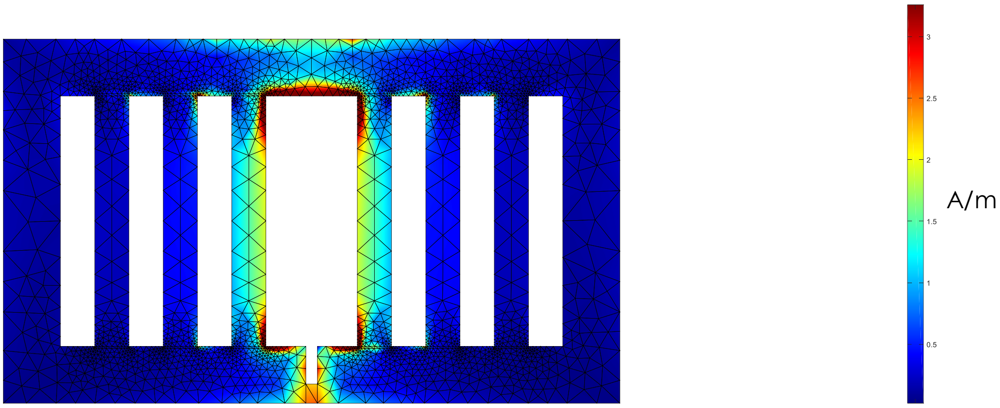

Figure 4.10: Custom antenna #2 current distribution from Matlab PDE Toolbox™.

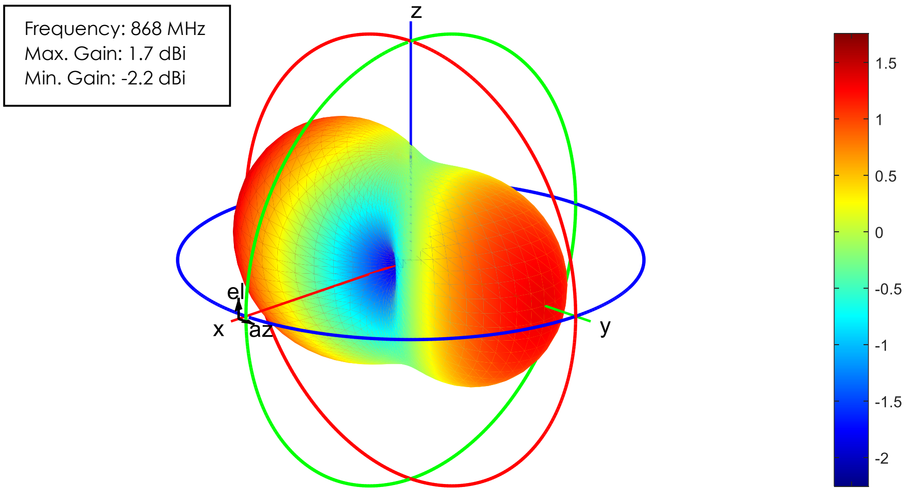

Figure 4.11: Custom antenna #2 radiation pattern from Matlab PDE Toolbox™.

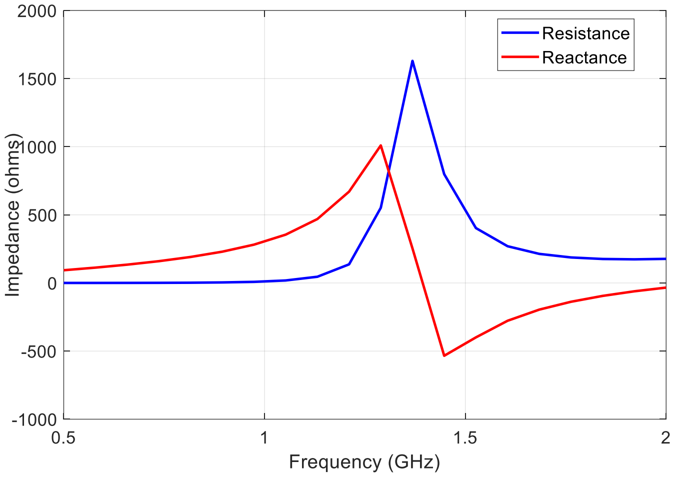

Figure 4.12: Custom antenna #2 impedance sweep from Matlab PDE Toolbox™.

From Figure 4.10 the current distribution can be examined. It can be seen that the inner loop dominates the current density and consequently the impedance. The outer loop determine the radiation efficiency of the antenna while the inner arms are used to fine tune its impedance [47].

The losses due to a slight mismatch between the antenna impedance and the HSMS-2852 based rectifier according to 4.3 is 8%. Which is already a significant improvement over the custom antenna #1 counterpart presented in the previous section.

4.3.3 Custom Antenna #3 for HPR

In the previous section a modified rectangular loop antenna that was designed for the low power HSMS-2852 based rectifier was presented. This section will introduce a novice antenna that used the design techniques of the custom antenna #2, to match the impedance of the high power HSMS-2822 rectifier. The same principles apply to this design, the radiation characteristics are predominantly influenced by the outer antenna length and width. This antenna will also use an FR4 substrate and the dimensions will be included in the appendix.

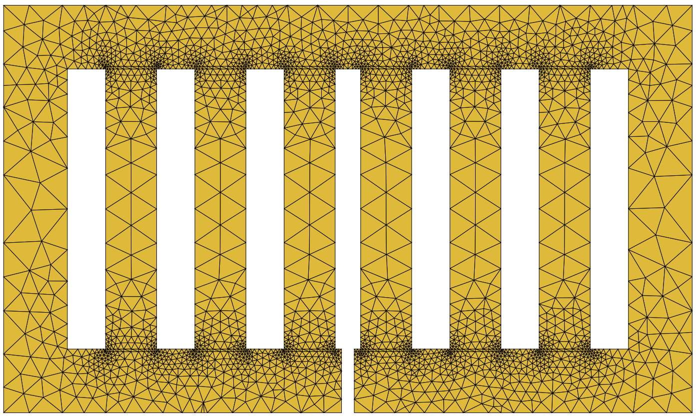

Figure 4.13: Custom antenna #3 topology as simulated from Matlab PDE Toolbox™.

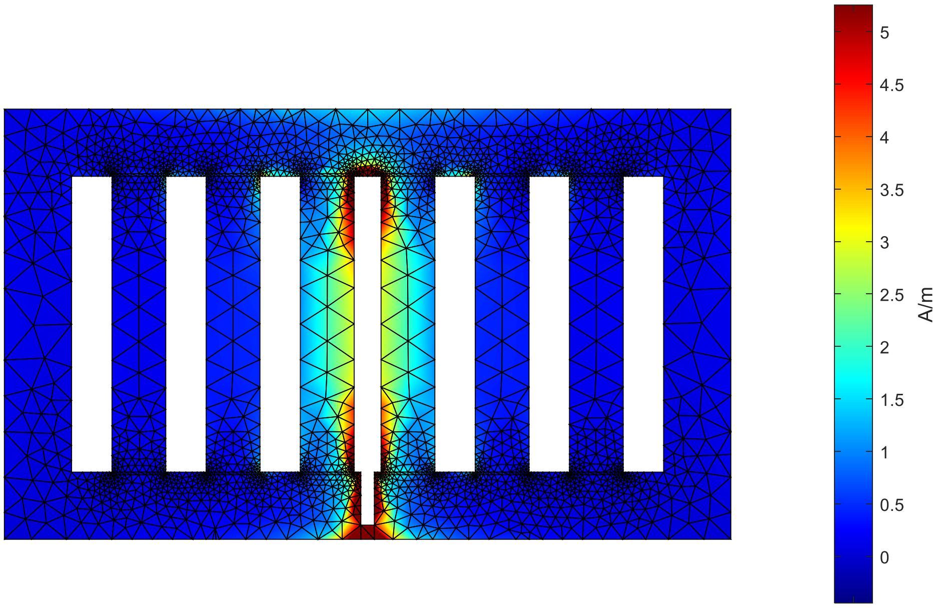

Figure 4.14: Custom antenna #3 current distribution from Matlab PDE Toolbox™.

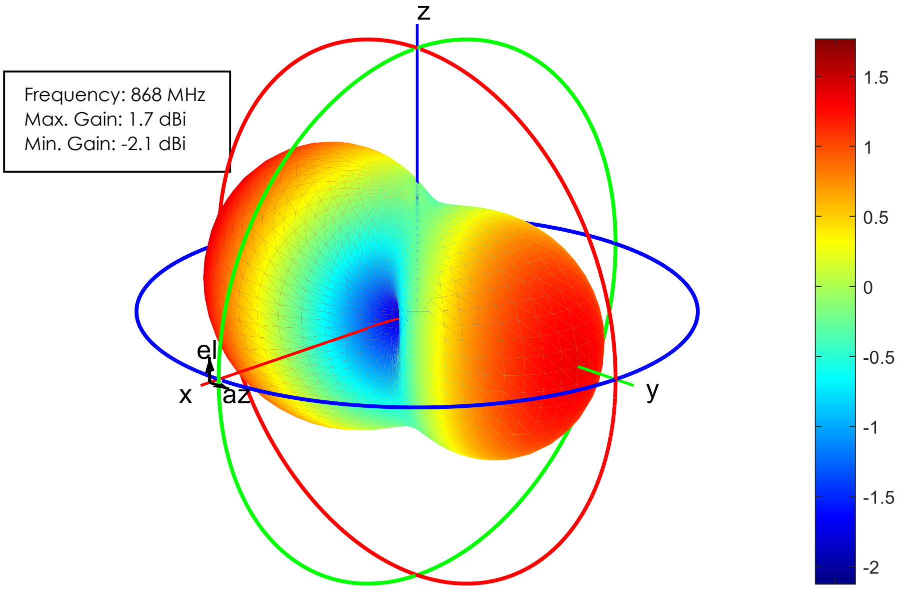

Figure 4.15: Custom antenna #3 radiation pattern from Matlab PDE Toolbox™.

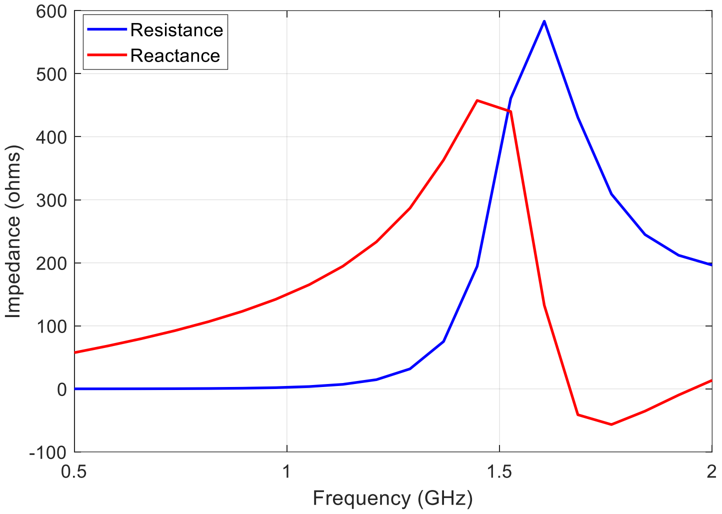

Figure 4.16: Custom antenna #3 impedance versus frequency.

As shown in Figure 4.14 the antenna's main loop draws the maximum current density, thus its impedance will be influenced by the geometrical features of that loop. Finally the losses due to a slight mismatch between the antenna impedance and the HSMS-2822 based rectifier according to the 4.3 Formula is 12%. Which is, again, an improvement over the custom antenna #1 counterpart presented in the previous section.

4.4 Antenna Lab Measurements

The antennas presented in the previous section were milled on top of an FR4 substrate in a PCB configuration. Without soldering the SMD components of the rectifier at the feed gap of the antennas, SMA connectors were installed instead to measure the return loss at 868MHz by connecting them to the network analyzer. The return loss represents how much power is reflected from the antenna and is the negative of the reflection coefficient S_{11}. The Figures bellow show the measured return loss for all the antennas examined.

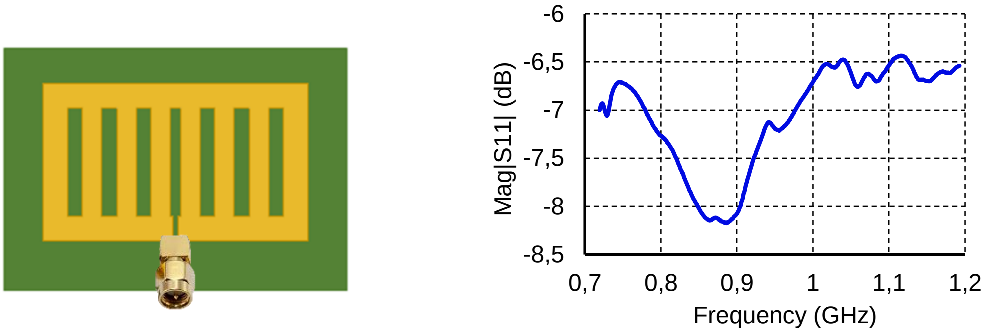

(a) (b)

Figure 4.17: (a) Measurement configuration of custom antenna #3 (b) Return loss versus frequency.

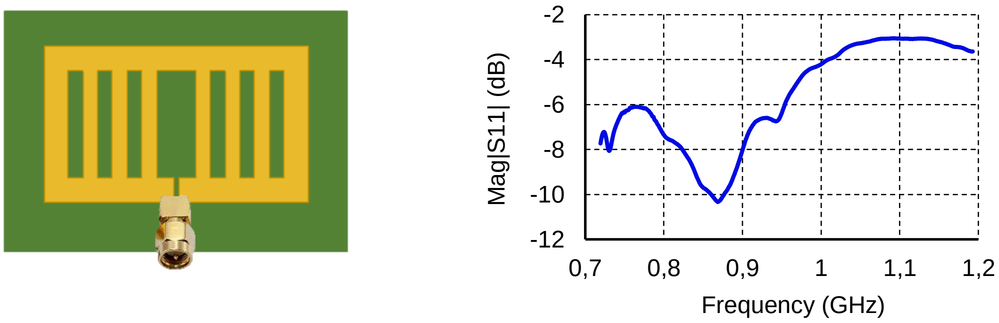

(a) (b)

Figure 4.18: (a) Measurement configuration of custom antenna #2 (b) Return loss versus frequency.

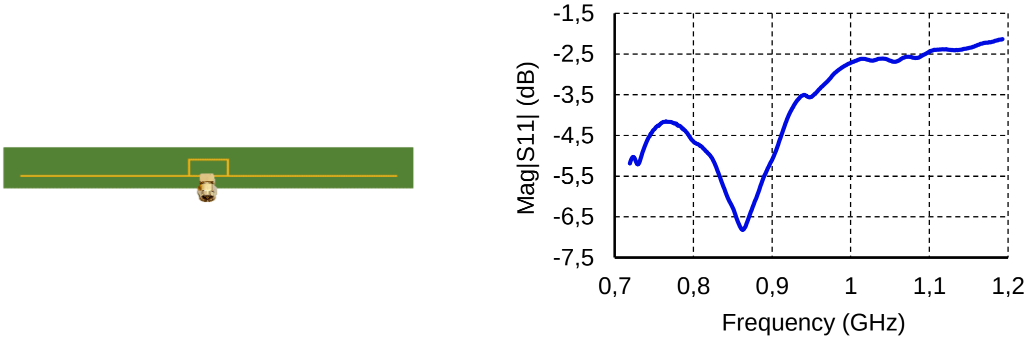

(a) (b)

Figure 4.19: (a) Measurement configuration of custom antenna #1 (b) Return loss versus frequency.

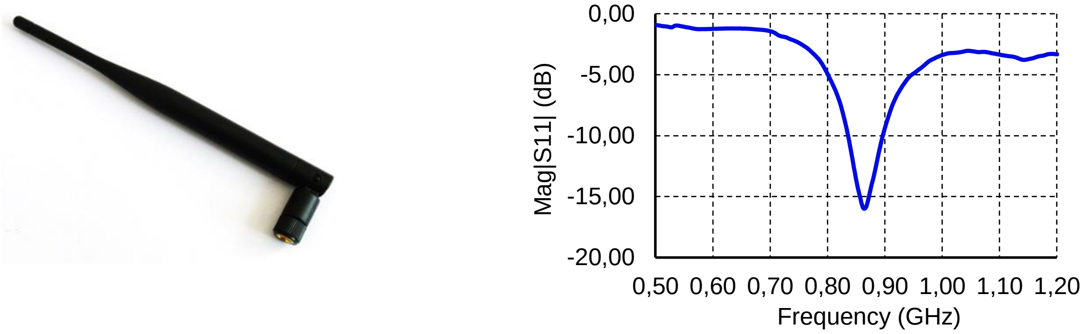

(a) (b)

Figure 4.20: (a) 3dBi commercial whip antenna (b) Return loss versus frequency.

From the graphs in Figures 4.17 to 4.20 it can be observed that the fabricated antennas show a wide band behavior for frequencies bellow 1.5 GHz when compared to the commercial whip antenna which is narrowband at 868 MHz.

4.5 Conclusions

In this Chapter, the design process behind the goal to match the impedance of the antenna to the input impedance of the rectifier is introduced. Loop antennas are potential candidates because of their inductance, which directly can match the capacitive behavior of the rectifier. However their geometrical features are limited and require other topologies in conjunction to provide the results that are needed. The first custom antenna design, through Matlab PDE toolbox simulations and measurements, showed adequate RF characteristics but presented the highest impedance mismatch of 17% and the highest gain.

The second custom antenna design, aimed for low power RF environment, consists of vertical arms inside the loop antenna to help tune the impedance with more accuracy. This design showed 8% impedance mismatch with the impedance of the rectifier and effective gain ranging from 1 to 1.7 dBi.

Finally, the last custom antenna design, aimed for higher power RF environment, is based on the design of the second antenna but modified to match the impedance of the HSMS-2822 based rectifier. Simulations presented a mismatch of 12% for this topology with similar RF properties as the second antenna design.

Chapter 5

Complete Harvesting System and Testing

This chapter introduces the integration of a commercially available power management IC to the existing harvesting infrastructure to offer a more complete system in terms of options and robustness. This circuit is based on a TI evaluation board and contains a nano-powered boost and buck converter that enable the storage of energy to a battery/capacitor. Finally the total system testing, consisting of efficiency measurements at different stages of the configuration, will be analyzed in order to identify the performance bottlenecks of the power harvesting system.

5.1 Power Management Integrated Circuit

The power management BQ 25570 IC is a micro-harvester specifically designed to efficiently to draw microwatts to milliwatts of power generated by high output impedance DC sources likes harvesting antennas, photovoltaic panels, piezo-electric and thermal electric generators [50].The boost charger is powered from the boost output, VSTOR as shown in Figure 5.1. Once the VSTOR voltage is above a threshold (1.8 V), the boost charger can extract power from low voltage output harvesters such as thermoelectric generators or small solar panels that generate voltages down to 100 mV (VIN_DC). At lower power levels where VSTOR is less than 100 mV, the cold start circuit needs at least 330 mV (VIN) to charge the VSTOR up to 1.8 V.

This power management circuit also contains a programmable maximum power point tracking sampling network to maximize the power harvested. The input open circuit voltage is periodically sampled every 16 seconds by disabling the boost converter for 256ms and can be managed by the VOC_SAMP jumper at 80% and 50% sampling or by using external resistors. The sampled voltage is held via internal sampling circuitry and stored in an external capacitor on the VREF_SAMP pin. Furthermore, BQ25570 has two different DC output rails to support a variety of energy storage elements. The nature of the proposed system depends on a sporadic or time-varying harvesting fashion. This kind of system will typically need some type of energy storage element, such as a re-chargeable battery, super capacitor, or conventional capacitor. The storage element provides constant power to the system. The storage element also allows the system to handle any peak currents that cannot directly come from the input source. To prevent damage to the battery, both maximum and minimum voltages are compared against the internally set under-voltage and user programmable over-voltage values [50].

The integrated buck converter shown in Figure 5.1 is controlling the output voltage to drive different components (sensors, super-capacitors) and is powered from VSTOR. Finally the power management IC will be embedded on the TI evaluation board which offers all the necessary test points, output pins and a certified design architecture that limits EMC. For a more compact system a custom PCB design can be used, however this was beyond the scope of this research project.

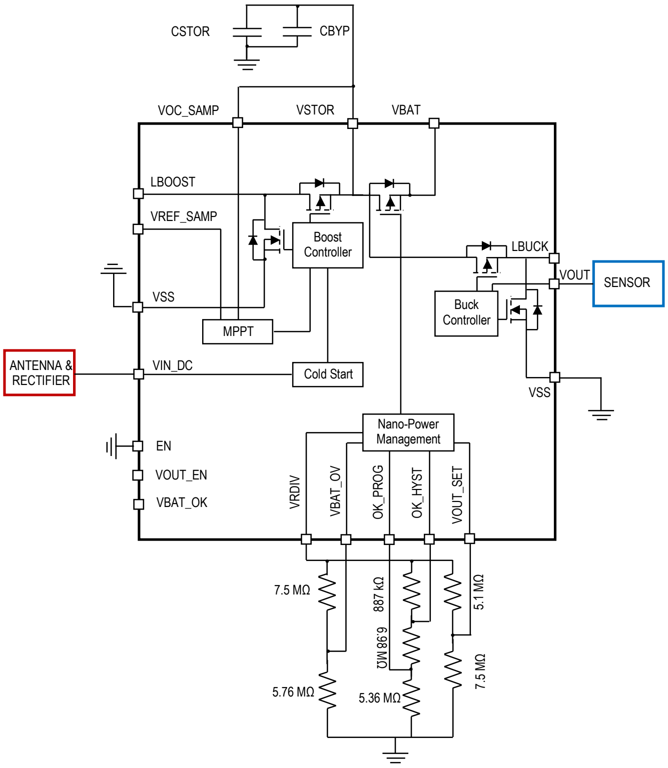

Figure 5.1: Application Schematic of the BQ25570 Power Management IC .

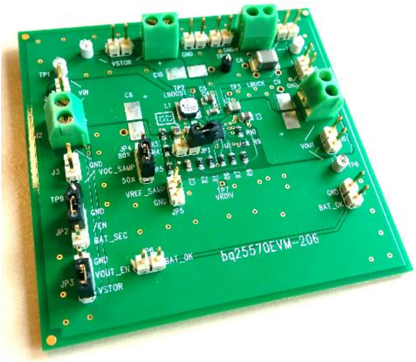

Figure 5.2: TI Evaluation Board .

5.2 Energy Storage Device

The energy storage device that will be used needs to be able of being fully charged, even by a low capacity source, and conserving energy for a relatively long period without leaking it. Furthermore, the storage device's performance needs to be maintained even after it is charged and discharged many times to reduce maintenance and replacement costs. Batteries and electric double-layer capacitors of different types have advantages and drawbacks, and only a small number of these devices can satisfy all conditions suitable for dedicated energy harvesting. There are a number of alternatives solutions for energy storage, and their choice depends on each application. The three most common storage options are the following:

- *Capacitor*: In applications that the required output current is very low and there are short interruptions of the power source (dedicated RF power transfer), capacitors may be used.
- *Super-capacitor*: The super-capacitors, compared with classic capacitors provide higher levels of capacity and can provide power for a longer period.
- *Rechargeable battery*: The rechargeable batteries are capable of storing high energy levels. They can be utilized to provide high power levels over a long period. They can be recharged when the energy harvesting device becomes available again. However their life expectancy is significantly influenced by the frequent charge/discharge cycles.

Battery life is directly linked to how deep the battery is cycled each time. If, for example, a battery is discharged to 50% every day, it will last about twice as long as if it is cycled to 90% Depth of Discharge (DOD). Of course, there are some practical limitations on this. The most practical number to use is 50% DOD on a constant basis. This does not imply that it cannot be exceeded once in a while. Also, there is an upper limit for a battery that is continually cycled 5% or less will usually not last as long as one cycled down to 10% [51]. This can be attributed to shallow cycles as the graph bellow shows how lifespan is affected by depth of discharge. Figure 5.3 is for a Lithium-ion battery, but all lead-acid batteries will have a similar shape of curve, although the number of cycles will vary. All these factors, along with the nature of the proposed system where several charge/discharge cycles will be enforced since the device will be relatively close to the transmitter, makes the rechargeable battery not a suitable option. The vicinity of the receiver circuit offers the possibility of a smaller storage element that doesn't need a lot of time charge even if it is completely empty.

5.2.1 Super-capacitor as a Storage Unit

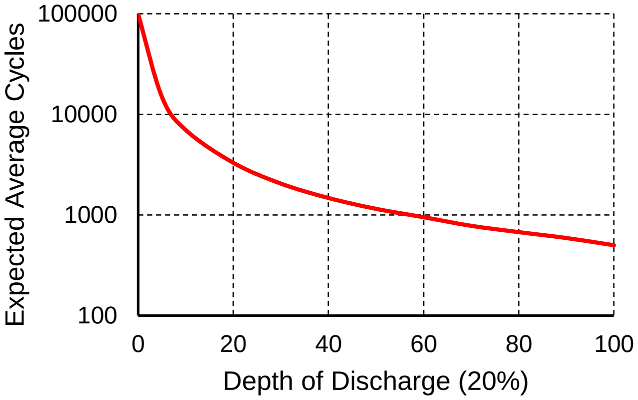

Figure 5.3: Depth of discharge vs Cycle Life for Li-ion batteries [52].

Super-capacitors, on the other hand, are electrical double-layer capacitors that are capable of storing and discharging energy very quickly and effectively. The electrodes are kept apart by a porous separator that allows ions in solution in the electrolyte to pass through, providing charge transport as shown in Figure 5.4. The super-capacitor can be charged and discharged a virtually unlimited number of times. Unlike the classic electrochemical battery, which has a defined cycle life, there is little deterioration by cycling a super-capacitor, which is really beneficial for the proposed application. Super-capacitors also age better than batteries [53]. Under normal operation, a super-capacitor degrades from the original 100% capacity to 80% in 10 years. Applying higher voltages than specified shortens the lifetime. Finally the double layer capacitor is a durable performer in both hot and cold temperatures, a significant advantage that batteries cannot meet easily.

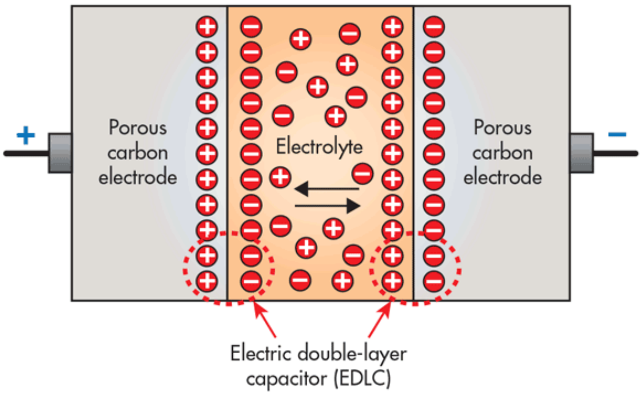

Figure 5.4: Separation of discharge distance in double layer capacitors [54].

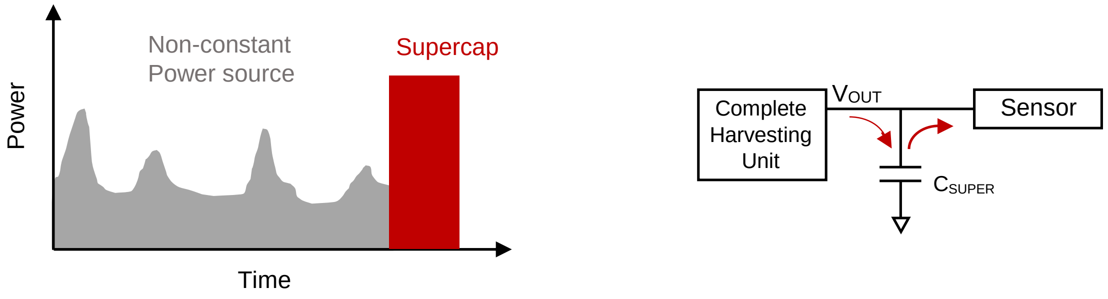

(a) (b)

Figure 5.5: (a) Power harvesting and consumption scheme for an autonomous sensor (b) Power flow of the system with a supercapacitor as a storage device.

The temperature sensor requires a burst of power drawn once every 30 seconds. The supercapacitor is capable of providing this power even when there is a non-constant power source available (sensor device movement or dynamic landscape) as shown in Figure 5.5 (a). However its position in the proposed system being as close as possible to the load/sensor as shown in Figure 5.5 (b) makes is enter subjected to a "cold-start" when the supercapacitor is empty. During this phase the V_{OUT} will start powering the sensor only when the supercapacitor voltage have reached the 1.5V mark (controlled by the resistor network of BQ25570). For the specifications of the design system there weren't commercially available EDSL capacitors smaller than 0.01F and low equivalent series resistance (ESR). This quite large amount of capacitance would increase the "cold-start" duration of the system and the extra capacity is not quite necessary since a dedicated router will be in the vicinity providing RF power in a calculated and predictable manner. For this reason smaller electrolytic capacitors with low ESR will also be examined in the next section.

5.2.2 Electrolytic capacitor as a Storage Unit

Electrolytic capacitors are polarized capacitors whose anode consists of a metallic material that creates an oxide layer through anodization. This oxide layer plays the role of the dielectric in the electrolytic capacitor. The surface of this oxide layer is covered by a solid or non-solid electrolyte, acting as the second electrode (cathode) of the capacitor [55]. This kind of capacitors have a significantly higher capacitance-voltage product (CV) when compared to film capacitors or ceramic capacitors, but a smaller CV value than super-capacitors. These capacitors present some problems. The most known one is their polarity. Anodization of aluminum is a polarity-dependent procedure. The capacitor must always be connected in the polarity that anodizes the aluminum. A reversed polarity will cause the electrolyte to deteriorate the surface oxide, which results in a shorted capacitor.

Another option could be a ceramic capacitor which present the lowest ESR and has a more compact footprint. However their capacitance drops with bias voltage. The higher the voltage across their terminals, the lower their effective capacitance. Also their packaging is mostly surface mount device (SMD) which makes the replacement more complicated than the electrolytic capacitor.

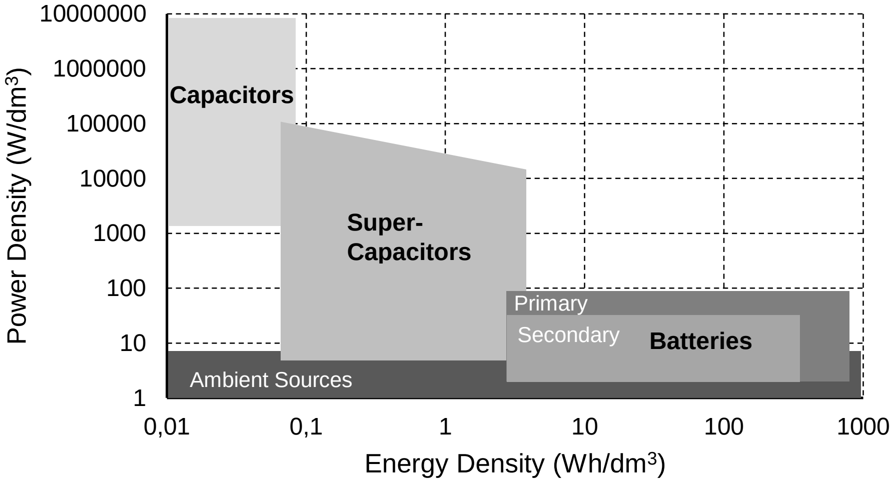

Figure 5.6: Ragone Plot of the power density vs Energy density for storage units [56][57].

Figure 5.6 presents a general chart of the power versus the energy density of different energy storage elements. As it can be seen batteries offer great energy density but luck power density. Supercapacitors lay somewhere in the middle offering both energy and power density for their respective volume. On the other hand capacitors offer high power density while presenting low energy density. Since the application that this thesis examines is based on frequent charge discharge cycles that doesn't require the storage element to hold large amounts of energy for a long time, capacitors can be a cost effective alternative. The capacitor will be connected to the CSTOR pins of the BQ25570.

5.3 System Operation and Capacitor Sizing

In practice the sensor being the power consuming component of the system, will not operate continuously. According to the proposed scenario of a wireless autonomous sensor measuring the temperature inside a patient room, the sensor will perform a sequence of temperature measurement and information relay lasting one second followed by an off state for 29 seconds. This scheme is known as duty cycling and can be applied for both transmission and generation as presented in Figure 5.7.

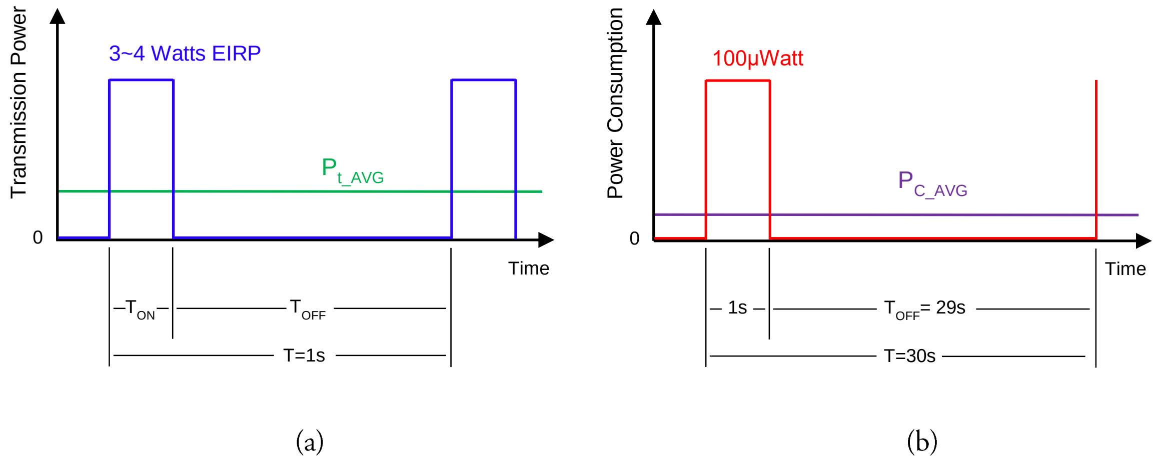

(a) (b)

Figure 5.7: (a) Time diagram of Power transmission duty cycling to lower the average transmitted power, (b) Time diagram of Sensor's power consumption.

The duty cycling of transmission power plays a crucial role in lowering the average power levels in order to comply with several regulations that are different around the globe according to [58]. Some countries allow for specific duty cycles (<15%) of transmission power for any 200ms period. To maintain autonomous and sustainable operation of the sensor, the average harvested power (P_{H_AVG}) must comply with the following:

$$P_{H\_AVG} \geq P_{C\_AVG} \tag{5.1}$$

Where P_{C_AVG} includes all the intermittent losses and the leakage of the storage unit. P_{H_AVG} depends on the efficiency of the harvesting system and its physical location. The storage unit must aid the power transfer to the sensor when the harvested power is lower than the consumed power.

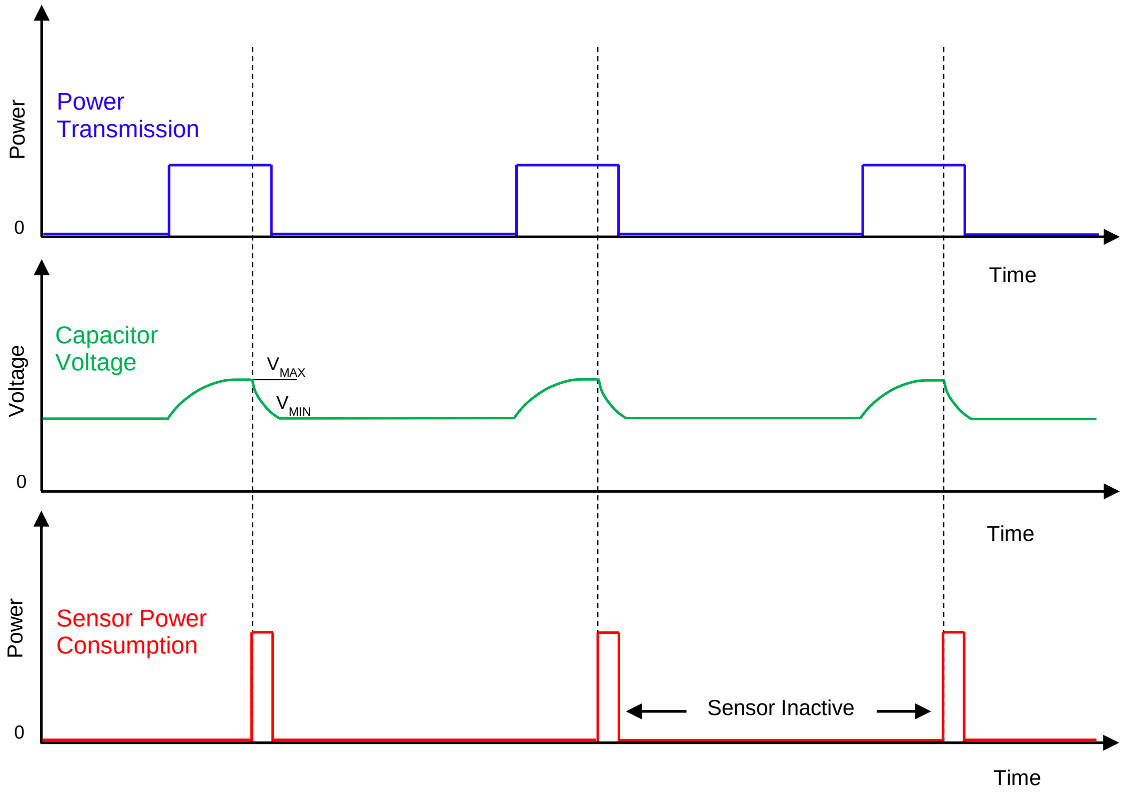

Figure 5.8: Time scheduling graphs for the proposed scenario of operation containing transmission, consumption and storage element voltage (capacitor) Schemes.

Figure 5.8 illustrates a scenario of operation that was examined and can easily showcase the basic principle of operation. A major advantage of such a system is its versatility, meaning the system's parameters like transmission power (duty cycling and power levels) storage element (capacity and voltage levels) can be adjusted to the sensor consumption scheme.

In a low data rate autonomous wireless sensors, a capacitor can be used as an alternative choice for energy storage. The amount of energy stored in the capacitor is equal to

$$E_{cap} = \int_{Q1}^{Q2} V dq = \int_{Q1}^{Q2} \frac{q}{C} dq = \frac{1}{2} C(V_2^2 - V_1^2) \qquad (5.2)$$

Where V_1 and V_2 are the voltage levels before and after the energy is released (V_{MAX} & V_{MIN} in Figure 5.8).

The minimum capacitance depends on the power drawn by the sensor P_S during the T_{ON} period, described in Figure 5.7 (b), where the capacitor voltage goes from V_1 to V_2 and is described by:

$$C \geq \frac{P_{SENSOR} T_{ON}}{0.5(V_2^2 - V_1^2)} \tag{5.3}$$

With P_{SENSOR} being the consumption of the load/sensor connected to the harvester.

For the specific application of a temperature sensor, the module was measured to draw 100μWatt for 1 second, causing a voltage drop from 1.8 to 1.2 V (minimum voltage levels for the sensor to operate) the minimum capacitance would be 120μF. To ensure enough storage capacitance two capacitors where chosen 1000μF and 470μF for comparison.

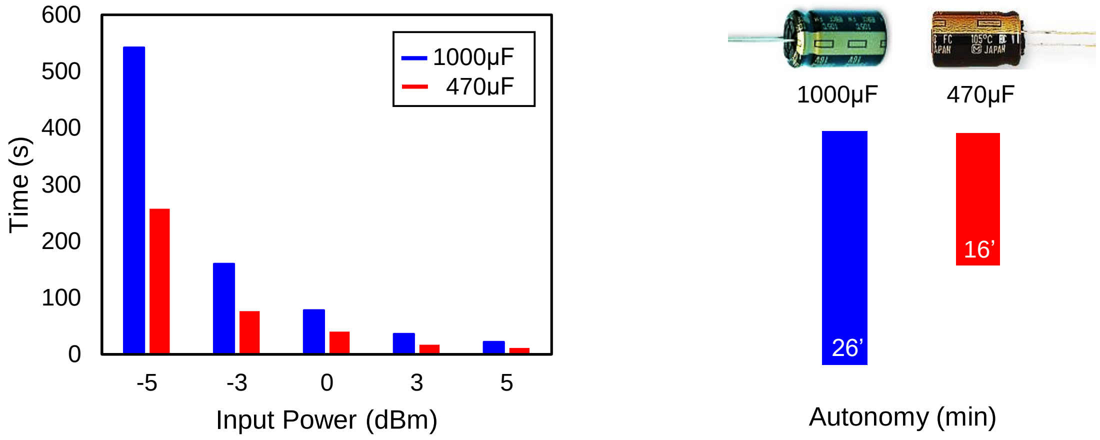

(a) (b)

Figure 5.9: (a) Time needed for the system to charge the capacitor from 0 to 1.8V (Cold start), (b) Measured autonomy of the system for the two selected capacitors.

Figure 5.9 shows the metrics used to choose the most appropriate capacitor. In the left (a) the time for the system to charge the capacitor from 0 to 1.8V is presented through multiple measurement for different power levels. The smaller capacitor is approximately 55% faster in charging through cold-start for all power levels. However its autonomy presented in the right (b) is less than the 1000μF by 10 minutes as expected. As explained in the previous section the sensors autonomy is not considered as much of a deciding factor for this scenario, that's why the smaller capacitor (470 μF) is selected since it provides enough autonomy for half the cold start time.

5.4 Total system Efficiency

The total system efficiency was measured at different points of the setup in order to identify the efficiency bottlenecks that occur during the RF power harvesting. Initially the testing setup will be presented in order to provide the complete framework of the measurement intrinsics.

The received power Pr by the antenna placed at a distance R from the transmitting antenna can be described by the Friis transmission equation [59]:

$$P_r = P_t G_t G_r \left(\frac{c}{4\pi f_0 R}\right)^2 \tag{5.4}$$

Where *c* is the speed of light in free-space and *f₀* is the frequency of the transmitted signal. The receiving power will be measured by a power meter. The simulation of this formula in Matlab for the existing setup and different antenna gains is presented in Figure 5.10. The graph below provides an approximation of the power levels that the system will be exposed to. The simulation results matched the measured ones with +/- 10% accuracy.

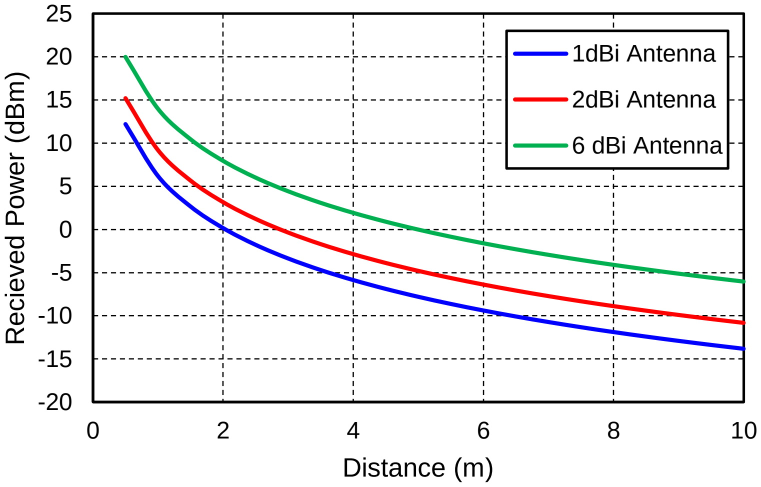

Figure 5.10: Simulated Power received versus distance for different antenna gains.

The Power Conversion Efficiency is calculated from:

$$PCE(\%) = \frac{P_{Load}}{P_{in}} = \frac{V_{Load} I_{Load}}{P_{in}} \tag{5.5}$$

5.4.1 Measurement Setup

The first step of setting up the test bench was to create a 3Watt EIRP transmitter. Effective Isotropic Radiated Power (EIRP) is the total power that will have to be radiated by an antenna that radiates uniformly power in all directions, to present the same radiation intensity as the physical source at a receiver pointed at the direction of the antenna's main lobe (strongest beam). EIRP is related to the power transmitted from the antenna (P_t), the cable losses (L_c) and the antenna gain (G_t) by:

$$\mathrm{EIRP} = P_t - L_c + G_t \tag{5.5}$$

In order to produce 3Watt EIRP with the provided 5dBi Horn antenna that could transmit at 868MHz the RF signal produced by the Agilent 8648C [60] must be amplified by a 3Watt RF amplifier. Then the output of the amplifier is connected through a 10dB attenuator (for protection) to the spectrum analyzer to measure 20dBm (+10dB from the attenuator) at 868MHz as shown in Figure 5.11. Therefore the output of the RF amplifier including the cable losses will be 30dB plus 5dB from the antenna will produce a 35dBm signal which is almost 3W EIRP, Figure 5.12.

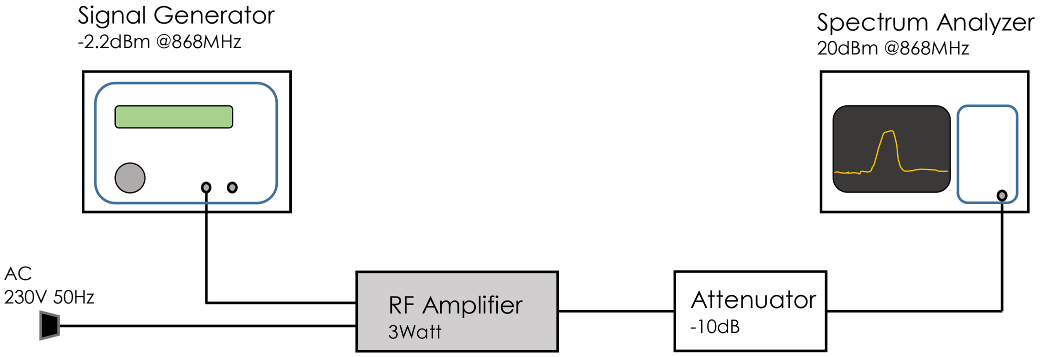

Figure 5.11: Test Setup for measurement of the 3W EIRP transmission.

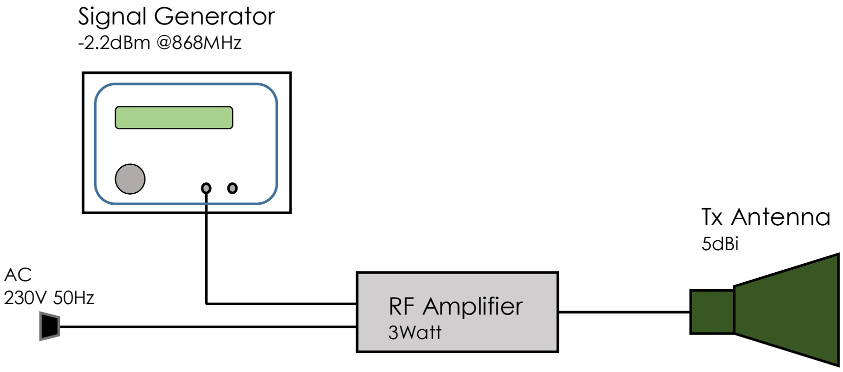

Figure 5.12: 3W EIRP transmission topology.

The measurement setup was installed inside an anechoic chamber to minimize electromagnetic wave reflections which would compromise the measurements. The transmitting antenna was pointed at a line of sight configuration with the receiving antennas as shown in the figures bellow.

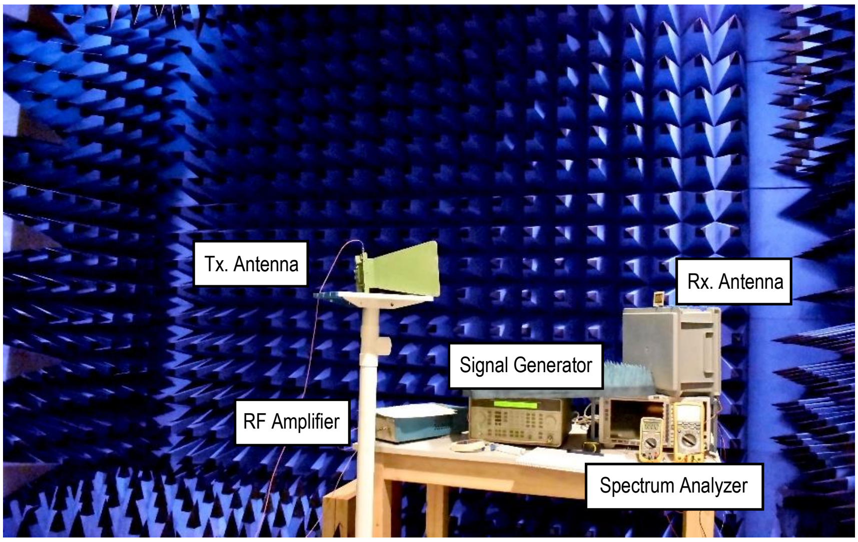

Figure 5.13: Test Setup inside the anechoic chamber.

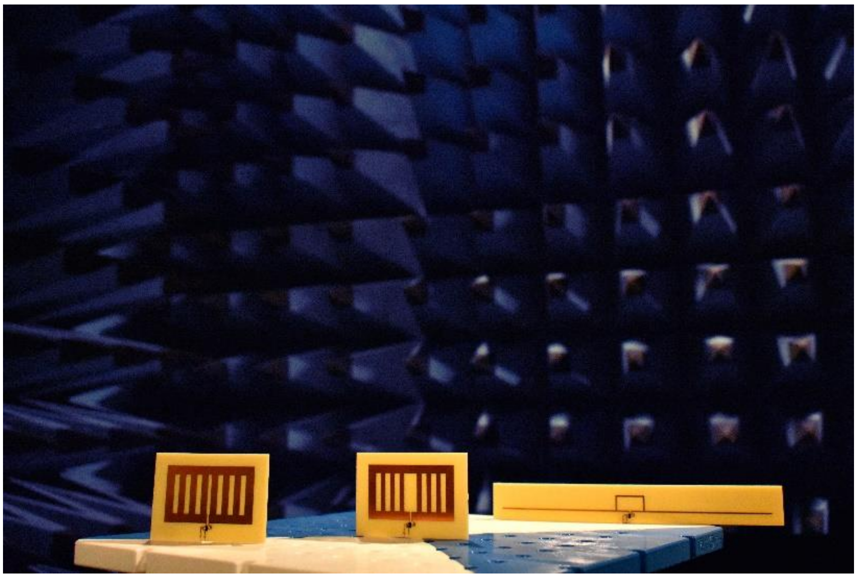

Figure 5.14: Fabricated PCB Antennas.

5.4.2 Complete System Measurements

The complete RF harvesting system from the receiver's side is illustrated in Figure 5.15. It contains the fundamental blocks that were analyzed in the previous chapters and the conversion efficiencies between them. The first one (η_1) is the RF-DC conversion of the antenna and the rectifier combined, the second one (η_2) is the DC-DC conversion efficiency of the boost converter embedded inside the BQ 25570 power management IC that boosts the voltage to the V_{STOR} value. Finally the third efficiency (η_3) is the DC-DC conversion efficiency of the buck converter that generates V_{OUT} to supply the sensor.

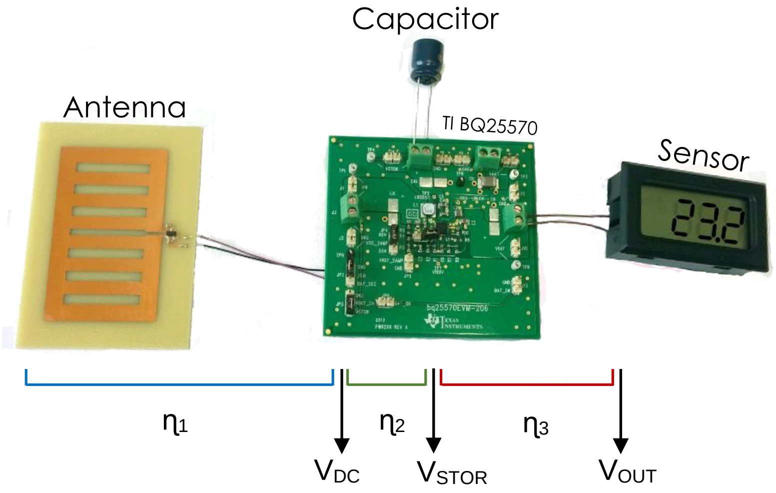

Figure 5.15: Complete RF harvesting prototype system. The different η's represent different power conversion efficiencies and the arrows point out the voltage outputs.

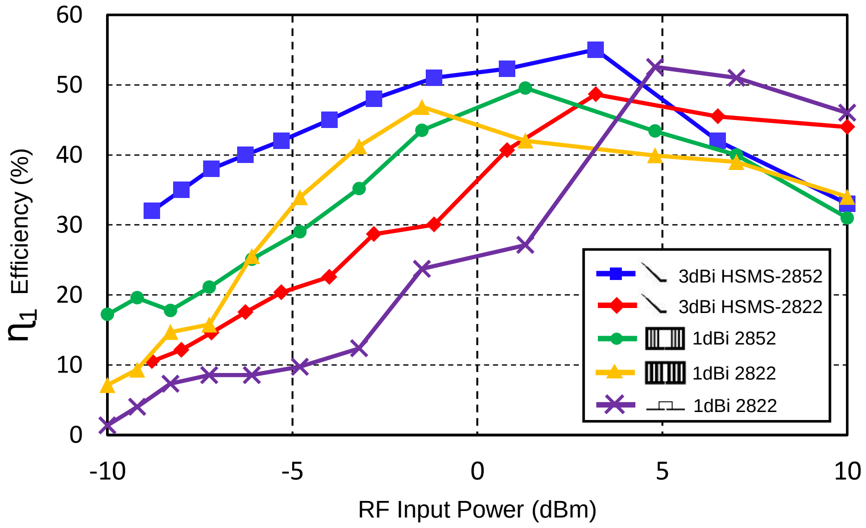

Figure 5.16: RF-DC efficiency of the examined antennas and rectifiers for different input power levels

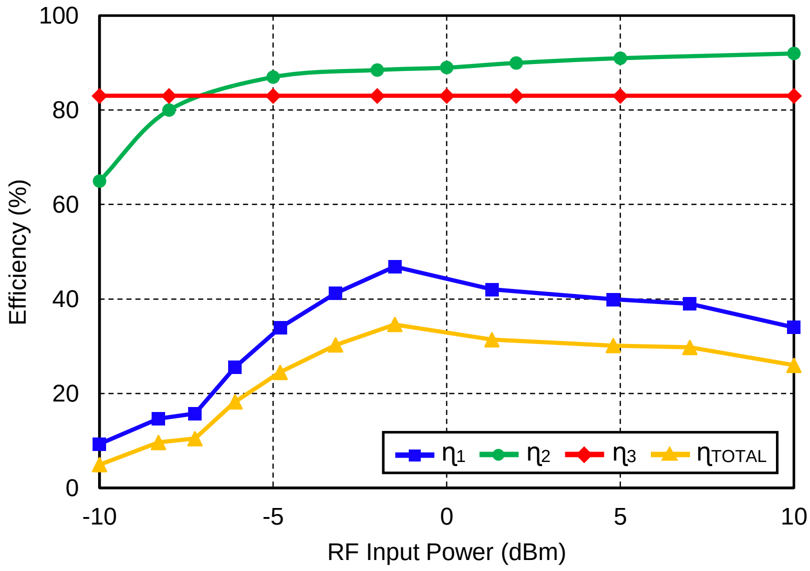

Figure 5.17: Efficiency measurements for different sections of the Harvesting system presented in Figure 5.15.

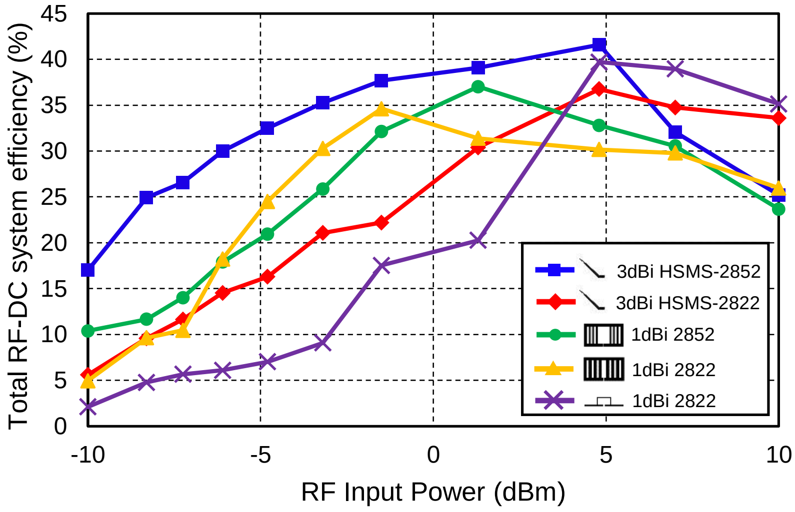

Figure 5.18: Total system RF-DC conversion Efficiency as a function of RF input power levels for all the antenna topologies developed in this thesis.

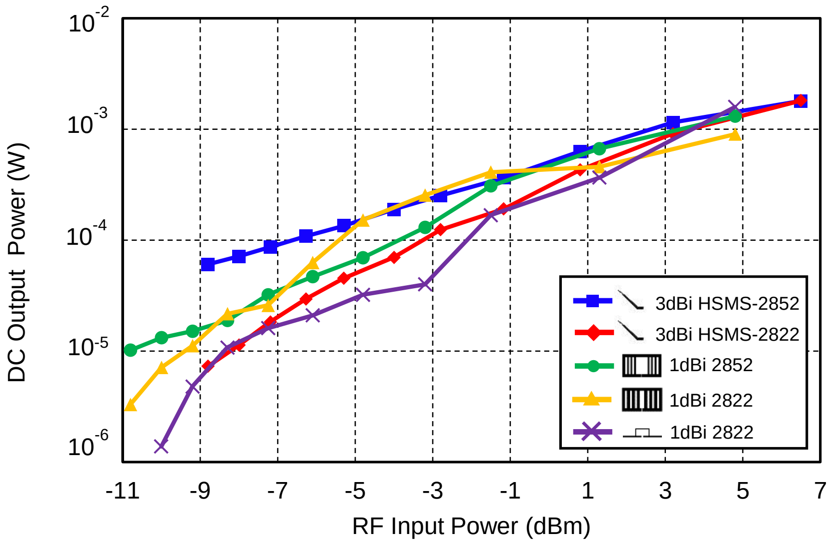

Figure 5.19: DC Power output as a function of RF input power levels for the examined antennas for a 5kOhm load.

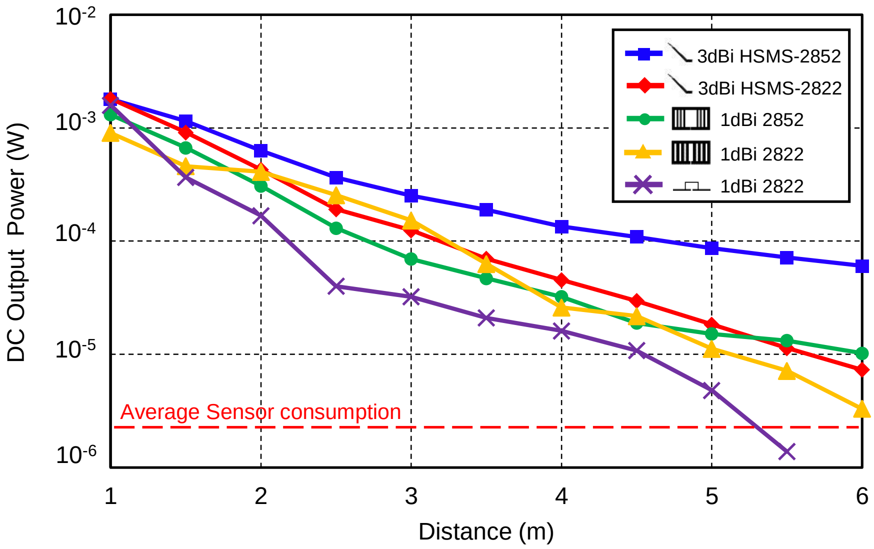

Figure 5.20: DC Power output versus distance for the examined antennas, the red dotted line represent the average consumption of the sensor.

Figure 5.16 shows the RF-DC conversion efficiency of the tested antennas with their embedded rectifiers. The PCB antennas present comparable performance, in terms of conversion efficiency, to the commercial 3dBi whip antennas. Especially the 1dBi PCB fabricated antenna with the HSMS-2822 rectifier outperformed the PCB HSMS-2852 antenna counterpart for the range of 0 to -5dBm. However the HSMS-2852 fabricated PCB antenna presents higher efficiency from all the compared antennas except its 3dBi commercial counterpart for the range of -5 to -10 dBm.

Furthermore, Figures 5.17 and 5.18 present system efficiency in different sections and the total system efficiency for different power levels respectively. The part that constitutes an efficiency bottleneck is the RF-DC conversion as it can be concluded from the graphs. The power management IC also introduces some losses especially at lower power levels. Table 5.1 summarizes the maximum total system efficiency for each topology.

Finally, Figure 5.20 depict the DC power output of the system versus the Input power and distance respectively while Figure 5.19 shows the DC power output of the rectifier without the power management IC. The average consumption of the sensor operating for one second every 30 seconds drawing 100 μWatt will be 3.4 μWatt. Thus all of the topologies presented in these figures will be able to power the sensor from at least five meters when the RF source is transmitting at 3W EIRP on average. As mentioned before, the average transmission power must be greater than the average sensor consumption power for autonomous operation. This leaves enough room for duty cycling techniques to be applied to the transmitter in order to lower the average transmitted power. If the sensor was operating continuously at 100 μWatt only the commercial 3dBi HSMS-2852 antenna would be able to satisfy its energy needs from approximately 4.5 meters while the rest of the topologies would not be able to after 2 to 3 meters of distance.

Antenna Topology	Maximum Total Efficiency	RF Input Power Levels (dBm)
3dBi HSMS-2852	41.5%	4.8
3dBi HSMS-2822	36.7%	5
1dBi HSMS-2852	37%	1.3
1dBi HSMS-2822	34.6%	-1.8
1dBi HSMS-2822 (Modified dipole)	38.9%	7

Table 5.1: Comparison of maximum total RF-DC conversion efficiencies for the proposed antenna topologies

5.5 Loss Classification

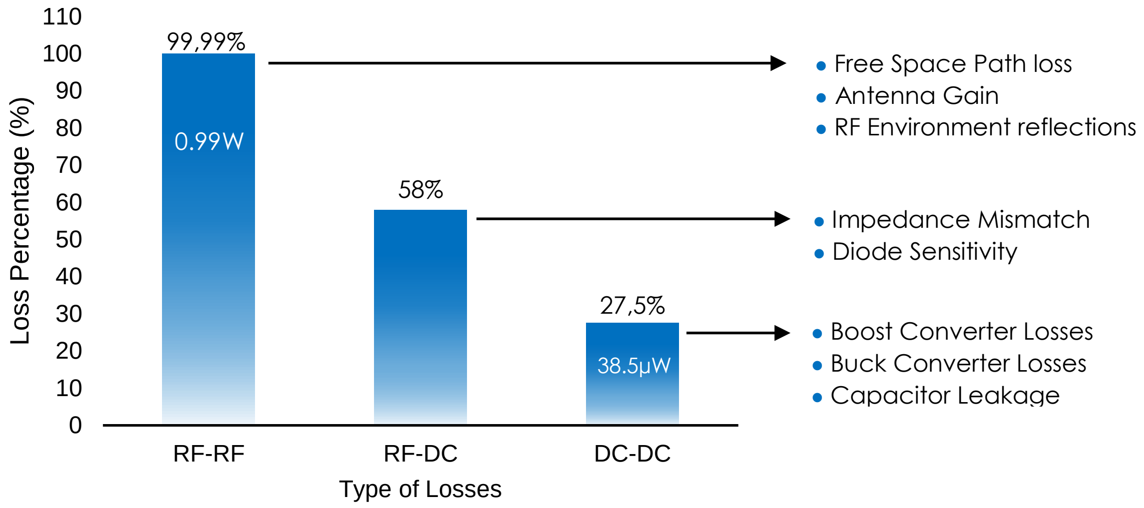

Figure 5.21: Loss categorization for the 3dBi HSMS-2852 rectenna @ 3W EIRP transmission, distance of 4 meters.

The main types of losses are presented in Figure 5.21. According to this graph the highest percentage of losses exist in the RF-RF environment. This translates to the efficiency of transferring low amounts of energy in the RF field also known as free space path loss (FSPL). The FSPL can be summarized as the loss between two isotropic radiators in free space, expressed as a power ratio in dB [61]. Therefore 1watt (30dBm) transmitted at 868MHz from a 5dBi to a 3dBi antenna in a line of sight setup with a transmission distance of 4 meters will be subjected to a 35db loss of signal strength at the receiver (Formula 5.6). That equals to -5 dBm (320 μW) of received power, meaning that 0.99968 watt almost 99.99% of the total transmitted power, was lost in the air.

$$\mathrm{FSPL} = 20\log_{10}(d) + 20\log_{10}(f) + 20\log_{10}\left(\frac{4\pi}{c}\right) - G_t - G_r \tag{5.6}$$

Apart from the free space path loss environmental reflections can also boost or reduce the receiving signal depending on the room's topology. In the examined case, reflections are minimized because the measurements were conducted in an anechoic chamber.

The RF-DC conversion efficiency of the rectenna depends on the RF power input intensity and the exact impedance match. When the power is small or the load is not matched, the efficiency drops dramatically.

The RF-DC loss is also determined by the characteristic of the diodes, which have their own junction and breakdown voltage, if the input voltage to the diodes is lower than the junction voltage or higher than the breakdown voltage the diode presents a poor rectifying characteristic. As a result, the RF-DC conversion efficiency drops with an input higher or lower than the optimum. It is worth noticing that all the measured maximum conversion efficiencies were reported at high RF power incident level because of the reason mentioned above. These losses amount to 58% at input power of -5dBm, even for a high sensitivity RF diode like the HSMS-2850.

Finally the power management IC introduces its own losses as well. The nano-powered boost and buck converters are highly efficient at input power levels of 0 dBm or higher with an average efficiency of approximately 90% as shown in Figure 5.17. However in this case (of -5dBm input power), 27.5% of the input DC power will be dissipated as switching and conduction losses of the converter's FETs as well as capacitor leakage and other parasitic losses that in total amount to 38.5 μW.

5.6 Conclusions

In this Chapter, the total dedicated RF harvesting system was presented and the performance of different antenna configurations was compared. The proposed prototype system, apart from the antenna designs, includes a rectifying circuit, a power management circuit, a storage capacitor and a temperature sensor. The efficiency at different points of the system was measured and showed that the major performance bottleneck is the conversion efficiency of the antenna-rectifier combination. Most peak efficiencies where observed between the 0 to 5 dBm of input power, with the PCB antennas performing close to the level of the commercial ones. Specifically, the peak system efficiency of the fabricated PCB antenna was 37% at 1.3 dBm while the commercial 3dBi antenna system reached 41.5% at 4.8 dBm.

The sensors average DC power consumption (3.4 μW) can be supplied at a distance of 6 meters for most of the antenna configurations when the transmitter uses a 100% duty cycle. Alternatively the sensor can be powered continuously from a distance of 3 to 4 meters depending on the antenna topology.

Chapter 6

Conclusions and Recommendations

This chapter summarizes the findings and contributions of this thesis.

6.1 Conclusions

The research journey of this thesis was initiated by the pursuit to develop an innovative wireless power transfer system that could be embedded inside the medical infrastructure to provide better healthcare services. The study has drawn insights from literature and empirical data having aiming to answer the main research question:

How to design a system that will enable wireless power transfer for low power devices such as small sensors, actuators and IoT modules as efficient and cost effective as possible?

The autonomous operation of these kind of sensors will integrate the medical IoT domain faster into the existing infrastructure. This feature, however, heavily relies on the wireless powering of these sensors which poses as a significant challenge since the power levels that can be transmitted are limited. Therefore it is of the utmost importance to accurately design the antenna – rectifier combination to maximize the harvested power. Based on existing literature studies of antenna designs, it has been found that conjugate matched antennas and rectifiers increase the system miniaturization.

Simulations through analytical models were implemented in order to identify the non-linear behavior of the Schottky diode in terms of output voltage, operating frequency and input impedance. It has been found that the most efficient and cost effective rectifying topology is the single stage voltage multiplier circuit for the power levels that the system is going to operate. The fundamental components of this circuit are the Schottky diodes. The Schottky diode's saturation current has shown to generate higher output voltage, that is why the HSMS-285x diode was selected for the low power scenario and the HSMS-282x diode was selected for the high power scenario.

Finally the proposed antennas that conjugately match the input impedance of the rectifier as well as the commercially available designs were fabricated and tested. The results of the experiments in the anechoic chamber that minimized heterogeneous interference to the measurements, showed that the proposed system can operate as efficiently as its commercial counterpart for specific distances.

6.2 Answers to Research Questions

- *Which is the most suitable rectifying topology for the proposed application?*

  The goal of this thesis is to power the wireless sensor from 3 to 5 meters. The circuit that showed the highest efficiency for the RF power levels (-10 to -5 dBm) present at that range is the single stage voltage multiplier. More rectifying stages offer benefits at higher power levels where a higher voltage output is needed. However the proposed scenario has not benefited by output voltages higher than 3V, a value that the single stage voltage multiplier can effectively produce (Chapter 2).

- *How does input power and frequency influence the Impedance of the rectifier?*

  The rectifier is based on the Schottky diode optimized for RF signal detection. This diode present a non-linear behavior as the frequency and the input power increases. The results from Matlab simulations and lab measurements showed that an increase in frequency decreases the real part of the rectifier's impedance while the imaginary part initially becomes more capacitive and after the 1GHz mark begins to decrease. In similar fashion, an increase in input power results in exponential increase to the real part of the rectifier's impedance at the -5dBm mark while the imaginary part at the same mark becomes less capacitive (Chapter 2).

- *Can Conjugate Matching antennas power the proposed system and how do they perform when compared to traditional commercial counterparts?*

  The fabricated PCB antennas, which match the impedance of the rectifier without the need for matching network, after lab measurements showed that they can supply the temperature sensor from 0 to 5 meters when the sensor operates at the proposed duty cycle. For continuous operation they can supply the load for a maximum distance of 3.3 meters. This performance is on par with the commercial counterparts that feature a higher antenna gain. Concluding, the PCB antenna topologies presented total RF-DC efficiencies that surpass the "high power" commercial counterpart while being competitive with the "low power" one at the power levels ranging from -5 to 0 dBm (Chapters 3 and 4).

- *What improvements does the power management IC provide?*

  The power management IC offers programmable maximum power point tracking that contributed to a slight average increase of the power levels harvested. Furthermore it provides isolation of the harvesting infrastructure to the sensor and the storage element. It also contains a boost converter that can be programmed to supply batteries offering over and under voltage protection. A buck converter is also included to regulate a constant voltage output to the load. However after measurements it was discovered that the boost converter is not very efficient at low power levels especially when the DC current is not sufficient. Overall the options that this IC offers are necessary for a robust commercial product with the expense of some micro watts of power (Chapter 5).

- *What is the overall RF-DC conversion efficiency of such a system? Identify the losses.*

  The overall conversion efficiency of the proposed PCB antenna system presented a maximum of 37% at 1.3 dBm which is an improvement over several commercially available systems. The majority of the losses are due to the free space path loss phenomenon which constitute the major limitation for RF power transfer at low power levels. Also impedance mismatches and the Schottky diode's sensitivity can also play a significant role on the system efficiency. Finally the power management IC introduces a small amount of losses that is insignificant when compared to the previously mentioned factors (Chapter 5).

6.3 Future Work and Recommendations

During the development of this research project a number of possible avenues for further investigation have been identified and the most important of them are the following:

- The proposed system provides a single antenna for energy harvesting purposes, this antenna configuration could be modified to be able to receive and transmit data communications with the router. This will result to a more compact and complete system since the transmitter and the receiver could communicate apart from the application data, information about the charging state.

- Furthermore, the system could offer multi-type harvesting infrastructure for higher autonomy. Specifically small solar cells and piezoelectric devices can be combined with the existing antenna harvesting system that will ensure several ways of power generation and extra redundancy.

- Transmitter design optimizations. This thesis did not explore the transmitting side of the system in depth because the focus was on optimizing the receiving side. However communication between the transmitting antenna and the receiver can aid in developing transmitting antennas and schemes that utilize beam-forming, much like the Wi-Fi transmitters, to boost the signal by directing it to a specific location minimizing the losses.

Bibliography

[1] C. Perera, A. Zaslavsky, P. Christen and D. Georgakopoulos, “Sensing as a service model for smart cities supported by Internet of Things”.

[2] Internet of Things (IoT) Healthcare Market by Component (Implantable Sensor Devices, Wearable Sensor Devices, System and Software), Application (Patient Monitoring, Clinical Operation and Workflow Optimization, Clinical Imaging, Fitness and Wellness Measurement) - Global Opportunity Analysis and Industry Forecast, 2014 – 2021

[3] N. Mahmood; A. Shah; A. Waqas; Z. Bhatti; A. Abubakar; H. Abid M. Malik, “RFID based smart hospital management system: A conceptual framework”, The 5th International Conference on Information and Communication Technology (ICT4M), 2014, Pages: 1 – 6.

[4] Handbook Of Industrial Automation, Richard Shell, 2000

[5] H. J. Visser and R. J. M. Vullers, “RF energy harvesting and transport for wireless sensor network applications: principles and requirements,” Proceedings of the IEEE, vol. 101, no. 6, pp. 1410-1423, June 2013.

[6] H.Liu, “Maximizing efficiency of wireless power transfer with resonant Inductive Coupling,” 2011.

[7] A. Kurs, A. Karalis, R. Moffatt, J. D. Joannopoulos, P. Fisher, and M. Soljacic, “Wireless power transfer via strongly coupled magnetic resonances,” Science , vol. 317, no. 5834, pp. 83-86, June 2007

[8] J. O. Mur-Miranda, W. Franklin, G. Fanti, Y. Feng, K. Omanakuttan, R. Ongie, A. Setjoadi, and N. Sharpe, “Wireless power transfer using weakly coupled magneto static resonators,” in Proc. of IEEE Energy Conversion Congress and Exposition (ECCE), Atlanta, GA, Sept. 2010.

[9] Coleman, Christopher, “An Introduction to Radio Frequency Engineering”. Cambridge University Press. pp. 1–3. ISBN 1139452304.

[10] W. Y.Toh, Y. K.Tan, W. S.Koh et al., “Autonomous Wearable Sensor Nodes With Flexible Energy Harvesting”, IEEE Sensors Journal, vol. 14,no. 7, pp. 2299–2306, July 2014.

[11] T.Torfs, V.Leonov, C.Van Hoof et al., “Body-Heat Powered Autonomous Pulse Oximeter,” in 5th IEEE Conf. on Sensors, Oct. 2006, pp. 427–430.

[12] M.L.Ku, W.Li, Y.Chen et al., “Advances in Energy Harvesting Communications: Past, Present, and Future Challenges,” IEEE Comm. Surveys Tutorials, vol. PP, no. 99, pp. 1–1, 2015.

[13] S. Lee, R. Zhang, and K. Huang, “Opportunistic wireless energy harvesting in cognitive radio networks,” IEEE Transactions on Wireless Communications, vol. 12, no. 9, pp. 4788-4799, September 2013.

[14] I. Flint, X. Lu, N. Privault, D. Niyato, and P. Wang, “Performance analysis of ambient RF energy harvesting: A stochastic geometry approach,” in Proc. of IEEE Global Communications Conference (GLOBECOM), Austin, TX, USA, December 2014.

[15] Powercast transmitter datasheet available online at “http://www.powercastco.com /products/powercaster-transmitter”

[16] FCC Codes of Regulation, Part 15. Available online “http://www.access.gpo.gov/nara/cfr/waisidx03/”

[17] M. Erol-Kantarci and H.T. Mouftah, “Mission-aware placement of RF-based power transmitters in wireless sensor networks,” in Proc. of IEEE Symposium on Computers and Communications (ISCC), pp. 12-17, Cappadocia, July 2012.

[18] S. M. Riazul Islam, Daehan Kwak, MD. Humaun Kabir, Mahmud Hossain and Kyung-Sup Kwak, “The Internet of Things for Health Care: A Comprehensive Survey” IEEE Access, vol. 3, pp 678-708, June 2015.

[19] ERC Recommendation 70-30, Electronic communications committee ECC, May 2017, pp 35. Online : http://www.erodocdb.dk/docs/doc98/official/pdf/rec7003e.pdf

[20] H. J. Visser, S. Keyrouz and A.B. Smolders, “Optimized rectenna design”, WiPE, pp 44-50, March 2015.

[21] K. Ng Kwok, “Schottky-Barrier Diode”, November 2010, John Wiley & Sons.

[22] Schottky barrier theory available online at “https://en.wikipedia.org/wiki/Schottky_barrier”

[23] D.A Fleri and L.D Cohen, “Nonlinear analysis of the Schottky-barrier mixer diode”, IEEE Transactions on Microwave Theory and Techniques, Vol. 21 No. 1 pp. 39-43, January 1973.

[24] S.El-Rabaie, V.F. Fusco and C. Stewart, “Harmonic balance evaluation of nonlinear microwave circuits – a tutorial approach”, IEEE transactions on education, Vol. 31, No. 3, August 1988.

[25] HSMS-282x SMD Schottky diodes data sheet. Online at “www.avagotech.com”.

[26] HSMS-285x SMD Schottky diodes data sheet. Online at “www.broadcom.com”.

[27] HSMS-286x SMD Schottky diodes data sheet. Online at “www.broadcom.com”.

[28] R. G. Harrison, X. Le Polozec, “Non-square law behavior of diode detectors analyzed by the ritz-galerkin method," IEEE Transactions on Microwave Theory and Techniques, vol. 42, no. 5,pp. 840-846, 1994.

[29] J .Akkermans, M. van Beurden, G. Doodeman ,H. Visser, “Analytical models for low-power rectenna design”, IEEE Antennas Wireless Propagation Lett 4:187–190, 2005.

[30] B. Merabet, L. Cirio L, H. Takhedmit, F Costa, C. Vollaire , B Allard, O Picon "Low-cost converter for harvesting of microwave electromagnetic energy", IEEE Energy conversion congress and exposition, San Jose, pp 2592–2599, 2009.

[31] S. Jongshi, C. In-Young, P. Young-June, H. Min "A new charge pump without degradation in threshold voltage due to body effect", IEEE Solid-State Circuits Vol 35:1227–1230, 2000.

[32] S. Heljo, M. Li, E. Lilja, S Majumdar, and D. Lupo, "Printed half-wave Rectifier circuits based on organic diodes" IEEE Transactions on el. devices, Vol.60, No.2, February 2013.

[33] P.Nintanavongsa, U. munchuk, D.R. Lewis and K. Chowdhury, "Design optimization and implementation for RF energy harvesting circuits", IEEE journal in circuits and systems, Vol.2, No.1, March 2012.

[34] T. Tanzawa, T. Tanaka, "A dynamic analysis of the Dickson charge pump circuit", IEEE Journal of Solid-State circuits, Vol.32, pp.1231-1240, 1997.

[35] D. F. Spencer, R. Aryaeinejad, El. Reber, "Using the Cockroft-Walton voltage multiplier design in handheld devices", IEEE Nuclear Science Symposium Conference Record, Vol.2, pp. 746-749, 2001

[36] J. Curty, N. Joehl, C. Dehollain, and M. Declercq, "Remotely powered addressable UHF RFID integrated system". IEEE Solid-State Circuits, vol.40, no.11, November, 2005.

[37] J. Visser, "Indoor wireless RF Energy Transfer for powering wireless sensors", Radio-engineering, Vol.21, No.4, December 2012

[38] Reflection coefficient theory available at "https://en.wikipedia.org/wiki/Reflection_coefficient"

[39] J. Rahola, "Power waves and conjugate matching", IEEE Transactions on Circuits and Systems II: Express Briefs, vol. 55, no. 1, pp. 92-96, 2008.

[40] Impedance matching theory available online at "https://en.wikipedia.org/wiki/Impedance_matching"

[41] A. Kumar, S. inha and A. Sepahvand, "Improved Design Optimization for High-Efficiency Matching Networks", IEEE Transactions on Power Electronics, Vol. PP, Issue: 99, February 2017.

[42] Y. Han and D.J. Perreault, "Analysis and Design of High Efficiency Matching Networks," IEEE Transactions on Power Electronics, vol. 21, no. 5, pp. 1484-1491, September 2006.

[43] A. Echearte, D. Jimenez-Lopez, M. Gasulla, F. Giuppi and A. Georgiadis, "A High-efficiency Matching Technique for Low Power Levels in RF Harvesting", PIERS Proceedings, August 2013.

[44] D. M. Pozar "Microwave engineering (4th Edition)", Wiley, 2011.

[45] P.H. Smith, "Electronic Applications of the Smith Chart (Electromagnetics and Radar)", SciTech Publishing Inc., July 1995.

[46] Basu, Dipak ," Dictionary of Pure and Applied Physics", 2nd Ed. CRC Press. p. 21, 2010.

[47] R.S. Elliot, “Antenna Theory and Design, revised edition, John Wiley & Sons, New York, 2003.

[48] L. Burgess, “Matching RFIC Wireless Transmitters to small loop Antennas”, High Frequency Electronics, pp.20-28, March 2005.

[49] C.A. Balanis, “Antenna Theory: Analysis and Design, 2nd ed.”, John Wiley & Sons 1997.

[50] Texas Instrument BQ25570 Ultra Low Power Harvester Power Management IC with Boost Charger, and Nano-power Buck Converter. Online “http://www.ti.com/product/BQ25570”

[51] L. Alexander, “Off the grid”, Dwellings, 2007.

[52] Depth of discharge vs Cycle Life for Li-ion batteries available at ”http://www.mpoweruk.com /life.htm”.

[53] G.Q. Max Lu, “Supercapacitors Materials, Systems, Applications”.

[54] Double layer capacitors information available online at “http://www.electronicdesign.com/power/can-supercapacitors-surpass-batteries-energy-storage”.

[55] P. Mcknight Deeley, “Electrolytic capacitors: the theory, construction, characteristics and application of all types”, The Cornell-Dubilier Electric Corp., 1938.

[56] S.F.J Flipsen, “Power Sources Compared: The ultimate truth”, Journal of power Sources, 2002.

[57] D. Linden T.B. Reddy, “Handbook of Batteries”, McGrew-Hill, 2001.

[58] Regulatory status for using RFID in the EPC Gen2 (860 to 960 MHz) band of the UHF spectrum, available online at “https://www.gs1.org/docs/epc/uhf_regulations.pdf”.

[59] H.T.Friis, Proc. IRE, vol. 34, p.254. 1946

[60] Agilent 8648C Signal Generator, Specifications available online at “http://literature.cdn.keysight.com /litweb/pdf/5965-432E.pdf?id=1000031128:epsg:dow”

[61] "Standard Definitions of Terms for Antennas", IEEE Std. 145-1983